Spring 5-5-2022

Approaching Quantum-limited Electrometry in the Single-photon Regime

Sisira Kanhirathingal
Sisira.Kanhirathingal.GR@Dartmouth.edu

Recommended Citation

Kanhirathingal, Sisira, "Approaching Quantum-limited Electrometry in the Single-photon Regime" (2022). *Dartmouth College Ph.D Dissertations*. 91.
https://digitalcommons.dartmouth.edu/dissertations/91

APPROACHING QUANTUM-LIMITED ELECTROMETRY IN THE SINGLE-PHOTON REGIME

A Thesis
Submitted to the Faculty
in partial fulfillment of the requirements for the
degree of

Doctor of Philosophy

in

Physics and Astronomy

by Sisira Kanhirathingal

Guarini School of Graduate and Advanced Studies
Dartmouth College
Hanover, New Hampshire

May 2022

Examining Committee:

Alexander J. Rimberg, Chair

Miles P. Blencowe

Chandrasekhar Ramanathan

Andrew D. Armour

F. Jon Kull, Ph.D.
Dean of the Guarini School of Graduate and Advanced Studies

Abstract

Mesoscopic quantum systems currently serve as essential building blocks in many quantum information and metrology devices. This thesis investigates the potential of quantum-limited detection in a mesoscopic electrometer named the cavity-embedded Cooper pair transistor (cCPT). As one application, this charge detector can act as the basis for an optomechanical system in the single-photon strong coupling regime. The realization of this scheme would entail near quantum-limited, ultra-sensitive electrometry at the single-photon level, the feasibility of which is studied at length in this thesis.

On the one hand, we approach this question using a fundamental, first-principles study, where an operator scattering model is used to analyze the quantum dynamics of this device. While the cCPT is inherently a tunable, strongly nonlinear system affording diverse functionalities, we restrict our analysis to a necessary first investigation of its linear charge sensing capabilities, limiting to low pump powers corresponding to an average cavity photon number $\lesssim 1$. Assuming realizable cCPT parameters, we predict the fundamental, photon shot noise-limited charge sensitivity to be $0.12\,\mu\mathrm{e}/\sqrt{\mathrm{Hz}}$ when the pumped cavity has an average of one photon.

In practice, this lower bound is difficult to achieve using conventional detection approaches, owing mainly to the low-frequency noise caused by the coupling of two-level systems to the cCPT. Hence we further employ a top-down approach where the gate-dependent tunability of the cCPT is used to implement a feedback scheme derived from the Pound-Drever-Hall locking technique. This scheme effectively reduces the fluctuations due to intrinsic charge noise. In particular, we report a reduction in the resonant frequency fluctuations caused by the internal charge noise over a bandwidth of ∼1.4 kHz when the cavity is driven at an average photon number $n = 10$, and a bandwidth of 11 Hz for average $n = 1$. Our technique can be generalized to achieve frequency stabilization in tunable microwave resonators that play a vital role in today's quantum computing architectures, thereby moderating the limitations in detection caused by the intrinsic $1/f$-noise on such circuit devices. As a concluding study, we incorporate these feedback techniques to improve the charge sensitivity of the cCPT, thus demonstrating the potential of near quantum-limited charge detection using this device.

To my baby niece,
to whom I hope this work speaks more than physics

Acknowledgments

I am grateful for the constant encouragement and support I received from people near and dear to me during these past seven years. They have been with me throughout this endeavor, amidst the harsh winters and pleasant summers of Hanover, a raging pandemic, and the many ups and downs of my research experience. I am deeply grateful to have earned their trust to bring this work to completion.

First and foremost, I would like to thank my thesis advisor Alex for his extraordinary guidance throughout my doctoral life. I am grateful for his confidence in me, especially in the early years of my Ph.D. when I was unsure about the course of this thesis and my research capabilities. His grasp of the theory that underlies the intriguing experiments we conduct, the ease at which he diagnoses the 'noise' found in all shapes and forms in our lab, his math agility while crunching the numbers of the experimental parameters, and his ability to point towards the right source of literature are a few in a long list that I have strived to master in the past couple of years. Alex has always encouraged independent research while being the guiding force whenever I reached out. Most importantly, he always knew when to give me a time out – an often lesser recognized quality of a great thesis advisor.

The one aspiration I had when I joined Dartmouth for my Ph.D. was to create a research work that I can call self-standing in terms of its theoretical and experimental framework. I would not have fulfilled this intent without the exemplary guidance from Miles, my thesis co-advisor and the principal investigator in theory. I look up to Miles not only for his passion for physics and research methodology but also as a compassionate and uplifting person in general. I consider him my paternal figure in academics and a dear friend outside; I value the time he spent during our hikes answering my never-ending questions as much as I value our long research discussions. Hours would pass by during these discussions without noticing, and I enjoyed them very much, whether it happened in his art-filled office in the observatory during winters or around Dartmouth's beautiful campus during summers. Thank you for reaching out and pulling me out every time I got into the rabbit hole of higher-order calculations, and thank you for being incredibly patient while I figured out the right ways of scientific writing. The complementing research mentoring I received from Alex and Miles is a core part of my professional identity that has given me perspective and is an experience I will hold on to throughout my research career.

Next to the mentoring by one's advisor, perhaps the relationships that influence and determine the course of a Ph.D. most are the ones with the teammates. I have been fortunate on that front. Every day has been a learning experience with my team, through thick and thin. I have long since stopped counting the times I have reached out to Bhar in the lab. It has been a pleasure working with him, and it goes without saying that Bhar has kept the lab running for years in a row; he is a brilliant and hard-working researcher, and his technical and hands-on knowledge knows no bounds. I thank Jules for providing us with the miraculous, long-standing sample that is the cCPT and for imparting his valuable working knowledge about the small fridge and the dos and dont's of a Ph.D. I have always appreciated how Ben got things done with his attention to detail and understanding of the big picture. Finally, Billy was my big brother in the lab; we didn't get enough opportunities to work together, but I am grateful for the times we spent together since then. I greatly admire how effortlessly he continued taking more courses even in his senior years and how efficiently and quickly he mastered the ways of theoretical research.

From learning how to conduct fast-paced, productive research in an expert team comprising physicists, engineers, and computer scientists to being funded for the later phase of my thesis, my internship experience at Google's Quantum Computing Hardware lab has been a truly rewarding opportunity. I believe this internship helped me set the final plot line for my thesis. I am thankful for the fun and productive times I had with Marissa Giustina, Evan Jeffrey, and Daniel Sank. Most importantly, this opportunity allowed me to work with Josh Mutus, a mentor throughout the internship and my subsequent years at Dartmouth. I am indebted to him for helping me bring this work to fruition. Besides always encouraging me to reach out to experts and clear out a roadblock instead of spending days self-diagnosing it, his ability to explain physics jargon in layman's terms is one skill I have yet to master.

I greatly appreciate every productive interaction I had with the faculties during my time at Dartmouth. Each and every one of them brought forth their unique research and teaching styles, and I have learned a great deal from them. I want to thank Sekhar, a member of my thesis committee, for giving me his valuable time and advice

whenever I reached out, even during the busiest times. Andrew Armour has been exceedingly kind and generous to me by agreeing to be my external committee member on short notice and providing valuable feedback on my latest publication. Thanks to Kristina Lynch, for whom I had the immense pleasure to work as a TA multiple times, I had numerous interesting discussions with her about physics problems in Class Mech and Electromagnetism. I also extend my gratitude to James Whitfield for all his career guidance and delightful corridor conversations.

This work was supported financially by the NSF under Grant No. DMR-1807785 and by a Google research award. I also thank the Department of Physics and Astronomy at Dartmouth for the honor of the Gordon F. Hull fellowship during my final year here.

The key to completing a doctorate in a competitive field and in a place that showers snow six months a year is to ensure a strong support system outside work who understands the toll it takes on your personal life. To Linta Joseph, Shruti Agarwal, Salini Karuvade, Maryam Negahbani, and Vasanta Kommineni, thank you for your companionship and support through these years and for constantly inspiring me to keep going in the toughest of times by delivering exceptional work, despite choosing a STEM field with a significant gender gap. Thank you, Dhananjay Beri, Prashant Anantharaman, and Kanav Setia, for making my life at Hanover extremely memorable, and thank you, Suman Bera, for being a friend I can count on always.

Last but not least, I would like to extend my deepest gratitude to my family. It is tough to stay apart by thousands of miles, further separated by all the cultural and societal barriers. Even so, they have been with me throughout this journey since the beginning, and I cannot thank them enough for their trust and faith in me.

Contents

List of Figures

List of Tables

Chapter 1

Introduction

One extremely intriguing yet intricate task in designing observable open quantum systems is implementing schemes that enable quantum optimal detection. As physicists in academia and leading industries continue delving deeper into the realm of quantum measurements, more attention is being drawn to the sensitivity of quantum-limited amplifiers and detectors that closely track the dynamics of the measured systems [1, 2, 3]. One may address this question using theoretical investigations of the fundamental quantum limits imposed by the quantum mechanical nature of the detector itself [4]. Such investigations are important in determining the standard quantum limits achievable during measurement. These limits are bounded by the interplay between the measurement imprecision of the detector and its backaction on the system [5, 6]. On the other hand, a practical viewpoint may call for a top-down approach where the experimental limitations of the device are dealt with by additional/alternative modes of noise control in the system [7].

The general trajectory of such schemes progressing towards optimal detection of quantum phenomena revolves around three main objectives. Firstly, the measurement of a quantum state is optimized when the detector adds the minimum possible noise allowed by quantum mechanics, as mentioned above [4]. Secondly, one key culprit that inhibits the detection at its quantum-limited scale is the environmental noise that couples to the measured system or the detector itself. Hence techniques facilitating noise decoupling are vital in preserving the quantum coherence [7, 8]. Finally, additional decoherence will occur due to the backaction of the detector on the system [9, 10, 11, 12], which is typically reduced by adopting a weak measurement regime, as discussed further below. In other words, we address two types of interactions across the quantum-classical regime to realize optimize detection; we need

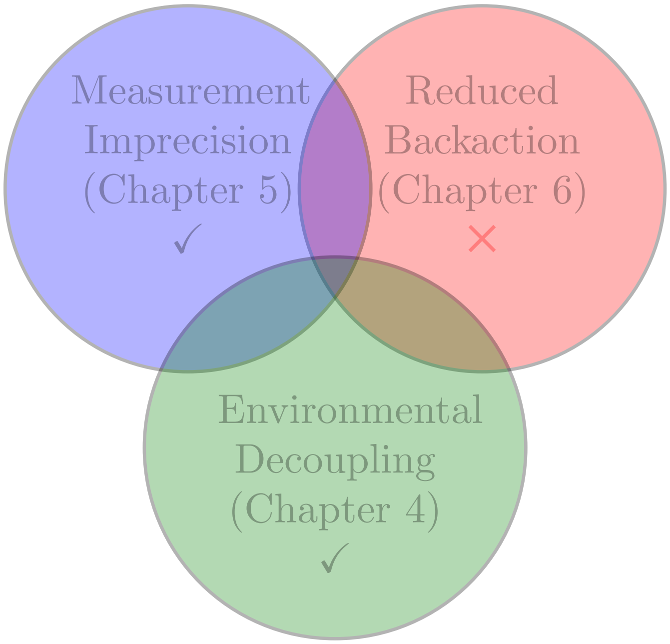

Figure 1.1: Topics covered in this thesis with focus on quantum-limited charge sensing using the cCPT. The current emphasis is on measurement imprecision and environmental decoupling. Backaction of the cCPT on a quantum system is to be investigated.

pathways that transfer information across the detector at this interface in a minimally disruptive (i.e., reduced backaction) but efficient manner, all the while isolating the system and the detector from the rest of the environment, be it classical or quantum mechanical.

Thesis Overview

The research work presented in this thesis involves investigations on a mesoscopic, superconducting system named the cavity-embedded Cooper pair transistor (cCPT). As we will establish through the discussions in subsequent chapters, in principle, the cCPT can operate at the intersection of the three objectives mentioned above (Fig 1.1). In the simplest sense, the characteristic features of the cCPT are modeled as a nonlinear microwave cavity. This design promotes diverse applications in electrometry, magnetometry, single-photon optomechanics, and parametric amplification etc [13, 14, 15]. This thesis primarily features theoretical investigations of the cCPT's linear charge sensing properties at the single-photon scale and experimental studies on environmental noise decoupling to enhance the electrometric capabilities of this device. The motivation behind these distinct yet related projects is presented further below.

From a pedagogical perspective, one overarching goal of this work is to present various measurement schemes tailored to realize near quantum-limited detection. We will accomplish this through the focused lens of the cCPT's diverse modes of operation. While a detailed study of all the potential applications of the cCPT is beyond the scope of the material presented here, we comment on the remaining aspects through brief discussions in the future work (Chapter 6) as well as by citing references reporting these studies.

Let us now look at the various detection regimes adopted by this thesis and are commonly practiced by the community to optimize detection. The bulk of this thesis will follow the 'weak and continuous measurement regime' where a steady-state signal collects data averaged over time such that the system being measured is minimally disturbed [16]. In terms of the Venn diagram presented in Fig. 1.1, such a measurement has dual advantages. Firstly, collecting data in small bits over a longer period of time enhances the signal-to-noise ratio and addresses 'the measurement imprecision' process. Secondly, this particular scheme ensures reduced backaction leading to extended coherence properties; this is opposed to an instantaneous, strong measurement that can affect the evolution drastically. While the present work does not take into account a measured quantum dynamical system and the effects of backaction, it instead considers a classical, simulated environment using a deterministic sinusoidal charge modulated signal (Refer Chapter 5). Typically, weak measurements are also adopted partly due to empirical limitations on the interaction strength between the detector and system. In order to gain sufficient information, these detectors are operated using high pump powers. However, as we will briefly touch upon in §6.1, the cCPT architecture can realize an optomechanical system driven to the 'ultra-sensitive, single photon-single phonon' strong coupling regime. Such an optomechanical system, if realized, can lead to displacement measurement of the mechanical resonator using a cavity that is driven merely at an average of a few photons.

Another critical distinction to consider is that the open system Hamiltonian modeled in the current work involves measuring both of the quadratures of a harmonic oscillator (i.e., a photonic cavity). This mode of measurement is termed 'phase-preserving detection' in the literature. Since the two observables form a conjugate pair (for example, the number and phase operators of the cavity) that do not commute, the detection (i.e., charge sensing in our context) is fundamentally limited by the Heisenberg's uncertainty principle. Consequently, this particular mode of charge sensing has a fundamental lower bound for the noise added during detection which further addresses the question of 'measurement imprecision' in Fig. 1.1. However, Chapter 6 briefly addresses another mode, phase-sensitive detection, that can also be realized in the cCPT using Hamiltonian engineering. The advantage of phase-sensitive detection schemes is their ability to detect a single quadrature with unlimited precision. However, the second quadrature that is not measured, in turn, is loaded with added noise to satisfy the uncertainty principle [4, 17].

Finally, the cCPT's charge detection is based on the coupling of the system with the microwave resonator component of the cCPT. As we will see in later chapters, this detection is dispersive, where the coupling appears as a phase shift in the reflected signal. This reduces the dissipation of useful information to the environment thus contributing to 'environmental decoupling' in Fig. 1.1. Dispersive measurements using microwave resonators have become a standard practice in detecting the state of a superconducting qubit. Our focus, however, is to investigate the cCPT's potential to detect the position of a mechanical oscillator. For completeness, we also note that one major difference in these two schemes is that the former is a quantum nondemolition (QND) measurement, where the Hamiltonian of the qubit system that is being measured commutes with the system observable (e.g., the spin). In the latter case, as the position observable does not commute with the Hamiltonian of the mechanical resonator, such a measurement is typically nonQND.

We now present a background into the two approaches adopted in this thesis to investigate quantum-limited charge detection by the cCPT. As clarified below, these two approaches form standalone projects and branches to provide relevant applications in their respective domains. However, our interests primarily lie in bridging these two approaches to boost the efficiency of the cCPT's performance, as presented in Chapter 5.

It is to be taken note that a good volume of this thesis contains verbatim taken from two relevant publications of the author [13, 18]. In order to provide a coherent picture, we have split different sections of these two papers into different chapters and have added further details. If a section is reproduced in this manner, we acknowledge this fact at the beginning using footnotes.

Quantum-limited Electrometry - Theory[1]

Rapid detection of electrical charge on the scale of an individual electron has long been an important experimental technique in such areas as readout of qubits [19, 20], detection of individual tunneling events [21], and motion sensing of nanomechanical resonators [22]. The most common means of performing such measurements consists of detecting changes in the current flowing through a mesoscopic charge detector, such as a single electron transistor or quantum point contact, due to changes in the detector conductance [23, 19, 22, 20, 24]. Numerous studies have investigated the limits on the charge sensitivity, which is determined by electronic shot noise in the detector current, and where the backaction on the measured system often exceeds the minimum required by quantum mechanics [25, 26, 27, 1].

An alternative and potentially superior mode of charge detection instead relies on detecting changes in the capacitive or inductive reactance of a superconducting device such as a Cooper pair box or Cooper pair transistor that is biased on its supercurrent branch [28, 29, 30, 31]. By embedding such a device in a resonant circuit and measuring changes in the phase of a reflected microwave probe signal, it is possible to dispersively detect single electronic charges with a sensitivity that is limited by photon shot noise in the probe signal and with backaction on the measured charge that may approach the minimum allowed by quantum mechanics [32].

The first phase of this thesis work presents theoretical investigations on the cCPT (presented in chapters 3 and 5, and published in [13]), which functions as the first amplifier stage of a dispersive electrometer due to its charge-dependent superconducting reactance. We show that this device is in principle capable of achieving charge sensitivities on the order of $0.1\,\mu\mathrm{e}/\sqrt{\mathrm{Hz}}$, better than the best predicted values for single Cooper pair transistors (SCPTs) [33] and other mesoscopic charge detectors. This is despite using many orders of magnitude less power (attowatts instead of picowatts) than is typical for previous electrometer devices, in particular corresponding to an average cavity photon number occupation $\lesssim 1$ for our cCPT device [14, 15], so that the cCPT is well suited for applications requiring minimal backaction.

We shall utilize a first principles, operator scattering approach for investigating the cCPT quantum dynamics that overcomes the limitations of the analyses presented in Refs. [34, 14], as discussed in detail in §3.2. The vital objective of such a study is to thoroughly understand this device in its linear charge sensing regime. In particular,

---

[1] We acknowledge that this section is reproduced from a Journal of Applied Physics publication by Kanhirathingal *et. al.* [13], with major contributions from Profs. Rimberg and Blencowe.

the present approach crucially provides the quantitative conditions under which the approximate eigenfunction expansion analysis of Ref. [34] and lumped element circuit analysis of Ref. [14] are valid. Furthermore, the scattering method provides a systematic way to derive the expressions for the various parameters of the effective cavity Hamiltonian. Relevant parameters include not only those for the effective linear cavity dynamics (e.g., renormalized resonant frequency), but also the explicit forms of the higher order nonlinear cavity terms and coupling terms between the cavity and other systems such as a nanomechanical resonator [34]. Most importantly, the scattering approach yields the versatile quantum Langevin equation for describing the effective cavity quantum dynamics, with explicit expressions for the damping and the associated quantum noise terms that are necessary for establishing the photon shot noise-limited charge sensitivity.

As a result of its single-photon-level charge sensitivity, the cCPT is capable of mediating the standard optomechanical interaction in the ultrastrong coupling regime [see Eq. (6.5) in §6.1]. The experimental realization of single photon optomechanical dynamics in this tripartite system (comprising the cavity, CPT, and mechanical resonator) will depend on the optimized non-linear charge sensitivity of the cCPT. As mentioned above, an analysis on such an optomechanical system is outside the framework of this thesis; instead, we use a deterministic sinusoidal charge modulated signal in the photon shot-noise limit as a necessary step towards such investigations.

Decoupling Environmental Noise[2]

The existence of two-level-system induced $1/f$-noise is well-known to limit the efficiency and sensitivity of devices across a breadth of applications – ranging from the semiconductor industry, to the emerging field of quantum computing processors [35]. Understanding its microscopic origin [36, 37, 38] and exploring different approaches to suppress this noise is a crucial step towards the realization of high coherence superconducting quantum circuits [39, 40, 41, 42], ultra-sensitive electrometry/magnetometry [15, 43, 44, 45, 46, 47, 48], and other studies more fundamental in nature [49, 50, 51].

Many approaches to reduce low-frequency noise focus on the elimination of two-level defects on the hosts, during fabrication and post-processing [52, 53, 54, 55, 35, 56]; or using error correction codes during the measurement itself. These branches of research are being intensely surveyed by the scientific community. Besides often

---

[2] We acknowledge that the bulk of this section is reproduced from a publication by Kanhirathingal *et. al.* [18], currently under peer review.

being a cumbersome task that can also sometimes be expensive to implement, some of these methods can cost anharmonicity of energy levels, which are critical for the performance of qubits [57]. Such systems can therefore profoundly benefit from the real-time detection and suppression of $1/f$-noise while performing measurements, thence significantly improving their performance [58, 59, 8], in such areas as qubit metrology and quantum sensing. For instance, this can result in a more effective, durable calibration of an operating physical qubit's parameters (e.g., T_1 and T_2 times). As a result, we may reduce the unaccounted bit-flip and phase-flip errors during a measurement, improving gate fidelity in a multi-qubit quantum processor.

The complete noise characterization of the cCPT presented in Ref. [14] addresses the role of the intrinsic noise in charge/flux bias leading to resonant frequency fluctuations, especially in regions where the cCPT can operate as a highly sensitive electrometer/magnetometer. By singling out bias regions where the cCPT is maximally sensitive to charge/flux fluctuations, measurements detected typical charge and flux noise spectral densities of the form $S_{\mathrm{qq}} \propto 1/f\ \mathrm{e}^2/\mathrm{Hz}$, and $S_{\Phi\Phi} \propto \sqrt{1/f}\ \Phi_0^2/\mathrm{Hz}$, respectively. The magnitude of these resonant frequency fluctuations at some bias points is of the order of the cavity linewidth, shifting the carrier signal away from the cavity resonance during the course of a measurement. As a result, while the ideal cCPT can operate as a quantum, photon shot noise-limited electrometer, the actual device in a realizable measurement setup is prone to charge fluctuations and other reducible noise sources, to date limiting its linear charge sensitivity to values two orders of magnitude worse [15] than the theoretically attainable minimum predicted in the first phase of our study.

Nevertheless, these charge fluctuations can be suppressed using feedback techniques that filter out the low frequency noise tampering with resonance, bringing the linear charge sensitivity of the cCPT closer to the photon shot noise-limit (not including the noise of the subsequent amplifier chain). Thus the second phase of the study (Chapter 4 and [18]) reports a reduction of these frequency fluctuations induced by the intrinsic charge/flux noise on the cCPT.

Such a study is of two-fold importance to the general circuit-QED audience. Firstly, in many ways the cCPT mimics the resonant tunability and readout scheme generally adopted in quantum computing architectures [60], while working with a simpler circuit system. The basic structure consists of a quarter-wavelength superconducting microwave resonator (in a coplanar waveguide geometry), with non-linear tunability introduced via a Cooper pair transistor (CPT) formed using two Josephson junctions in series. Dispersive reflection measurements of the resonator via capacitive coupling to a pump/probe transmission line enable readout of the system state. Similar to the devices mentioned above, the cCPT is exposed to low-frequency charge noise due to charge traps nearby the CPT island, as well as to flux noise originating from the unpaired surface spins coupling to the SQUID loop. As the cCPT is specifically designed to be a highly sensitive electrometer/magnetometer, it is an ideal candidate for understanding and suppressing the associated effects of such $1/f$-noise commonly found in these devices. Secondly, stabilizing the resonant frequency fluctuations can elevate the cCPT into a superior charge sensing regime compared to previously reported results for the same cCPT device [15]. Ultrasensitive electrometry can aid in the realization of a macroscopic optomechanical system in the single photon-phonon strong coupling regime as proposed in [34, 61, 62, 63]. Furthermore, stabilizing against charge fluctuations can provide controllable access to the neighborhood of the Kerr-sourced bifurcation point of the cCPT, where the charge sensitivity undergoes a steep increase in magnitude [30, 64, 65].

The scheme to achieve the suppression of intrinsic bias-noise follows the well-established technique of Pound-Drever-Hall (PDH) locking, extensively used in laser optics to stabilize laser sources during cavity reflection measurements [66]. Studies reporting the successful tracking of the resonant frequency fluctuations in superconducting microwave resonators utilizing this technique are also available in the literature [67, 68, 52]. By carefully calibrating the circuit at each stage to provide maximum signal-to-noise ratio (SNR), we suppress intrinsic $1/f$-noise in the resonant frequency fluctuations over a bandwidth of 10 Hz, while driving the cavity at an average of merely a single photon. When the average photon number in the cavity is increased to $n = 10$, this bandwidth increases to 1.4 kHz.

In the conventional approach to Pound-locking in microwave cavities, an error signal is used to correct the drive frequency such that it continuously tracks the fluctuating resonance. Some of the underlying factors leading to these resonant fluctuations include the dielectric losses due to the superconducting cavity's direct coupling to its immediate environment [69], and radiation noise leading to quasiparticle poisoning in the CPT [70]. However, in general, the measured fluctuations follow a $1/f$-behavior as mentioned before, and are believed to emerge from two-level system (TLS) defects coupling through various channels into the cavity [41, 38, 71]. In the case of the cCPT and similar tunable microwave cavities, the dominant sources of these fluctuations are $1/f$-charge and flux noise coupling to the resonant frequency via its tunability. Hence, when the cCPT is tuned to regions of maximum charge/flux sensitivity, this also results in the parametric coupling of unwanted electrical and magnetic fluctuations to the microwave cavity, leading to increased resonant frequency fluctuations. Locking to a stable reference thus results in a more stable resonant frequency of the cavity, significantly improving quantum sensing in these devices.

Background Reading

The introducing sections of each chapter will contain a presentation of the background material supporting the topics of focus. However, this work constitutes concepts spanning diverse fields such as microwave engineering, quantum noise and amplification, circuit quantum electrodynamics (cQED), dynamic feedback control, low-frequency noise phenomena, and superconductivity. We therefore direct the reader to other useful references that help build the necessary background and further reading.

The concepts of microwave engineering are well-covered in the textbook by Pozar [72]. The review by Clerk *et al.* [1] provides an introduction to quantum noise, measurement and amplification, with a focus on mesoscopic detectors and amplifiers. For a deeper understanding of the concepts in quantum noise, the textbook by Gardiner and Zoller [73] may be useful. Tunnelling phenomena and Josephson junctions are discussed in depth in the textbook by Grabert and Devoret [74] and in the thesis of Joyez [75]. The field of cQED is quite vast; the review article by Blais *et al.* [76] and Schuster's thesis [77] are good starting points. The textbooks by Walls and Milburn [78], and Bowen and Milburn [79] discuss topics in quantum optics and quantum optomechanics, respectively. The microscopic origins and the detrimental effects of the ubiquitous $1/f$-noise in superconducting circuits are reviewed by Paladino *et al.* [39]. The review article by Bechhoefer *et al.* [80] should suffice to understand the feedback techniques used in this thesis work; for further reading the textbook by Frankin *et al.* [81] has detailed mathematical concepts covering dynamic feedback control.

Finally, the experimental characterization of the cCPT device used in this thesis work is extensively discussed in Brock's thesis [65], and details about the fabrication of the sample is presented in the thesis of Juliang Li [82]. Further investigations on nonlinear charge sensing properties of the cCPT can be found in the thesis work of Thyagarajan [83].

Thesis Layout

The thesis layout is as follows. In Chapter 2, we begin by addressing the first crucial component of the cCPT – a quarter-wave microwave resonator. We present a detailed analysis of the microwave resonators using a lumped element circuit method as well as using a scattering operator approach based on its quantum mechanical description. This chapter also presents practical considerations while designing the measurement configurations along with impedance matching requirements. We then move onto Chapter 3, where we discuss the open system dynamics of the cCPT using a first-principles investigation. The experimental characterization that follows verifies the validity of the model. Chapter 4 provides the theoretical framework as well as the experimental results of the feedback technique that stabilizes the resonant frequency fluctuations of tunable cavities by decoupling environmental noise. Chapter 5 addresses quantum-limited charge sensing in the theoretical limit and utilizing the feedback techniques in Ch. 4 to enhance the cCPT's performance experimentally. In Chapter 6, the future directions of the projects discussed in previous chapters are laid out in brief. Finally, we conclude this thesis by summarizing the main results in Chapter 7.

Appendices at the end will address related concepts and measurements supporting the future directions of various projects discussed in this thesis. In Appendix A, we present a discussion of the linearization of the optomechanical Hamiltonian relevant in the high photon regime. In Appendix B, the discussion moves onto the optomechanical Hamiltonian in the single-photon limit, which necessitates a completely different detection scheme compared to App. A. Appendix C provides preliminary calculations on the magnitude of the phase operator, demonstrating the need for fundamental investigations towards defining the phase operator itself in the single-photon limit. Finally in Appendix D, we illustrate through preliminary measurements a proof of concept to detect Poisson processes in real-time with high sensitivity.

Chapter 2

Quarter-wave Microwave Resonators

As a starting point, we begin our discussions by looking at a system that forms the backbone of this thesis and in fact many cQED architectures – the superconducting microwave resonator. The microwave resonators relevant for the readout schemes discussed in this thesis are implemented using a transmission line geometry. In this chapter, we will look at a few different yet related approaches to understand the physics of such microwave resonators, both in the classical and quantum limits. In particular, we will begin with a discussion of these microwave resonators in the context of a lumped-element equivalent circuit model, which is useful for analysis of measurements by room temperature equipment such as vector network analyzers [Refer to §2.1]. In §2.2, we will then discuss the two major measurement configurations used in the readout of shorted quarter-wave resonators, with and without impedance mismatch considerations. The dynamics at the sample stage requires a quantum mechanical description that motivates a discussion of the operator scattering approach in §2.3, modeled using the distributed network form of transmission lines. Finally, we will end this chapter by deriving the output power response of the quarter-wave resonator under a coherent drive [Refer to §2.4].

Section 2.1

The Lumped-element Circuit Model

Transmission lines are an integral part of many cQED architectures, functioning both as the input and output channels that carry the information to and from the sample, and as the basis for microwave resonators that enable the readout of the quantum system itself. Since the physical dimensions of these lines and resonators are comparable to the wavelengths of the signals, these structures form a distributed-parameter network where the voltage and current along the network is a function of the length; this is opposed to the lumped-element circuit case where the parameters do not vary substantially over the dimensions of the circuit elements. However, transmission line theory can be modeled from the lumped-element circuit analysis by considering the infinitesimal lengths of the line as lumped elements, which can then be extended to model these resonators as equivalent RLC circuits. An overview of these concepts and the relevant parameters are discussed in this section. For a detailed discussion, refer Pozar's textbook for microwave engineering [72].

2.1.1. Transmission Lines

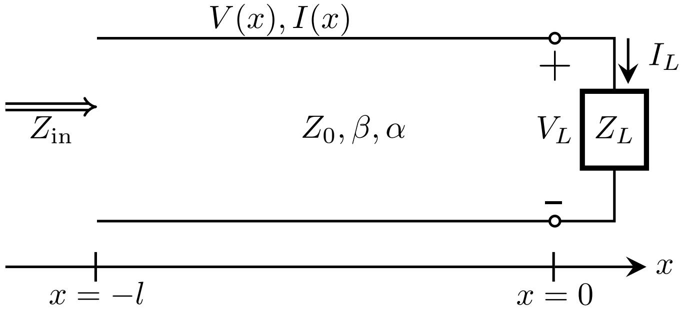

Figure 2.1: A transmission line defined by the characteristic impedance Z_0 and the complex propagation constant $\gamma = \beta + i\alpha$, terminated using a load resistor Z_L.

The major physical parameters that determines the transmission line performance (refer Fig. 2.1) are the inductance per unit length $\mathcal{L}$, the capacitance per unit length $\mathcal{C}$, the series resistance per unit length $\mathcal{R}$ that originate from the finite conductivity, and the shunt conductance per unit length $\mathcal{G}$ sourced from the dielectric losses. Since the measurement readout is via superconducting lines, the losses originating from $\mathcal{R} \to 0$. We will also use microwave resonators with high internal quality factors, where the dielectric losses contributing to $\mathcal{G}$ are also assumed to be low. The wave propagation in the steady-state condition can be solved in terms of the familiar wave equation

$$\frac{d^2F(x)}{dx^2} = \gamma^2 F(x), \tag{2.1}$$

where $F(x)$ can be either the voltage $V(x)$ or the current $I(x)$ along the line, and

$\gamma = \alpha + i\beta$ represents the complex propagation constant. Qualitatively, we can consider the solutions to $F(z)$ having a sinusoidal component determined by the reactance of the circuit with the wavelength $\lambda = 2\pi/\beta$, as well as an exponentially varying component that is determined by the resistive losses in the circuit.

An important distinction to take note is between the concepts of characteristic impedance Z_0 and the input impedance Z_{in}. The characteristic impedance is the ratio of the amplitudes of the voltage and current of a signal that is propagating along the line. This is determined by the material features and geometry of the transmission line itself and can be reduced to

$$Z_0 = \sqrt{\frac{\mathcal{L}}{\mathcal{C}}} \tag{2.2}$$

for the lossless case. However, the ratio of the voltage to the current at length l which is a measure of the impedance seen looking into the line, is defined as the input impedance. Along with the magnitude of Z_0, Z_{in} is also a function of the load resistor Z_L that terminates the line. In short, the input impedance of a lossy transmission line of length l, characteristic impedance Z_0, complex propagation constant γ and a load impedance Z_L is given by

$$Z_{\text{in}} = Z_0 \frac{Z_L + Z_0 \tanh \gamma l}{Z_0 + Z_L \tanh \gamma l}. \tag{2.3}$$

A terminated transmission line with $Z_L \neq Z_0$ also results in the generation of reflected waves to satisfy the condition of energy conservation. The voltage reflection coefficient Γ is defined as the ratio of the outgoing (left propagating) voltage amplitude to the incident (right propagating) voltage amplitude. The measurement of the reflection coefficient, as we will see in the upcoming chapters, is an extremely useful quantity that captures the information relevant to various detection schemes. It can be expressed in terms of Z_0 and Z_L as

$$\Gamma = \frac{Z_L - Z_0}{Z_L + Z_0}. \tag{2.4}$$

The trivial cases are $\Gamma = -1$ for $Z_L = 0$, $\Gamma = 1$ for $Z_L = \infty$, and $\Gamma = 0$ for $Z_L = Z_0$. Hence when the load is matched, the signal continues propagating along the line without forming standing waves leading to an infinite return loss given by RL = -20 $\log|\Gamma|$ dB. This concept lies at the heart of the readout schemes, enabling transfer of information to and from the sample without significant losses along the way.

2.1.2. Unloaded Quarter-wave Microwave Resonators

For a shorted quarter-wave ($\lambda/4$-wave) resonator, the transmission line parameters introduced in the previous discussion correspond to $Z_L = 0$ and $l = \lambda/4$, resulting in an input impedance of $Z_{\text{in}} = Z_0 \tanh \gamma l$. Expanding the complex propagation constant γ about resonance $\omega_{\lambda/4}$ for a low-loss transmission line with phase velocity v_p, with $\beta = (\omega_{\lambda/4} + \ \delta\omega)/v_p$ and $\tanh \alpha l \approx \alpha l$, we obtain the input impedance as

$$Z_{\text{in}} = \frac{Z_0}{\alpha l + i\pi\delta\omega/2\omega_{\lambda/4}}. \tag{2.5}$$

The above expression is equivalent to the input impedance about resonance of a parallel RLC circuit with the corresponding parameters $R = Z_0/\alpha l$, $C = \pi/4Z_0\omega_{\lambda/4}$ and $L = 1/\omega_{\lambda/4}^2 C$. We can thus apply lumped-element circuit methods for modeling systems involving unloaded shorted $\lambda/4$-wave resonators by reducing these resonators to parallel RLC circuits. Note that the input impedance at resonance corresponds to the maximum value $Z_0/\alpha l$ in this case. As a result, a shorted $\lambda/4$-wave resonator forms a rejector circuit with minimal current flow at the resonant frequency. Moreover, the resonant frequencies of the cavity occur where the cavity length equals multiples of the quarter wavelength corresponding to the fundamental resonance and are given by $\omega_{\lambda/4} = (2n+1)\pi v_p/2l$, where $n = 0, 1, 2 \ldots$.

Another important parameter of interest while considering resonant circuits is the rate at which information is gained/lost at resonance. This quantity defined as the quality factor Q is given by

$$Q = \omega \frac{\text{average energy stored}}{\text{energy loss (or gain)/second}}. \tag{2.6}$$

For resonator circuits exposed to dielectric, conductor and radiation losses, we assign an internal quality factor $Q_{\text{int}} = \pi/4\alpha l$ (for $\lambda/4$-wave resonators) to describe channels through which useful information is lost. This is also interchangeably used with the concept of internal damping rate κ_{int} given by $\omega_{\lambda/4}/Q_{\text{int}}$, and corresponds to the internal linewidth of the resonator.

2.1.3. Loaded Quarter-wave Microwave Resonators

In order to facilitate readout, we typically couple the resonators to another transmission line (of $Z_0^{(p)}$ characteristic impedance) either capacitively or inductively. A $\lambda/4$-wave resonator (of $Z_0^{(r)}$ characteristic impedance) weakly coupled to a pump/probe transmission line via a coupling capacitance $C_{pc} \ll C$ collects/provides information at an external damping rate κ_{ext} and can be equivalently described using its external quality factor Q_{ext}.

The sum of the average electric and magnetic energies stored is twice the energy stored on the capacitor of the resonator: $E_{\text{avg}} = 2 * \frac{1}{2} C \langle V^2 \rangle$. The average power flow P_{avg} into the transmission line via C_{pc} is $P_{\text{avg}} = \langle I^2 \rangle\, Z_0^{(p)}$, where $I = \omega C_{pc} V$. Hence we obtain Q_{ext} as

$$Q_{\text{ext}} = \omega \, \frac{\frac{\pi}{4\omega_{\lambda/4} Z_0^{(r)}} \langle V^2 \rangle}{\omega^2 C_{pc}^2 \langle V^2 \rangle Z_0^{(p)}} = \frac{\pi}{4\left(\omega C_{pc}\sqrt{Z_0^{(r)} Z_0^{(p)}}\right)^2} \frac{\omega}{\omega_{\lambda/4}}. \tag{2.7}$$

The total damping rate κ_{tot} of the resonator thus has two effective channels through which energy transfer occurs, and is given by $\kappa_{\text{tot}} = \kappa_{\text{int}} + \kappa_{\text{ext}}$. The net quality factor becomes

$$\frac{1}{Q_{\text{tot}}} = \frac{1}{Q_{\text{int}}} + \frac{1}{Q_{\text{ext}}}. \tag{2.8}$$

The coupling capacitance also leads to an added impedance and consequently a shifted resonance of the cavity ω_n obtained through the condition

$$\mathbb{Im}\left(Z_{\text{in}}|_{\omega=\omega_n}\right) = \mathbb{Im}\left(-\frac{i}{\omega_n C_{pc}} + Z_{\text{in}}^{\lambda/4}(\omega_n)\right) = 0, \tag{2.9}$$

where $Z_{\text{in}}^{\lambda/4}$ is the input impedance contribution from the unloaded resonator.

Defining $\Omega \equiv \omega_n - \omega_{\lambda/4}$, we get

$$\mathbb{Im}\left(-\frac{i}{\omega_n C_{pc}} + \frac{4Z_0^{(r)} Q_{\text{int}}/\pi}{1 + 2iQ_{\text{int}}\Omega/\omega_{\lambda/4}}\right) = 0. \tag{2.10}$$

The above condition leads to a quadratic equation

$$\frac{4Q_{\text{int}}^2}{\omega_{\lambda/4}^2}\,\Omega^2 + \frac{8Z_0^{(r)}\omega_n C_{pc} Q_{\text{int}}^2}{\pi\omega_{\lambda/4}}\,\Omega + 1 = 0, \tag{2.11}$$

with solutions

$$\Omega = -\frac{2Z_0^{(r)}\omega_n C_{pc}\omega_{\lambda/4}}{\pi} \quad \text{and} \quad \Omega = -\frac{\pi\omega_{\lambda/4}}{8Z_0^{(r)}\omega_n C_{pc} Q_{\text{int}}^2} \tag{2.12}$$

Table 2.1: Parameter values used in the design of $\lambda/4$-wave resonator.

Parameter	Value
Characteristic impedance $Z_0^{(r)}$	50 Ω
Resonant frequency $\omega_{\lambda/4}$	5.83 GHz

Parameter	Value
Internal quality factor Q_{int}	10^4
Coupling capacitance C_{pc}	10 fF

under the condition of weak coupling and high Q_{int}.

Note that for the typical values of resonator parameters given in Table 2.1, the renormalized second root of the resonance in the above expression Eq. (2.12) is very close to the original value $\omega_{\lambda/4}$ (with a shift of the order of MHz), thus corresponding to a high resulting impedance (as discussed in terms of the rejector circuit in §2.1.2) and is of little interest. However, the resulting input impedance corresponding to the first root in Eq. (2.12) is given by [84]

$$Z_{\text{in}}(\omega) \approx \frac{\pi}{4Z_0^{(r)} Q_{\text{int}} (\omega_n C_{pc})^2} \left(1 + 2iQ_{\text{int}} \frac{\delta\omega}{\omega_n}\right), \tag{2.13}$$

where $\delta\omega \equiv \omega - \omega_n$ and $\omega_0^{-1} \approx \omega_{\lambda/4}^{-1}$. The above expression can be further simplified in terms of external coupling derived in Eq. (2.7) into

$$Z_{\text{in}}(\omega) \approx Z_0^{(p)} \frac{Q_{\text{ext}}}{Q_{\text{int}}} \left(1 + 2iQ_{\text{int}} \frac{\delta\omega}{\omega_0}\right). \tag{2.14}$$

Comparing this input impedance to a lumped-element circuit, we obtain the equivalent model for the loaded $\lambda/4$-wave resonator as a series RLC circuit in this configuration, with parameters given by $R = Z_0^{(p)} Q_{\text{ext}}/Q_{\text{int}}$, $L = Z_0^{(p)} Q_{\text{ext}}/\omega_n$ and $C = (\omega_n^2 L)^{-1}$. As the input impedance is minimum at resonance, this configuration thus leads to an acceptor circuit (where the signal enters the cavity due to its low impedance) and can be further utilized in readout schemes to extract information about the system using reflection coefficient measurements.

Finally, we may also obtain the simplified form of the renormalized resonant frequency of a $\lambda/4$-wave resonator in the weak coupling limit as

$$\omega_n \approx \omega_{\lambda/4} \left(1 - \frac{C_{pc}}{2C}\right), \, n = 0, 1, 2 \ldots, \tag{2.15}$$

where we have used the first root obtained in Eq. (2.12) as the resonance shift. We will primarily be operating the resonator in its fundamental mode where the relative variation in the external quality factor is small near resonance: $\Delta Q_{\mathrm{ext}}(\omega)/Q_{\mathrm{ext}}(\omega_0) \ll 1$. This allows us to work under the first Markov approximation of considering the external damping rate to be constant over the frequency region of interest, a frequently used simplification in modeling input-output relations in cQED systems, as will be clarified in future discussions.

Section 2.2

Measurement Configuration

One crucial step in the microwave readout is the efficient isolation of the incoming and outgoing signal components. This is accomplished typically using microwave circulators and isolators, as well as by the careful design of the resonator-transmission line interface. In this section, we present a discussion of the transmission or reflection measurements in a quarter-wave resonator which can be done using two different configurations [56]. When the resonator is capacitively coupled to a single transmission line that simultaneously acts as the pump and probe, the isolation of these signals are achieved using a circulator at a later stage (Refer Fig. 2.2a). Another useful configuration is when the resonator is connected to a transmission feedline in a hanger geometry. This necessitates a pass-by transmission measurement where the input signal interacts with the resonator near its resonance frequency as shown in Fig. 2.2b. We will also address the impedance matching requirements in these two configurations that is essential for the accurate readout of the resonator characteristics.

2.2.1. Reflection Measurement in a Shorted Quarter-wave Resonator

As mentioned above, one approach to achieve reflection measurement in a shorted quarter-wave resonator is illustrated in Fig. 2.2a. We will look at a detailed derivation of the reflection coefficient here; this will prove useful towards the impedance-mismatched case in the subsequent discussions.

As shown in Fig. 2.3, the circulator divides the circuit into two loops. Loop 1 can be used to extract the signal reflected off the load into port 2 of the circulator, which then enters port 3 and can be measured as V_{out}, through Loop 2 [72]. The load resistor Z_L corresponding to the loaded $\lambda/4$-wave resonator with impedance given by Eq. (2.14) is placed at $x = 0$. At $x = -l$, the reflected signal enters port 2 of circulator. The steady-state, general solution (at time t_0) for the voltage

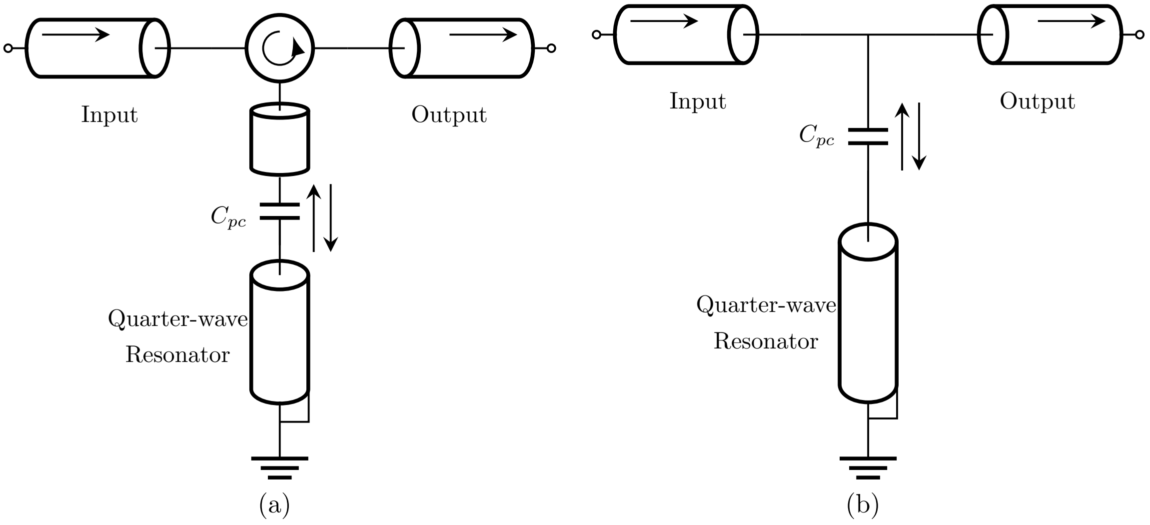

Figure 2.2: (a) Configuration using a circulator for reflection measurement S_{11} in a quarter-wave resonator. (b) Corresponding hanger configuration.

wave equation, given in Eq. (2.1), considering both the left and right propagating components can be expressed as

$$V(x) = V_0^+ \left(e^{-i\beta x} + \Gamma e^{i\beta x}\right), \tag{2.16}$$

where V_0^+ is the input voltage amplitude, $\Gamma = (Z_L - Z_0)/(Z_L + Z_0)$ is the reflection coefficient and we neglect resistive losses ($\alpha \to 0$) inside pump/probe transmission line. Hence at $x = -l$,

$$V(-l) = V_0^+ \left(e^{i\beta l} + \Gamma e^{-i\beta l}\right) \tag{2.17}$$

and at $x = 0$,

$$V_L \equiv V(0) = V_0^+(1 + \Gamma). \tag{2.18}$$

Using Kirchoff's law in Loop 1, we get the voltage-dividing components V_L and $V(x = -l)$ as

$$V_L = V_g \frac{Z_L}{Z_0 + Z_L} \qquad \text{and} \qquad V(x = -l) = V_g \frac{Z_{\text{in}}(x = -l)}{Z_0 + Z_{\text{in}}(x = -l)}, \tag{2.19}$$

where $Z_{\text{in}}(x = -l)$ is the input impedance at the circulator port 2 seen looking

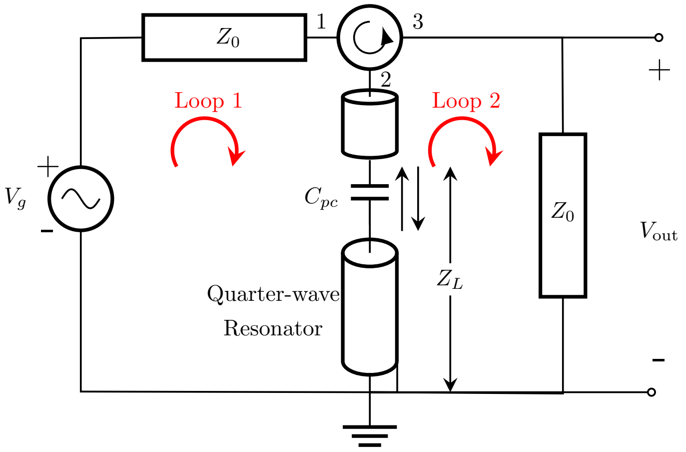

Figure 2.3: Readout scheme for a quarter-wave resonator in reflection mode. Circulator effectively separates the circuit to two separate loops.

towards the resonator, and is given by

$$Z_{\text{in}}(x=-l) = \frac{V(x=-l)}{I(x=-l)} = Z_0 \frac{V_0^+\left(e^{i\beta l} + \Gamma e^{-i\beta l}\right)}{V_0^+\left(e^{i\beta l} - \Gamma e^{-i\beta l}\right)}. \tag{2.20}$$

A bit of algebra combining expressions for $V(x=-l)$ in Eqs. (2.17) and (2.19) then provides the relation $V_0^+ = V_g e^{-i\beta l}/2$. The signal coming out of port 2 of the circulator can thus be measured at the output via Loop 2, and can be expressed as

$$V_{\text{out}} = V_0^+ \Gamma e^{-2i\beta l} = \frac{V_g}{2} \Gamma e^{-2i\beta l}. \tag{2.21}$$

A vector network analyzer can be thus be used to measure the reflection coefficient of the resonator via a signal input V_g through port 1 and a measurement at port 2 (phase delay is adjusted using calibration at the instrument stage). In short, the scattering matrix coefficient S_{21} is given by

$$S_{21} = \frac{2V_{\text{out}}}{V_g} = \Gamma. \tag{2.22}$$

Applying the expression for Z_L from Eq. (2.14) (with $Z_0^{(p)} = Z_0$) to $\Gamma = (Z_L - Z_0)/(Z_L + Z_0)$, the magnitude and phase of $S_{21}(\delta\omega)$ is obtained from

$$S_{21}(\delta\omega) = \frac{2i\delta\omega + (\kappa_{\text{int}} - \kappa_{\text{ext}})}{2i\delta\omega + (\kappa_{\text{int}} + \kappa_{\text{ext}})}, \tag{2.23}$$

The expression can be transformed in the inverse complex plane as

$$\tilde{S}_{21} \equiv 2\left(S_{21}+1\right)^{-1} = \left(1+\frac{Z_0}{Z_r}\right) = 1+\frac{\kappa_{\text{ext}}}{\kappa_{\text{int}}}\left(\frac{1}{1+2i\delta\omega/\kappa_{\text{int}}}\right). \tag{2.24}$$

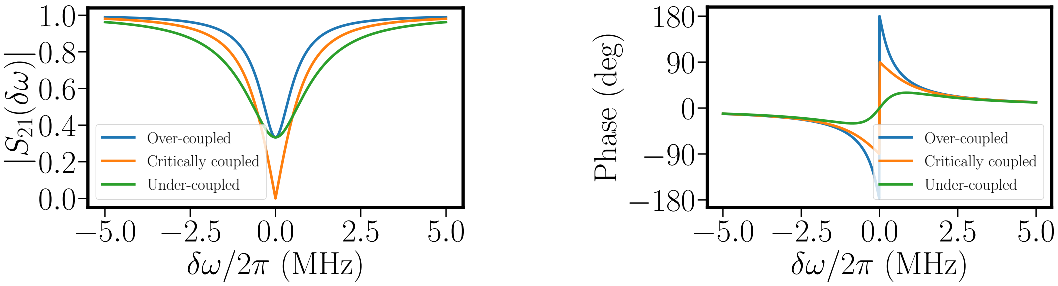

(a) (b)

Figure 2.4: (a) Magnitude of the reflection coefficient in the different coupling regimes. (b) Corresponding phase response of the reflection coefficient.

The resonator parameters ω_0, κ_{int} and κ_{ext} can be extracted either through Eq. (2.23) [65] or Eq. (2.24) [85]. The magnitude and phase of the reflection coefficient in Eq. (2.23) are plotted in Fig. 2.4. In the S_{21} plane, the reflection traces a circle with the off-resonance value at unity and the resonance corresponding to the other intercept on the real axis, as displayed in Fig. 2.5a. Depending on the coupling ratio $\xi = \kappa_{\text{ext}}/\kappa_{\text{int}} = Q_{\text{int}}/Q_{\text{ext}}$, the resonance lies on the negative real axis for $\xi > 1$ (over-coupled), positive real axis for $\xi < 1$ (under-coupled) or origin for $\xi = 0$ (critically coupled). The diameter is given by $D = 2\kappa_{\text{ext}}/\kappa_{\text{tot}}$. Also, the corresponding points for $|\delta\omega| = \kappa_{\text{tot}}/2$ form a diameter perpendicular to the real-axis giving the 3 dB points of the loaded resonator.

In the $\tilde{S}_{21}$ plane, the trajectory remains a circle with off-resonance and resonance value on the positive real axis, as displayed in Fig. 2.5b. The value at resonance is $S_{21} > 2$ for $\xi > 1$ (over-coupled), $S_{21} < 2$ for $\xi < 1$ (under-coupled) or $S_{21} = 2$ for $\xi = 0$ (critically coupled). The diameter is given by the coupling factor $D = \xi$. Finally, the corresponding points for $|\delta\omega| = \kappa_{\text{int}}/2$ join perpendicular to the real-axis directly extracting the 3 dB points of the unloaded resonator.

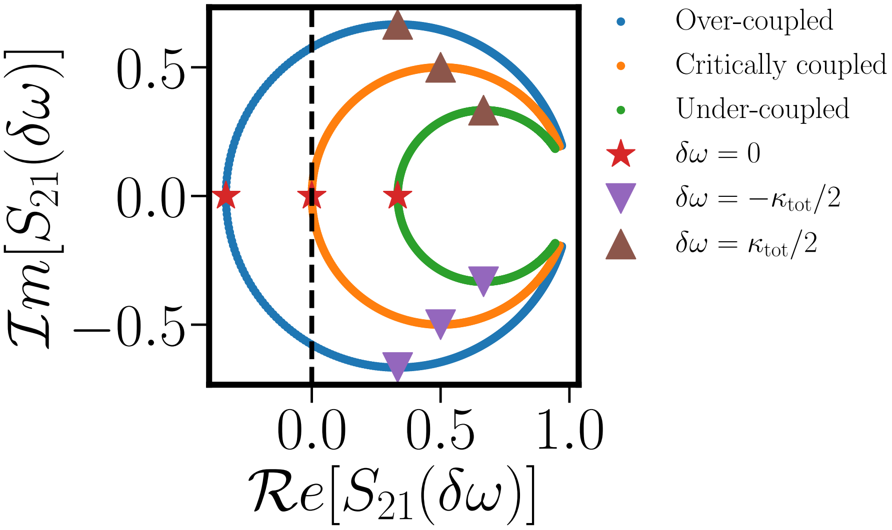

(a)

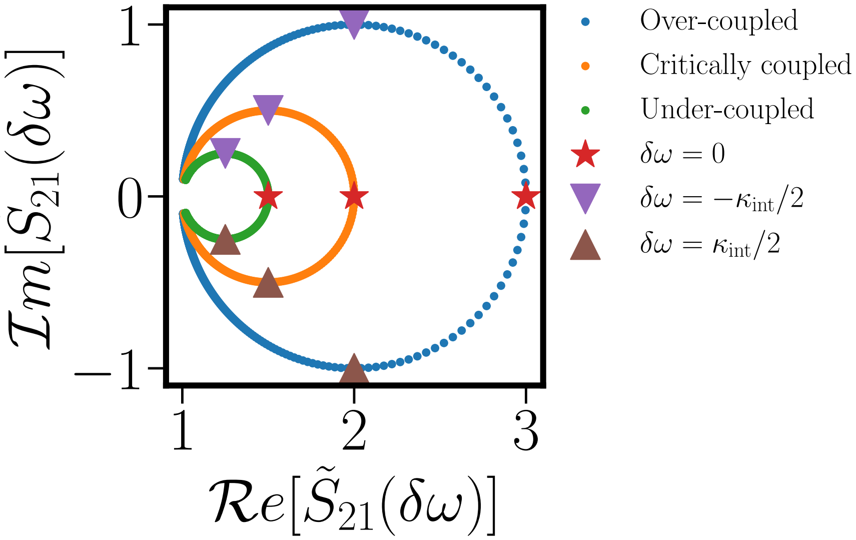

(b)

Figure 2.5: (a) Trajectory of the reflection coefficient $S_{21}(\delta\omega)$ in the complex plane in different coupling regimes. The relevant parameters of the resonator can be extracted from the circle's features. (b) Trajectory of $\tilde{S}_{21}(\delta\omega)$ in the inverse complex plane and the corresponding resonator parameter extraction using the circle.

2.2.2. Pass-by Measurement in a Shorted Quarter-wave Resonator

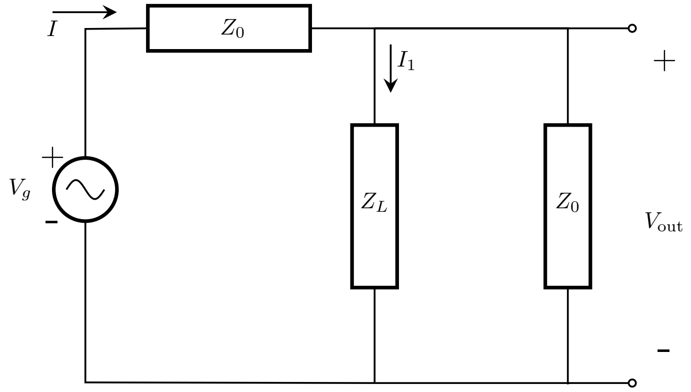

Figure 2.6: Readout scheme for a quarter-wave resonator in hanger mode. The signal passes-by off-resonance and enters the resonator only near resonance.

This analysis follows the description provided in [85]. Transmission in a resonator with loaded input impedance $Z_{\text{in}} = Z_L$ can be measured using the configuration provided in Fig 2.6. The total current I, current through the resonator I_1, and the output voltage V_{out} are given by

$$I = \frac{V_g}{Z_0 + \left(\frac{Z_0 Z_{\text{in}}}{Z_0 + Z_{\text{in}}}\right)} \tag{2.25}$$

$$I_1 = \frac{I}{1 + Z_{\text{in}}/Z_0} \tag{2.26}$$

$$V_{\text{out}} = I_1 Z_{\text{in}} = \frac{V_g}{2\left(1 + Z_0/2Z_{\text{in}}\right)} \tag{2.27}$$

Note that as $Z_{\text{in}} \to \infty$, $S_{21} = 1$ as the signal will merely pass-by the transmission feedline without entering resonator. Hence,

$$S_{21} = \frac{2V_{\text{out}}}{V_g} = \frac{1}{1 + Z_0/2Z_{\text{in}}}. \tag{2.28}$$

In our specific case of quarter-wave resonator, $Z_L = Z_{\text{in}}$ is obtained from Eq. (2.14). However, $Z_0^{(p)}$ in this configuration is given by $Z_0/2$ since the resonator sees two transmission lines in parallel at the interface. Thus a measurement in the vector network analyzer provides

$$S_{21} = \left[1 + \frac{\kappa_{\text{ext}}}{\kappa_{\text{int}}}\left(\frac{1}{1 + 2i\delta\omega/\kappa_{\text{int}}}\right)\right]^{-1} \tag{2.29}$$

In the inverse plane, $\tilde{S}_{21} \equiv S_{21}^{-1}$ again traces a circle with off-resonance value at unity and resonance corresponding to the intercept on the real axis, with the parameters extracted as shown in Fig. 2.5b.

2.2.3. Measurements in Impedance-mismatched Circuits

In practice, the measurement circuitry generally undergoes an impedance mismatch that could arise due to imperfect sample mounting, as well as due to circulator and amplifier return losses. This distorts the transmission/reflection measurement and makes it less ideal to analyze the resonance as described in previous sections.

For a pass-by transmission, an extended analysis is described in Megreant's paper [85] where the impedance mismatch add ΔZ_1 and ΔZ_2 at the input and output lines, respectively, as given in Fig. 2.7a. Following the same analysis in subsection 2.2.2, the modified expression for S_{21} is given by

$$S_{21} = \frac{2Z_0}{Z_1 + Z_2} \frac{1}{1 + Z/2Z_{\text{in}}} \tag{2.30}$$

where $Z_i = Z_0 + \Delta Z_i$ for $i = 1, 2$ and $2/Z \equiv 1/Z_1 + 1/Z_2$. The constant $2Z_0/(Z_1 + Z_2)$ gets absorbed in an off-resonance calibration, and as before, in the inverse plane,

$$\tilde{S}_{21} \equiv S_{21}^{-1} = 1 + \frac{\kappa_{\text{ext}}^*}{\kappa_{\text{int}}} e^{i\phi} \frac{1}{1 + 2i\delta\omega/\kappa_{\text{int}}}, \tag{2.31}$$

where $Z = |Z|e^{i\phi}$ and $\kappa_{\text{ext}}^* \equiv (|Z|/Z_0)\kappa_{\text{ext}}$. The center of the circle thus gets rotated by an angle ϕ, with the effective diameter $D = \kappa_{\text{ext}}^*/\kappa_{\text{int}}$, as shown in Fig. 2.8a. This limits the accuracy with which we can extract the external damping factor in an impedance-mismatched circuit.

For the case of reflection measurement in the circulator configuration, we can extend the analysis in subsection 2.2.1 to include the impedance mismatch parameters (Refer Fig. 2.7b). We will consider a sample mount imperfection that introduces a ΔZ_1 into the load impedance, and an amplifier return loss that adds ΔZ_2. Note that the nonreciprocity and impedance matching in circulators is an intense field of research by itself [86], but this is not taken into consideration in the following simplified approach.

The modified reflection coefficient $\Gamma' = (Z_L' - Z_0)/(Z_L' + Z_0)$ where $Z_L' = Z_L + \Delta Z_1$. At $x = 0$,

$$V_L' \equiv V(0) = V_0^+(1 + \Gamma'), \tag{2.32}$$

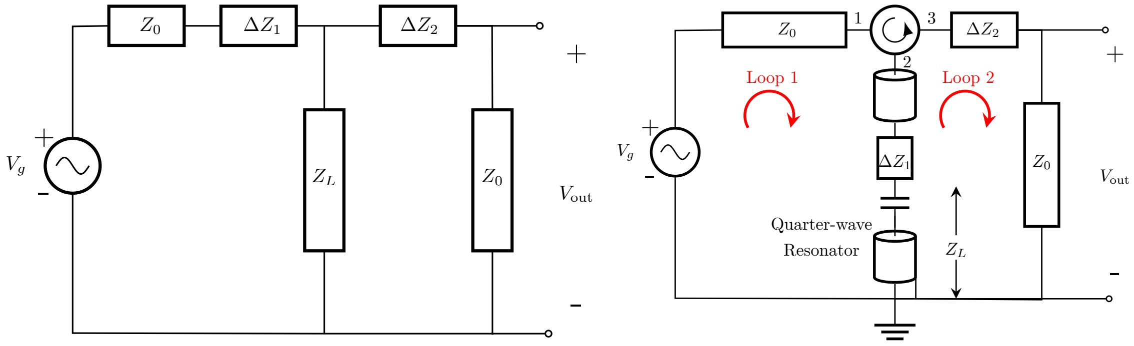

(a) (b)

Figure 2.7: (a) Equivalent hanger-mode circuit diagram with impedance mismatch losses. (b) Corresponding circuit diagram for single pump/probe line.

and Kirchoff's law gives

$$V_L' = V_g \frac{Z_L'}{Z_0 + Z_L'}. \tag{2.33}$$

As before, we can then find the modified signal entering port 3 of circulator and the net $V_{\text{out}} = V_0^+ \Gamma' (Z_0/Z_2)$, where $Z_2 \equiv Z_0 + \Delta Z_2$ (the phase delay of $e^{-2i\beta l}$ is ignored). The final expression for V_{out} becomes

$$V_{\text{out}} = \frac{V_g}{2} \frac{Z_0}{Z_2} \frac{Z_L' - Z_0}{Z_L' + Z_0}, \tag{2.34}$$

and the reflection coefficient S_{21} is given by

$$S_{21} = \frac{2V_{\text{out}}}{V_g} = \frac{Z_0}{Z_2} \frac{Z_L' - Z_0}{Z_L' + Z_0}. \tag{2.35}$$

The factor of (Z_0/Z_2) can be obtained using an off-resonance calibration, and defining $\tilde{S}_{21} \equiv 2\left[(Z_2/Z_0) S_{21} + 1\right]^{-1}$, we get

$$\tilde{S}_{21} = \left(1 + \frac{Z_0}{Z_L'}\right). \tag{2.36}$$

In short, the modified $\tilde{S}_{21}$ takes the form

$$\tilde{S}_{21} = 1 + \frac{\kappa_{\text{ext}}}{\kappa_{\text{int}}^*} \frac{1}{1 + 2i\delta\omega/\kappa_{\text{int}}^*,} \tag{2.37}$$

where for $\Delta Z_1/Z_0 = \epsilon e^{i\phi}$, the resonance frequency shifts from $\omega_0 \to \omega_0 - \epsilon\kappa_{\text{ext}} \sin\phi/2$,

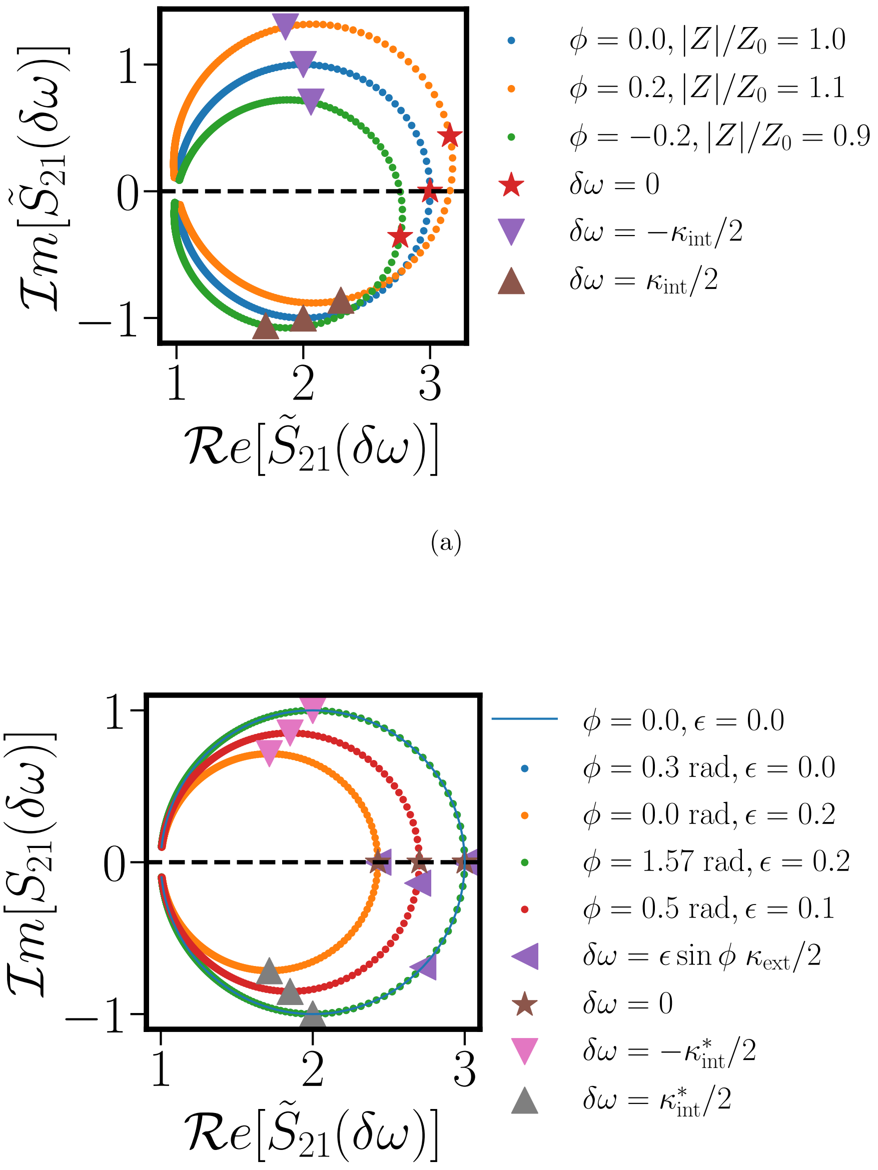

(a)

(b)

Figure 2.8: (a) $\tilde{S}_{21} = S_{21}^{-1}$ plotted in the over-coupled regime for different impedance mismatched values. Rotation of the circle occurs in the direction of ϕ, and the diameter is modified due to rescaling of the external damping rate. (b) Impedance mismatch affecting $\tilde{S}_{21}$ in a single pump/probe transmission line setup. The resonance is shifted due to the reactance component in ΔZ_1, and the diameter and measured internal damping rate changes in presence of a resistive element. The original resonance frequency is denoted by the left-pointing triangles.

and the internal damping rate is rescaled from $\kappa_{\text{int}} \rightarrow \kappa^*_{\text{int}} = \kappa_{\text{int}}(1+\xi\epsilon\cos\phi)$. Thus an impedance mismatch caused purely due to reactance causes a shift in the measured resonance frequency of the resonator, and an impedance mismatch that is purely resistive rescales the value of the measured internal damping rate. This is illustrated in Fig. 2.8b.

2.2.4. Comparison of Measurement Configurations

The hanger geometry is a useful configuration that allows simultaneous readout of multiple resonators using frequency-domain multiplexing through a single feedline [87]. This configuration has the disadvantage that the information at the interface is not completely available as there are two channels through which the signal can propagate. This is not the case in a single pump/probe transmission line discussed in 2.2.1, where the entire signal is available for readout. This however implies the addition of an extra circulator in the circuit can create stray magnetic fields, as well as adds a bulky component in the cryogenic setup. The device used in this thesis work will utilize the combined pump/probe transmission line configuration.

2.2.5. Experimental Data

Here we provide a comparison between the two analyses that extracts the resonator parameters coupled to a single transmission line (Refer Fig. 2.9). The impedance mismatch in actuality manifests as a rotation of the circle. This is believed to be caused due to the return losses at the circulator interface.

Section 2.3

Quantum Mechanical Description of Microwave Resonators

The classical description of the microwave resonators discussed in the previous sections is useful for measurement analysis at the room temperature stage where the signal is typically of the order of nWs and higher. However, at the cryogenic stage, we drive the resonator itself at the order of 1-100 photons. Since the thermal fluctuations at this stage are negligible compared to the energy of even a single photon, we require a detailed quantum mechanical description of the microwave resonator, where the open system dynamics is explained using the quantized Hamiltonian of the cavity-transmission line interaction. In this section, we will begin with an overview

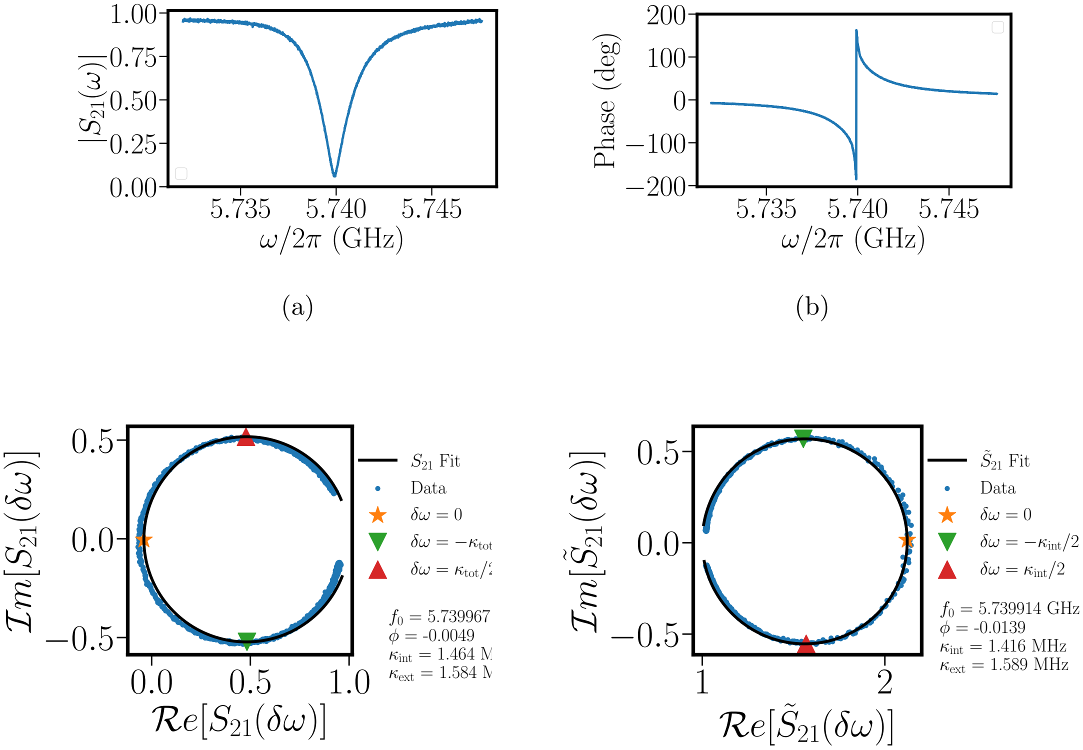

(a) (b)

(c) (d)

Figure 2.9: (a) Magnitude of the reflection coefficient of a bare cavity with resonance near 5.74 GHz. (b) Corresponding phase response of the reflection coefficient. (c) Trajectory of the reflection coefficient $S_{21}(\delta\omega)$ in the complex plane and the extracted values of resonator parameters as per the model in Eq. (2.23) (d) Trajectory in the inverse complex plane and the corresponding resonator parameter extraction using the model in Eq. (2.24). Note an extra rotation of the circle due to the circulator impedance mismatch not accounted for in 2.2.3.

of these concepts (for the sake of an impatient reader). The subsequent discussions will cover a first-principles, scattering operator approach that provides a fundamental description of the resonator-transmission line dynamics. This will prove useful for describing the cCPT dynamics and charge sensitivity derivation presented in later chapters. The reviews by Blais *et al.* [76], Vool *et al.* [88], and Devoret *et al.* [89] are all useful references that provide a detailed overview of the concepts in circuit quantum electrodynamics (cQED).

2.3.1. An Overview

As already discussed in previous sections, the electromagnetic environment inside a microwave resonator formed using a transmission line of characteristic impedance $Z_0 = \sqrt{L/C}$ is modeled by a LC resonator that is exposed to internal and external resistive losses. The Hamiltonian of the quantum LC resonator is given by

$$H_{LC} = \frac{\hat{Q}^2}{2C} + \frac{1}{2}C\omega_0^2\hat{\Phi}^2, \tag{2.38}$$

where $\hat{Q}$ is the charge on the mode capacitor C and $\hat{\Phi}$ is the flux threading the mode inductor L. We have only accounted for a single mode here but the generalized H_{LC} will contain $n = 0, 1, 2, \ldots$ discrete modes that satisfies the boundary conditions of the resonator.

The above expression is also written using these specific coordinates so that the magnetic energy component given by the second term is analogous to the potential energy of a mechanical oscillator with position corresponding to the flux coordinate $\hat{\Phi}$, and the electric energy in the first term corresponds to the kinetic energy, expressed in terms of the conjugate momentum $\hat{Q}$. Note that this convention helps in the future derivations involving addition of the CPT's perturbative component to the Hamiltonian. We can also instead work with the swapped coordinate system considering $\hat{\Phi}$ as the conjugate momentum.

Taking the analogy with the mechanical oscillator further, we recognize the noncommutativity of these two observables via the expression

$$\left[\hat{\Phi}, \hat{Q}\right] = i\hbar. \tag{2.39}$$

In terms of the creation and annihilation operators $\hat{a}^\dagger$ and $\hat{a}$, the generalized coordinates may be rewritten as

$$\hat{\Phi} = \hat{\Phi}_{zp}\left(a^{\dagger} + \hat{a}\right) \qquad\qquad \hat{Q} = i\hat{Q}_{zp}\left(a_n^{\dagger} - \hat{a}\right), \tag{2.40}$$

where the zero-point fluctuations of the flux and charge are given by $\hat{\Phi}_{zp} = \sqrt{\hbar/2\omega_0 C}$ and $\hat{Q}_{zp} = \sqrt{\hbar\omega_0 C/2}$, respectively. The Hamiltonian takes the familiar form (again considering only the fundamental mode):

$$H_{LC} \;=\; \hbar\omega_0\left(\hat{a}^{\dagger}\hat{a} + \frac{1}{2}\right). \tag{2.41}$$

The Hamiltonian of a semi-infinite transmission line (acting as the pump/probe line) consists of a bath of such harmonic oscillators discussed above, where the boundary condition now allows a continuum of modes, with the resulting Hamiltonian given by

$$H_p = \hbar\int_0^{\infty} d\omega\omega\left(\hat{a}_p^{\mathrm{in}}(\omega)\right)^{\dagger}\hat{a}_p^{\mathrm{in}}(\omega), \tag{2.42}$$

where each of the mode operators satisfy the commutation relation

$$\left[\hat{a}_p^{\mathrm{in}}(\omega), \left(\hat{a}_p^{\mathrm{in}}(\omega')\right)^{\dagger}\right] = \delta(\omega - \omega'). \tag{2.43}$$

Finally, the interaction between the pump/probe line and the cavity resonator via the coupling capacitance is generally described using input-output formalism [90]. This assumes a linear interaction (by means of weak coupling between the in/out line and cavity) where the net Hamiltonian of the open system takes the form

$$H = H_{LC} + H_p + H_{(interact)}, \tag{2.44}$$

where H_{LC} and H_p are given by Eqs. (2.41) and (2.42), respectively. The interaction Hamiltonian can be expressed as

$$H_{(interact)} = i\hbar\int_{-\infty}^{\infty} d\omega\omega\kappa_{\mathrm{ext}}\left[\left(\hat{a}_p^{\mathrm{in}}(\omega)\right)^{\dagger}\hat{a} - \hat{a}^{\dagger}\hat{a}_p^{\mathrm{in}}(\omega)\right], \tag{2.45}$$

where κ_{ext} is the external damping rate which is assumed to be a constant and independent of frequency (essentially the first Markov approximation). Note that the limits of the integral also include the negative frequency range to account for both left and right propagating modes. The internal losses are modeled as a second, internal thermal bath that corresponds to an internal damping rate κ_{int}, which accounts for the resistive losses inside the cavity.

The steady-state system dynamics can be obtained from the standard quantum-Langevin equation (in the time domain)

$$\dot{\hat{a}}(t) = -i\omega_0(t)\hat{a}(t) - \frac{\kappa_{\text{tot}}}{2}\hat{a}(t) - i\sqrt{\kappa_{\text{ext}}}\hat{a}_p^{\text{in}}(t), \tag{2.46}$$

where we have not included the contribution from the internal bath operator. Combining both the input and output going fields, we obtain

$$\hat{a}_p^{\text{out}}(\omega) = \hat{a}_p^{\text{in}}(\omega) - i\sqrt{\kappa_{\text{ext}}}\hat{a}(\omega), \tag{2.47}$$

the standard input-output relation in Fourier domain for the cavity undergoing a reflection mode measurement.

Combining Eq. (2.47), the solution to Eq. (2.46) in the Fourier domain, and adding κ_{int} as a second interactive bath dynamics, we may also obtain the reflection coefficient $r(\omega) = \hat{a}_p^{\text{out}}(\omega)/\hat{a}_p^{\text{in}}(\omega)$, that results in the same expression as Eq. (2.23):

$$r(\omega) = \frac{2i(\omega - \omega_0) + (\kappa_{\text{int}} - \kappa_{\text{ext}})}{2i(\omega - \omega_0) + (\kappa_{\text{int}} + \kappa_{\text{ext}})}. \tag{2.48}$$

2.3.2. Operator Scattering Approach [1]

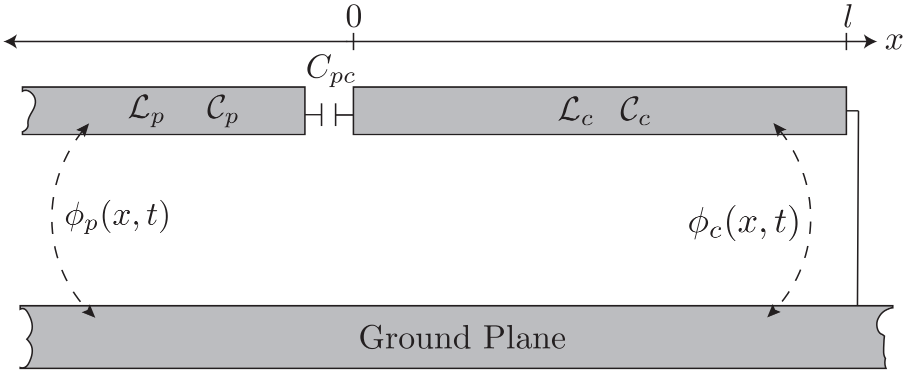

Figure 2.10: Circuit schematic of a bare quarter-wave ($\lambda/4$) cavity coupled to a pump/probe transmission line via a coupling capacitor C_{pc}.

---

[1] We acknowledge that the bulk of this section is reproduced from a Journal of Applied Physics publication by Kanhirathingal *et. al.* [13], with major contributions from Prof. Blencowe.

In this subsection, we present a detailed, first-principles derivation of a shorted quarter-wave resonator weakly coupled to a pump/probe transmission line via a capacitance C_{pc} (Fig. 2.10). The dynamics of this model is well-established using the input-output formalism, as presented as an overview in 2.3.1. The standard input-output theory considers the damping rates due to internal losses and coupling to the transmission line as phenomenological parameters during the derivation [90]. In the following, we shall instead apply the operator scattering approach [91, 88], where we systematically recover the discrete mode cavity operators that define the cavity Hamiltonian, together with the cavity mode renormalized frequencies and external damping rates due to the coupling to the transmission line. This approach validates the lumped element circuit analysis already discussed in 2.2.1. The sources of internal losses in the cavity can originate from the interactions of the cavity with its local environment, and are typically observed as low-frequency noise in the resonant frequency of the cavity [52, 92, 93]. Such damping due to internal losses will be neglected (i.e., $\kappa_{\text{int}} = 0$) initially in this model, to be added phenomenologically later.

To outline, we begin by writing down the cavity and transmission line wave equations, along with the capacitive coupling and shorted-end boundary conditions using Kirchhoff's laws. The general solutions to the corresponding quantum Heisenberg wave equations that are coupled via these boundary conditions are obtained using the operator scattering approach. Under the condition of weak coupling, the standard form input-output quantum Langevin equation for the cavity mode operator is recovered by approximation, together with explicit expressions for the resonant frequency and damping rate in terms of the circuit parameters.

Referring to Fig. 2.10, the wave equations for the cavity phase field $\phi_c(x,t)$ and the transmission line probe phase field $\phi_p(x,t)$ are

$$\frac{\partial^2 \phi_i}{\partial t^2} = \left(\mathcal{L}_i \mathcal{C}_i\right)^{-1} \frac{\partial^2 \phi_i}{\partial x^2}, \begin{cases} i = c, & \text{if } 0 < x < l \\ i = p, & \text{if } x < 0, \end{cases} \tag{2.49}$$

where the phase field is defined in terms of the magnetic flux field $\Phi(x,t)$ through $\phi_i \equiv 2\pi\Phi/\Phi_0$ with $\Phi_0 = h/(2e)$ the flux quantum, $\mathcal{L}_i$, $\mathcal{C}_i$ denote respectively the inductance and capacitance per unit length of the cavity ($i = c$) and transmission line ($i = p$), and l is the cavity center conductor length.

The current and voltage propagating along the transmission line can be expressed respectively in terms of the phase field as

$$V_i(x,t) = \left(\frac{\Phi_0}{2\pi}\right)\frac{\partial \phi_i}{\partial t} \qquad\qquad I_i(x,t) = \frac{1}{\mathcal{L}_i}\left(\frac{\Phi_0}{2\pi}\right)\frac{\partial \phi_i}{\partial x}, \tag{2.50}$$

such that we can retrieve the wave equation Eq. (2.1) for voltage and current by substitution of these two expressions into Eq. (2.49). Hence the current conservation at $x = 0$ and the boundary condition at $x = l$ give respectively:

$$\frac{1}{\mathcal{L}_p}\left.\frac{\partial \phi_p}{\partial x}\right|_{x=0^-} = \frac{1}{\mathcal{L}_c}\left.\frac{\partial \phi_c}{\partial x}\right|_{x=0^+} = C_{pc}\left.\left(\ddot{\phi}_c - \ddot{\phi}_p\right)\right|_{x=0}, \tag{2.51}$$

$$\phi_c(l,t) = 0. \tag{2.52}$$

Working with the Heisenberg equations resulting from formally replacing the coordinates with their associated quantum operators $\hat{\phi}_c(x,t)$ and $\hat{\phi}_p(x,t)$, the general solution for the wave equation (2.49) can be written in terms of photon creation/annihilation operators as follows:

$$\phi_i(x,t) = \frac{2\pi}{\Phi_0}\int_0^\infty d\omega \sqrt{\frac{\hbar Z_i}{\pi\omega}}\frac{1}{2}\left[e^{-i\omega(t-t_0-x/v_i)}a_i^{\rightarrow}(\omega,t_0) + e^{-i\omega(t-t_0+x/v_i)}a_i^{\leftarrow}(\omega,t_0)\right] + \text{h.c.}, \tag{2.53}$$

where ‘h.c.’ denotes the Hermitian conjugate and we have dropped the hats on the operators for notational convenience. Note that there should properly be a regularizing, upper frequency cut-off in Eq. (2.53) due to the finite length of the cavity and transmission line. However, the actual measured quantities involve finite frequency bandwidths about the pump frequency that are well below (and independent of) the cut-off. The superscripts ‘→’ (‘←’) correspond to right (left) propagating modes, with the photon creation/annihilation operators satisfying the standard commutation relation

$$[a_i^m(\omega,t_0), (a_i^n(\omega',t_0))^\dagger] = \delta_{mn}\delta(\omega-\omega'), \tag{2.54}$$

where $m,n \in \{`\rightarrow', `\leftarrow'\}$. The cavity and transmission line impedances are given by $Z_i = \sqrt{\mathcal{L}_i/\mathcal{C}_i}$ [note Z_i is the same as Z_0 used in §2.1 and §2.2], and $v_i = (\mathcal{L}_i\mathcal{C}_i)^{-1/2}$ is the microwave phase field propagation velocity. These commutation relations, together with the form of the solution (2.53) ensure that the phase field operators and their conjugate momenta satisfy the standard canonical commutation relations given in Eq. (2.39).

In essence, the operator scattering approach involves substituting the wave equation solutions (2.53) into the boundary conditions (2.51) and (2.52) in order to express the left propagating (i.e., "reflected" or "scattered") probe operator $a_p^{\leftarrow}$ in terms of the right propagating ("incident") probe operator $a_p^{\rightarrow}$ and cavity operator $a_c^{\rightarrow}$.

Starting with boundary condition (2.52), we have $a_c^{\leftarrow}(\omega, t_0) = -e^{2i\omega l/v_c} a_c^{\rightarrow}(\omega, t_0)$, so that the cavity phase field solution (2.53) (with $i = c$) becomes

$$\begin{aligned}\phi_c(x,t) = \frac{2\pi}{\Phi_0}\int_0^\infty d\omega \sqrt{\frac{\hbar Z_c}{\pi\omega}}\frac{1}{2}e^{-i\omega(t-t_0)} \quad \times& \quad \left[e^{i\omega x/v_c} - e^{-i\omega(x-2l)/v_c}\right] a_c^{\rightarrow}(\omega, t_0) \\ &+\text{h.c.}; \qquad (2.55)\end{aligned}$$

one may readily verify that solution (2.55) vanishes at $x = l$ as required by the boundary condition (2.52). Using Eq. (2.53) (for $i = p$), Eq. (2.55), and boundary condition (2.51), we can now couple the cavity and probe phase field to arrive at the following respective expressions for ϕ_p and $a_c^{\rightarrow}$:

$$\begin{aligned}\phi_p(x,t) = \frac{2\pi}{\Phi_0}\int_0^\infty d\omega \sqrt{\frac{\hbar Z_p}{\pi\omega}}\frac{1}{2}e^{-i\omega t} \times \left[e^{i\omega x/v_p} + \left(\frac{1 + i\omega Z_p C_{pc}}{1 - i\omega Z_p C_{pc}}\right) e^{-i\omega x/v_p}\right] a_p^{\text{in}}(\omega) \\ -i\frac{2\pi}{\Phi_0}\int_0^\infty d\omega \sqrt{\frac{\hbar Z_p}{\pi\omega}}\frac{1}{2}e^{-i\omega(t-t_0+x/v_p)}\left(1 - e^{2i\omega l/v_c}\right) \\ \times \frac{\omega\sqrt{Z_p Z_c} C_{pc}}{1 - i\omega Z_p C_{pc}} a_c^{\rightarrow}(\omega, t_0) + \text{h.c.} \\ (2.56)\end{aligned}$$

and

$$\begin{aligned}&\left[\cos\left(\omega l/v_c\right) - \frac{\omega Z_c C_{pc}}{1 + \left(\omega Z_p C_{pc}\right)^2}\sin\left(\omega l/v_c\right) - i\frac{\left(\omega\sqrt{Z_c Z_p} C_{pc}\right)^2}{1 + \left(\omega Z_p C_{pc}\right)^2}\sin\left(\omega l/v_c\right)\right] a_c^{\rightarrow}(\omega, t_0) \\ &= -ie^{-i\omega(t_0 + l/v_c)}\frac{\omega\sqrt{Z_p Z_c} C_{pc}}{1 - i\omega Z_p C_{pc}} a_p^{\text{in}}(\omega), \qquad (2.57)\end{aligned}$$

where $a_p^{\text{in}}(\omega) \equiv e^{i\omega t_0} a_p^{\rightarrow}(\omega, t_0)$ may be interpreted classically as the right propagating component of the pump/probe line field in frequency space that enters the cavity at time $t = 0$.

Under the condition of weak cavity-probe coupling, Eq. (2.57) describes the Fourier transform of the quantum dynamics of approximately independent harmonic oscillators (i.e., cavity modes) subject to damping and noise. The resonant mode frequencies are obtained by setting the real, square-bracketed coefficient in the first line to zero and solving for ω, while the mode linewidths are given by the imaginary coefficient on the second line of Eq. (2.57). The term involving $a_p^{\mathrm{in}}(\omega)$ represents the pump drive and noise. In particular, imposing the condition of weak coupling given by the smallness of the dimensionless parameter $\zeta \equiv C_{pc}/(\mathcal{C}_c l) \ll 1$, and expanding to first order in ζ, we obtain for the mode frequencies

$$\omega_n \approx (2n+1)\,\frac{\pi v_c}{2l}\left(1-\frac{C_{pc}}{\mathcal{C}_c l}\right),\ n=0,1,2,\ldots, \tag{2.58}$$

which coincides with the lumped element expression (2.15) for the cavity mode capacitance: $C = \mathcal{C}_c l/2$. Furthermore, under the Markovian approximation, the pump/probe damping rate κ_{ext} is given by

$$\kappa_{\mathrm{ext}} = 2Z_p\frac{C_{pc}^2}{\mathcal{C}_c l}\omega_n^2, \tag{2.59}$$

which matches Eq. (2.7) near ω_n with the external quality factor $Q_{\mathrm{ext}} \equiv \omega_n/\kappa_{\mathrm{ext}}$.

2.3.3. Validity of Scattering Approach

We can now use results obtained in 2.3.2 to derive the standard quantum Langevin equation in the Fourier domain involving the familiar closed-system cavity mode Hamiltonian, along with the zero-point fluctuations of the cavity phase coordinate modes.

Simplifying Eq. (2.57) by approximation using (2.58) and restricting to a narrow bandwidth $\Delta\omega \ll \omega_n$, we obtain to first order in the capacitance ratio $\zeta \equiv C_{pc}/(\mathcal{C}_c l) \ll 1$:

$$\left(\omega-\omega_n+i\frac{\kappa_{\mathrm{ext}}}{2}\right)a_n(\omega) = \sqrt{\kappa_{\mathrm{ext}}}\;a_p^{\mathrm{in}}(\omega). \tag{2.60}$$

This expression is the standard, Fourier transformed quantum Langevin equation, where the nth cavity mode photon annihilation operator is defined as

$$a_n(\omega) \equiv \sqrt{\frac{2l}{v_c}}e^{i\omega t_0}a_c^{\rightarrow}(\omega,t_0), \tag{2.61}$$

for ω in the vicinity of a given mode frequency ω_n [Eq. 2.58)]. This rescaling ensures that $a_n(t) = \frac{1}{\sqrt{2\pi}}\int_{-\infty}^{+\infty} d\omega e^{-i\omega t}a_n(\omega)$ satisfies the usual, discrete mode canonical commutation relation $[a_n(t), a_n^{\dagger}(t)] = 1$.

Thus the solution of $\phi_c(x,t)$ in Eq. (2.55) is reduced to a sum containing n

discrete modes $\phi_n(x,t)$ with a bandwidth of $\Delta\omega$. Applying the second derivative with respect to time to the solution of each of these modes we get the equation of motion corresponding to the nth mode

$$\ddot{\phi}_n(x,t) = -\omega_n^2 \phi_n(x,t). \tag{2.62}$$

We can thus extract the Lagrangian of the closed system as

$$\mathscr{L} = \left(\frac{\Phi_0}{2\pi}\right)^2 \sum_n^{\infty} \left(\frac{1}{2} C_n \dot{\phi}_n^2 - \frac{\phi_n^2}{2L_n}\right), \tag{2.63}$$

with the lumped element parameters given by the mode capacitance $C_n = \mathcal{C}_c l/2 + C_{pc}$ and the mode inductance $L_n = 8\mathcal{L}_c l/(2n+1)^2\pi^2$. Defining the conjugate momentum $p_{n,\phi} \equiv \partial\mathscr{L}/\partial\dot{\phi}_n$, the Hamiltonian of the closed system consisting of a shorted quarter-wave resonator with a coupling capacitance can be extracted using $H_{\text{cav}} = \Sigma_n p_{n,\phi}\dot{\phi}_n - \mathscr{L}$:

$$\begin{aligned} H_{\text{cav}} &= \sum_{n=0}^{\infty} \left[\left(\frac{2\pi}{\Phi_0}\right)^2 \frac{p_{n,\phi}^2}{2C_n} + \left(\frac{\Phi_0}{2\pi}\right)^2 \sum_{n=0}^{\infty} \frac{\phi_n^2}{2L_n} \right] \\ &= \sum_{n=0}^{\infty} \hbar\omega_n \left(a_n^\dagger a_n + \frac{1}{2}\right), \end{aligned} \tag{2.64}$$

and thus comprises of n discrete harmonic oscillator modes. The first term represents the Hamiltonian for the independent lumped element LC oscillator expressed in terms of the generalized mode phase coordinates and conjugate momenta respectively, and we identify the conjugate momenta as the charge stored in the mode capacitance: $p_{n,\phi} = (\Phi_0/2\pi)Q_n$ in Eq. (2.38). In terms of the creation/annihilation operators a_n for the mode 'n' cavity operator obtained from $\phi_n = \phi_{zp,n}\left(a_n + a_n^\dagger\right)$ and $p_n = -i\left(\Phi_0/2\pi\right)^2 \omega_n \phi_{zp,n}\left(a_n - a_n^\dagger\right)$, we get the familiar form of harmonic oscillator Hamiltonian, as given in 2.41. The mode zero-point uncertainty can be written as

$$\phi_{zp,n} = \left(\frac{2\pi}{\Phi_0}\right)\sqrt{\frac{\hbar}{2C_n\omega_n}} = 2\sqrt{\frac{\mathcal{Z}_n}{R_K}}, \tag{2.65}$$

with $\mathcal{Z}_n = \pi\sqrt{L_n/C_n}$ the cavity mode impedance and $R_K = h/e^2$ the von Klitzing constant.

Finally, the output phase field is

$$\phi_p^{\text{out}}(x,t) = \frac{2\pi}{\Phi_0}\int_0^\infty d\omega\sqrt{\frac{\hbar Z_p}{4\pi\omega}}\, e^{-i\omega(t+x/v_p)}a_p^{\text{out}}(\omega), \tag{2.66}$$

following a similar convention as for $a_p^{\text{in}}(\omega)$ given above [just after Eq. (2.57)], and defining $a_p^{\text{out}}(\omega) \equiv e^{i\omega t_0}a_p^{\leftarrow}(\omega, t_0)$. Within the bandwidth $\Delta\omega$ and to first order in the capacitance ratio $\zeta = C_{pc}/(\mathcal{C}_c l)$, we can deduce $a_p^{\text{out}}(\omega)$ by identifying the left propagating (i.e., reflected) terms involving the exponential factor $e^{-i\omega(t-t_0+x/v_p)}$ in the coupled cavity-probe relation (2.56). In short, we have

$$a_p^{\text{out}}(\omega) = a_p^{\text{in}}(\omega) - i\sqrt{\kappa_{\text{ext}}}a_n(\omega), \tag{2.67}$$

the standard input-output relation for the cavity in a reflection mode measurement, where we have used the explicit expression (2.59) for the pump/probe damping rate κ_{ext}, and where the cavity mode annihilation operator is defined by Eq. (2.61).

Section 2.4

Output Power Measurement[2]

Experiments on the device performance require measurements on the steady state response of the cavity, subject to a pump with frequency ω_p typically applied in the vicinity of the fundamental cavity resonance ω_0 given by Eq. (2.58) for $n = 0$. In practice, this involves a classical input pump signal at room temperature, which is further attenuated at different stages to reach the sample placed at the cryogenic temperature ($\lesssim$ 30 mK), for which the scale of thermal fluctuations $k_BT \ll \hbar\omega_0$. In the absence of driving, we consider the continuum of modes in the semi-infinite transmission line to be in a thermal state given by

$$\rho_{\text{th}} = \frac{1}{Z}\sum_{\{n(\omega)\}=0}^{\infty} e^{-\beta H_p}\ |\{n(\omega)\}\rangle_p\langle\{n(\omega)\}|_p \tag{2.68}$$

where $|\{n(\omega)\}\rangle_p$ is the transmission line Fock state, $Z = \text{Tr}\left(e^{-\beta H_p}\right)$ is the partition function, $\beta \equiv 1/(k_BT)$, and the transmission line Hamiltonian takes the form in Eq.

---

[2] We acknowledge that the bulk of this section is reproduced from a Journal of Applied Physics publication by Kanhirathingal *et. al.* [13], with major contributions from Prof. Blencowe.

(2.42):

$$H_p = \hbar \int_0^\infty d\omega\omega \left(a_p^{\mathrm{in}}(\omega)\right)^\dagger a_p^{\mathrm{in}}(\omega), \tag{2.69}$$

where we neglect the zero point energy term since it does not contribute to the measured quantities.

The presence of coherent driving may be approximated by a displaced thermal state for the pump/probe transmission line: $\rho_{\alpha,\mathrm{th}} = D[\alpha]\rho_{\mathrm{th}}D[\alpha]^\dagger$ [94], where $D[\alpha]$ is the displacement operator that gives the coherent state $|\alpha\rangle$ via operation on the vacuum state $|0\rangle$:

$$D[\alpha]\left|0\right\rangle = \left|\alpha\right\rangle, \tag{2.70}$$

and is defined as follows:

$$D[\alpha] = \exp\left(\int d\omega \left[\alpha(\omega)\left(a_p^{\mathrm{in}}(\omega)\right)^\dagger - \alpha^*(\omega)a_p^{\mathrm{in}}(\omega)\right]\right), \tag{2.71}$$

with

$$\alpha(\omega) = \sqrt{\frac{P_p^{\mathrm{in}}T_p^2}{\hbar}}\frac{e^{-(\omega-\omega_p)^2T_p^2/2}}{\sqrt{\omega}}e^{i\theta_p}. \tag{2.72}$$

Here, P_p^{in} is the average pump power and θ_p is the pump phase. The pump coherence time T_p is assumed to be longer than all other characteristic timescales of the system so that the displacement wavelet is narrowly smeared about $\omega = \omega_p$ in this large T_p limit.

Some general properties of $D[\alpha]$ is given by

$$\begin{aligned} D[\alpha]^\dagger D[\alpha] &= \mathbb{I} \\ D[\alpha]\hat{a}D[\alpha]^\dagger &= \hat{a} - \alpha \\ D[\alpha]^\dagger\hat{a}^\dagger D[\alpha] &= \hat{a}^\dagger + \alpha^*. \end{aligned} \tag{2.73}$$

We can then extract the time averaged output power (averaged over some measurement time T_M) in the bandwidth $\Delta\omega$ centered at ω_p using

$$P_p^{\mathrm{out}}(\omega_p, \Delta\omega) = \overline{\left\langle\left[I_p^{\mathrm{out}}(x,t|\omega_p,\Delta\omega)\right]^2\right\rangle}Z_p, \tag{2.74}$$

where the output probe current is

$$I_p^{\mathrm{out}}(x,t) = -\frac{\Phi_0}{2\pi\mathcal{L}_p}\frac{\partial\phi_p^{\mathrm{out}}(x,t)}{\partial x}. \tag{2.75}$$

Substituting the quantum Langevin equation (2.60) into the input-output relation (2.67) and using the definition (2.74) for P_p^{out}, we obtain

$$\begin{aligned} P_p^{\text{out}}(\omega_p, \Delta\omega) = \frac{\hbar\omega_p}{4\pi} \int\int_{\omega_p-\Delta\omega/2}^{\omega_p+\Delta\omega/2} d\omega d\omega' \left(\frac{2\sin[(\omega-\omega')T_M/2]}{(\omega-\omega')T_M}\right) \\ \left[r(\omega)r^*(\omega')\, \langle a_p^{\text{in}}(\omega)\left(a_p^{\text{in}}(\omega')\right)^\dagger\rangle + r(\omega')r^*(\omega)\, \langle\left(a_p^{\text{in}}(\omega)\right)^\dagger a_p^{\text{in}}(\omega')\rangle\right], \end{aligned} \tag{2.76}$$

where the cavity reflection coefficient $r(\omega)$ is defined as

$$r(\omega) = \frac{\omega - \omega_n - i\kappa_{\text{ext}}/2}{\omega - \omega_n + i\kappa_{\text{ext}}/2}, \tag{2.77}$$

as expected [Refer to Eq. (2.48)]. Using the properties in Eq. (2.73), the ensemble averages in the above expression are given by

$$\begin{aligned} \langle\left(a_p^{\text{in}}(\omega)\right)^\dagger a_p^{\text{in}}(\omega')\rangle &= \text{Tr}[\rho_{\alpha,\text{th}}\left(a_p^{\text{in}}(\omega)\right)^\dagger a_p^{\text{in}}(\omega')] = n_p(\omega)\delta(\omega-\omega') + \alpha^*(\omega)\alpha(\omega') \\ \langle a_p^{\text{in}}(\omega)\left(a_p^{\text{in}}(\omega')\right)^\dagger\rangle &= \text{Tr}[\rho_{\alpha,\text{th}}\left(a_p^{\text{in}}(\omega)\right)^\dagger a_p^{\text{in}}(\omega')] = \left(n_p(\omega)+1\right)\delta(\omega-\omega') + \alpha^*(\omega)\alpha(\omega'). \end{aligned} \tag{2.78}$$

with the transmission line average thermal occupancy $n_p(\omega) = (e^{\beta\hbar\omega} - 1)^{-1}$ (which is small in the frequency bandwidth of interest at $T \lesssim 30$ mK). Inserting the above expressions back into Eq. (2.76) and using $\omega_p = \omega_0$ and $\Delta\omega \ll \omega_0$, we get

$$P_p^{\text{out}}(\omega_p, \Delta\omega) = P_p^{\text{in}} + \frac{\hbar\omega_p}{2\pi} \int_{\omega_p-\Delta\omega/2}^{\omega_p+\Delta\omega/2} d\omega \left(n_p(\omega) + \frac{1}{2}\right), \tag{2.79}$$

Since we set $\kappa_{\text{int}} = 0$, the pump microwaves are reflected without any absorption/emission as expected.

Internal noise/losses are modeled as a second, internal thermal bath denoted as ρ_ι, modifying the total input state: $\rho_{\text{in}} = \rho_{\alpha,p} \otimes \rho_\iota$. The thermal occupancies of the pump n_p and internal bath n_ι are usually assumed to be identical, as the temperature variations at different locations in the device are neglected. However, in reality, the internal bath may have a different noise temperature due, for example, to coupling with two-level defects [95]. In the presence of internal losses, the output power can be obtained as

$$P_p^{\text{out}}(\omega_0, \Delta\omega) = P_p^{\text{in}} + \frac{\hbar\omega_0}{2\pi} \int_{\omega_0 - \Delta\omega/2}^{\omega_0 + \Delta\omega/2} d\omega \tag{2.80}$$

$$\left[n_p(\omega) + \frac{1}{2} + \frac{\kappa_{\text{ext}}\kappa_{\text{int}} \left(n_\iota(\omega) - n_p(\omega) \right)}{(\omega - \omega_p)^2 + \left(\frac{\kappa_{\text{tot}}}{2} \right)^2} \right], \tag{2.81}$$

with the second bath average thermal occupancy $n_\iota(\omega) = (e^{\beta_\iota \hbar\omega} - 1)^{-1}$ (for a bosonic bath) determined by the internal bath temperature $\beta_\iota = 1/k_B T_\iota$.

Chapter 3

The Cavity-embedded Cooper Pair Transistor

The cavity-embedded Cooper pair transistor (cCPT) consists of a shorted quarter-wave ($\lambda/4$) resonator in a co-planar wave guide geometry (the dynamics of which are discussed in Chapter 2), and a Cooper pair transistor (CPT) at the voltage anti-node (Fig 3.3). In this chapter, we will present a discussion of the open system dynamics of the cCPT and establish the inherent non-linearity of this device. We will begin with a brief review of the Josephson junctions, the component that makes the cCPT a non-linear harmonic oscillator. We will then proceed towards describing a theoretical framework for the cCPT. Since the CPT is designed to weakly interact with the cavity, its influence on the latter can be treated perturbatively within the operator scattering approach described in §2.3.2. This work thus serves as a prelude to further investigations into utilising the inherent non-linearity of the cCPT for applications in single-photon optomechanics, quantum measurements and low-frequency noise studies. The in-depth analysis will also validate the various assumptions and bias regimes used in the experimental characterization of the cCPT following this model [14].

Section 3.1

Josephson Junctions

In this section, we will look at the physics of the superconducting tunnel junction that embodies Josephson junctions. These concepts are well-studied since 1962 [96] as they form the basis of many interesting superconducting circuits and qubit architectures.

Hence this section only provides a brief, mostly qualitative review of the Josephson junction dynamics. For a detailed background reading, refer to Joyez's thesis [75] and textbooks by Grabert and Devoret [74], and Tinkham [97].

3.1.1. Single Superconducting Tunnel Junction

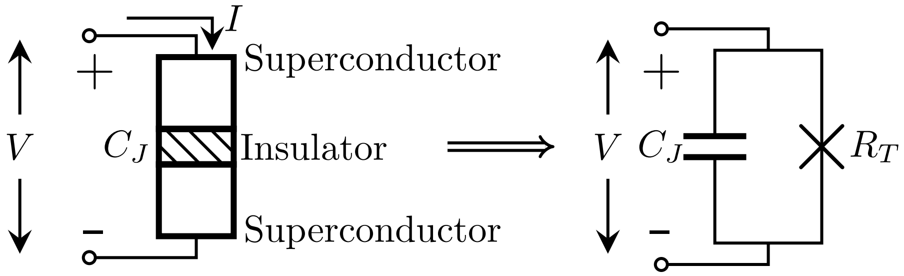

Figure 3.1: A single JJ consist of a thin insulator sandwiched between two superconducting electrodes. On the right, the equivalent lumped-element model is given.

A Josephson tunnel junction (JJ) consists of two superconducting electrodes (forming a source and drain) separated by a thin insulating barrier, which forms a junction capacitance C_J (Refer to Fig. 3.1). The charge transport occurs between the electrodes via Cooper pair tunneling. The facilitating condition for the tunneling of a single Cooper pair across the barrier is determined by the electrostatic energy, such that

$$\Delta E = \frac{Q^2}{2C_J} - \frac{(Q-2e)^2}{2C_J} > 0, \tag{3.1}$$

where $Q = N \times 2e$ is the charge on the junction capacitance, with N the number of Cooper pairs that have hopped across the junction.

Solving the Schrödinger equation in terms of the Cooper pair wave functions in the two superconducting electrodes, we can arrive at the expressions for current and voltage at the Josephson junctions:

$$I = I_C \sin(\varphi) \tag{3.2}$$

$$V = \frac{\Phi_0}{2\pi}\frac{\delta\varphi}{\delta t}, \tag{3.3}$$

where I_C is the critical current of the junction, and $\Phi_0 = h/2e$ is the magnetic flux quantum, as described in §2.3.2. Combining the above expressions using the flux relation $\Phi = L(\varphi)I(\varphi)$ [note $\Phi = (\Phi_0/2\pi)\varphi$], we can associate an inductance $L(\varphi)$

with the junction. The expression for $L(\varphi)$ is obtained as

$$L(\varphi) = \frac{L_J}{\cos\varphi}, \tag{3.4}$$

with $L_J \equiv (\Phi_0/2\pi)I_C$ the Josephson inductance of the junction. The nonlinear component originating from the JJs is evident from the above expression for inductance. Similarly, the energy change associated with a tunneling process can be obtained from $E_{\text{tun}}(\varphi) = \int IV dt$, and is obtained as

$$E_{\text{tun}}(\varphi) = -E_J \cos\varphi, \tag{3.5}$$

where we define another characteristic parameter of the junction, the Josephson energy, as

$$E_J \equiv \Phi_0 I_C/2\pi. \tag{3.6}$$

The total Hamiltonian of the JJ exposed to an environment that controls the electrostatic energy of the junction will thus contain two components: 1) the environmental contribution to the Hamiltonian corresponding to an energy of $\hat{Q}^2/2C_J$, where $\hat{Q} = \hat{N} \times 2e$ corresponding to the total charge, and 2) the tunneling energy described in Eq. (3.5) that leads to Cooper pair hopping between the electrodes. In short,

$$H_{\text{JJ}} = 4E_C\, \hat{N}^2 - E_J \cos\hat{\varphi}, \tag{3.7}$$

with E_C defined as the charging energy $E_C = e^2/2C_J$, the electrostatic energy associated with one electron. Analogous to the charge-flux conjugate variables described in §2.3.2 using Eq. (2.39), we identify the two conjugate variables of the JJ as the non-dimensional quantities $\hat{N} = \hat{Q}/2e$ and $\hat{\varphi} = (2\pi/\Phi_0)\Phi$ that are related via the commutation relation

$$[\hat{\varphi}, \hat{N}] = i. \tag{3.8}$$

Considering the sinusoidal nature of the Hamiltonian in Eq. (3.7), we further write down the more suitable phase coordinate form $e^{i\hat{\varphi}}$, and the commutation relation is expressed as follows:

$$\left[e^{i\hat{\varphi}}, \hat{N}\right] = -e^{i\hat{\varphi}}. \tag{3.9}$$

The usefulness of the phase coordinate $e^{i\hat{\varphi}}$ can be best observed using the action of the above commutator on the number state $|N\rangle$:

$$\begin{aligned}
\left[e^{i\hat{\varphi}}, \hat{N}\right]|N\rangle &= -e^{i\varphi}|N\rangle \\
\left(Ne^{i\hat{\varphi}} - \hat{N}e^{i\hat{\varphi}}\right)|N\rangle &= -e^{i\varphi}|N\rangle \\
\hat{N}\left(e^{i\hat{\varphi}}|N\rangle\right) &= (N+1)\left(e^{i\hat{\varphi}}|N\rangle\right). \qquad (3.10)
\end{aligned}$$

Thus $e^{i\hat{\varphi}}$ raises the number state by one Cooper pair, and $e^{-i\hat{\varphi}}$ lowers the number state by one, resulting in:

$$e^{i\hat{\varphi}}|N\rangle = |N+1\rangle \qquad\qquad e^{-i\hat{\varphi}}|N\rangle = |N-1\rangle. \qquad (3.11)$$

Applying the above relations to the Hamiltonian Eq. (3.7), we may rewrite the Hamiltonian of the JJ in the number basis as

$$H_{\mathrm{JJ}} = 4E_C \sum_{N=-\infty}^{+\infty} N^2|N\rangle\langle N| - \frac{E_J}{2}\sum_{N=-\infty}^{+\infty}\left(|N+1\rangle\langle N| + |N-1\rangle\langle N|\right). \qquad (3.12)$$

Thus the eigenstates of the system characterized by the Hamiltonian in Eq. (3.7) maybe considered as a coherent superposition of an infinite number of number states $|N\rangle$.

For completeness, we also mention the two crucial conditions that allow a JJ to be operated in this interesting regime, as follows. Firstly, the charging energy $E_C \gg k_BT$, such that the junction behaviour can be accessed reliably using an external environment and is not exposed to thermal fluctuations. Secondly, the tunneling resistance $R_T \gg R_K/4$, where $R_K = h/e^2$ is the resistance quantum, also known as the von Klitzing constant (already defined in §2.3.2). This ensures that the energy uncertainty associated with the tunneling process is much smaller compared to the charging energy of one Cooper pair. As a result, the lifetime due to tunneling given by R_TC_J is high enough to create a localized wave function that guarantees charging effects in the junction.

3.1.2. Double Superconducting Tunnel Junctions

We will now focus our attention on the environmental variable discussed in 3.1.1, that allows the control of electrostatic energy of JJ systems. One neat and clever way to accomplish this is to introduce two JJs in series, that forms an island in between the

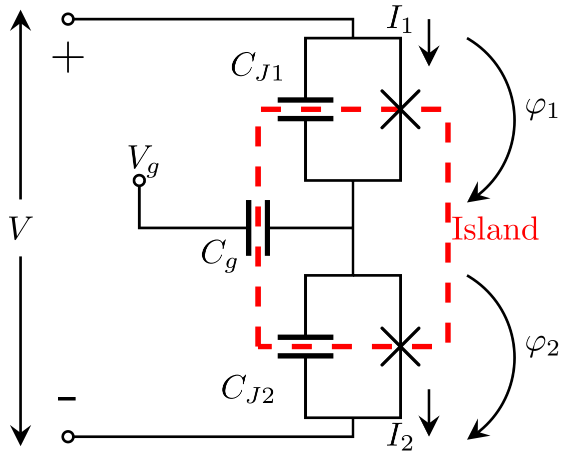

Figure 3.2: Two JJs in series forming an island that can be gate controlled via V_g.

junctions. The island can then be controlled using a gate voltage V_g through another capacitor C_g (Refer Fig. 3.2).

The combined system now has two degrees of freedom defined by the phase coordinates $\hat{\varphi}_1$ and $\hat{\varphi}_2$, with corresponding conjugate variables defined by $\hat{N}_1$ and $\hat{N}_2$. A better coordinate system to use is the average phase coordinate $\hat{\bar{\varphi}} \equiv (\hat{\varphi}_1 + \hat{\varphi}_2)/2$ and the corresponding half-difference coordinate $\widehat{\delta\varphi} \equiv (\hat{\varphi}_1 - \hat{\varphi}_2)/2$. We recognize the corresponding conjugate variables $\hat{N}_{\text{tot}}$ and $\hat{N}$ by applying the individual commutation relation in Eq. (3.8), resulting in

$$[\hat{\bar{\varphi}}, \hat{N}_{\text{tot}}] = [\widehat{\delta\varphi}, \hat{N}] = i, \tag{3.13}$$

where $\hat{N}_{\text{tot}} \equiv \hat{N}_1 + \hat{N}_2$ is twice the average number of Cooper pairs having crossed both the junctions, and $\hat{N} \equiv \hat{N}_1 - \hat{N}_2$ is the excess number of Cooper pairs on the island.

The tunneling of a Cooper pair in or out of the island is facilitated only when the electrostatic energy condition is met. The required energy cost is tunable via the gate voltage V_g and has a periodicity of 2e.

We will use a qualitative argument to arrive at the Hamiltonian of this configuration, in the limit of symmetric junctions, i.e., $C_{J1} = C_{J2} = C_J$, $E_{J1} = E_{J2} = E_J$ and $C_g \ll C_J$. As discussed in 3.1.1, the Hamiltonian will consist of the tunneling energy component as well as the contribution from the environment. The tunneling energy is that of the total of each junction given by

$$\begin{aligned} H_{\text{tun}} &= -E_J \cos\hat{\varphi}_1 - E_J \cos\hat{\varphi}_2 \\ &= -2E_J \cos\hat{\bar{\varphi}} \cos\hat{\delta\varphi}. \end{aligned} \tag{3.14}$$

The environmental component is determined by the electrostatic energy of the island corresponding to the number of Cooper pairs in the island N_{isl}, and the capacitance of the island C_Σ. Using charge conservation we determine the charge on the island as $Q_{\text{isl}} = 2e \times N_{\text{isl}} = 2e \times (N_1 - N_2 - n_g/2)$, where $n_g \equiv C_g V_g/e$ is twice the number of Cooper pairs associated with the current through the gate capacitor branch. Furthermore, the island sees the three capacitors in parallel resulting in $C_\Sigma = 2C_J + C_g$. Thus the electrostatic energy of the environment is

$$H_{\text{env}} = \frac{\left(2e(\hat{N} - n_g)\right)^2}{2C_\Sigma}. \tag{3.15}$$

We therefore arrive at the total Hamiltonian in the charge basis to be

$$\begin{aligned} H_{2\text{JJ}} = 4E_C &\sum_{N=-\infty}^{+\infty} \left(N - \frac{n_g}{2}\right)^2 |N\rangle\langle N| \\ &- E_J \cos\bar{\varphi} \sum_{N=-\infty}^{+\infty} \left(|N+1\rangle\langle N| + |N-1\rangle\langle N|\right), \end{aligned} \tag{3.16}$$

with the charging energy $E_c \equiv e^2/2C_\Sigma$.

Similar to the single junction configuration discussed in 3.1.1, the eigenstate of the combined system will have a coherent superposition of an infinite number of number states $|N\rangle$ but this time tunable by the external parameter of gate voltage V_g. As we will see in subsequent sections, we are especially interested in the regime of $E_C > E_J$, such that the transition between each number state is reduced. This allows us to operate in a regime where the system is sensitive to minute gate charge fluctuations.

It is also worth noting that several variations of double Josephson junctions involving varying operating regimes determined by E_J and E_C have been looked at theoretically, and realized experimentally with state-of-the-art applications. Perhaps the most famous cousin to the above-mentioned system is the transmon qubit, which is formed by two JJs in parallel and a shunted capacitance, and fabricated in the $E_C < E_J$ regime [60]. Configured this way, the anharmonicity in the system can be exploited to model the system as a qubit where low-frequency charge noise is also exponentially suppressed due to the smallness of E_C. Some other notable variations that include JJ-cQED interactions are charge qubits, flux qubits, phase qubits, quantronium, and fluxonium [76].

Section 3.2

cCPT-Transmission Line Dynamics[1]

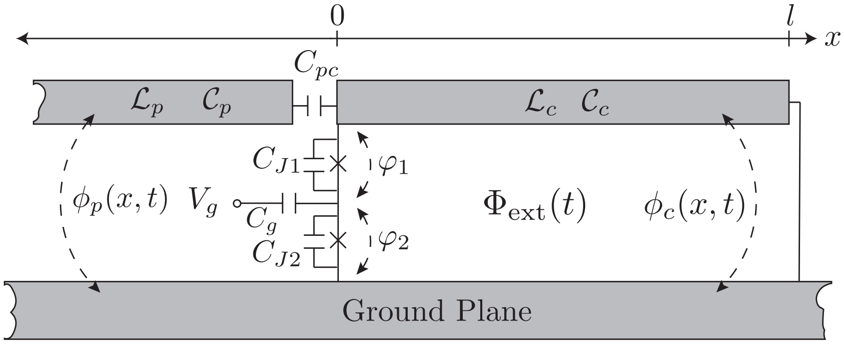

Figure 3.3: Circuit schematic of the cCPT coupled to a pump/probe transmission line via a coupling capacitor C_{pc}.

We have now setup the physics of the two crucial components of the cCPT, namely the shorted quarter-wave microwave resonator (refer to §2.3.2) and the JJs (refer to §3.1). In this section, we move on to describing a bipartite system formed by these two components - the cCPT. As already mentioned, the cCPT consists of a $\lambda/4$-wave resonator in a co-planar wave guide geometry and a CPT at its voltage anti-node. We will present a first-principles derivation of the cCPT dynamics that compares to actual devices to good approximation by allowing asymmetry in the JJs, given by distinct junction capacitances C_{J1} and C_{J2}, and critical currents I_{C1} and I_{C2} (refer to Fig. 3.3).

We begin by following the same procedure as in §2.3.2; in particular, we write down the cCPT-transmission line boundary conditions, which now accommodate the current through the CPT at $x = 0$ (Fig. 3.3). This leads to two additional phase degrees of freedom, one for each of the two JJs making up the CPT. The CPT-cavity

---

[1] We acknowledge that the bulk of this section is reproduced from a Journal of Applied Physics publication by Kanhirathingal *et. al.* [13], with major contributions from Prof. Blencowe.

coupling accomplished through the flux biased SQUID loop reduces the number of independent phase coordinates from three down to two. We then proceed to write down the CPT Hamiltonian, and further use adiabatic elimination of the CPT dynamics to expand the resulting cavity effective potential about a stable minimum. The resulting anharmonic contributions from the CPT are highly tunable and very strong; their effects can be observed even close to the few-photon limit [14].

3.2.1. Formulation of the Circuit Equations

Referring to Fig. 3.3, the cCPT consists of two JJs in series located at the voltage anti-node of the cavity, with the electrostatic energy of the CPT island tuned via a gate voltage V_g. The relevant coordinates for the cCPT system are the cavity phase field $\phi_c(x,t)$ and the JJ phase coordinates $\varphi_{1(2)}$. Note that Eqs. (2.49), (2.52) and (2.53) remain the same, while the boundary condition (2.51) at $x = 0^+$ gets modified to

$$\begin{aligned}
-\frac{\Phi_0}{2\pi\mathcal{L}_p}\,\phi_p'(x,t)\big|_{x=0^-} =& C_{pc}\left(\ddot{\phi}_c - \ddot{\phi}_p\right)\Big|_{x=0} \\
=& -\frac{\Phi_0}{2\pi\mathcal{L}_c}\,\phi_c'(x,t)\big|_{x=0^+} + \frac{\Phi_0}{2\pi}C_{J1}\ddot{\varphi}_1 + I_{C1}\sin\varphi_1 \\
=& -\frac{\Phi_0}{2\pi\mathcal{L}_c}\,\phi_c'(x,t)\big|_{x=0^+} + \frac{\Phi_0}{2\pi}\left(C_{J2}+C_g\right)\ddot{\varphi}_2 + I_{C2}\sin\varphi_2 \\
& - C_g\dot{V}_g(t),
\end{aligned} \tag{3.17}$$

where $f'(x,t)$ and $\dot{f}(x,t)$ represent the spatial and temporal derivatives, respectively, and recall $\Phi_0 = h/2e$ is the flux quantum.

The associated SQUID loop constrains the phase coordinates through the relation

$$\varphi_1(t) + \varphi_2(t) - \phi_c(0,t) \approx 2\pi n + 2\pi\frac{\Phi_{\text{ext}}(t)}{\Phi_0}, \tag{3.18}$$

where $\Phi_{\text{ext}}(t)$ is the externally applied flux bias, n is an arbitrary integer (set to zero without loss of generality). For our cCPT device [14, 82], the magnitude of the supercurrent I_{cir} circulating through the cCPT loop is such that we can neglect the resulting induced flux, i.e., $(\mathcal{L}_c l)I_{\text{cir}} \ll \Phi_0$.

Equation (3.18) allows us to reduce the number of system coordinates by one, since the average CPT coordinate $\bar{\varphi} = (\varphi_1 + \varphi_2)/2$ determines the cavity phase $\phi_c(x,t)$; we will utilize the cavity coordinate $\phi_c(x,t)$ and the half-difference CPT coordinate

$\delta\varphi = (\varphi_1 - \varphi_2)/2$ as the primary, independent variables. The equation of motion for $\delta\varphi$ can be obtained using the modified Eq. (3.17) together with Eqs. (2.53) (for $i = p$) and Eq. (2.55). As we are primarily interested in deriving the charge sensitivity of the device in this thesis, we only allow a time dependent gate voltage modulation and neglect any time dependent magnetic flux modulation. We obtain:

$$\frac{\Phi_0 C_{\mathrm{CPT}} C_\Sigma}{\pi} \ddot{\delta\varphi} = \ (C_g + \Delta C_J) C_{pc} \frac{\partial \hat{V}_p^{\mathrm{in}}(0,t)}{\partial t} - (\text{cCPT terms}), \tag{3.19}$$

where the junction capacitance asymmetry $\Delta C_J = C_{J2} - C_{J1}$, the CPT capacitance $C_{\mathrm{CPT}} = C_{J1}(C_{J2} + C_g)/C_\Sigma$ and the total island capacitance $C_\Sigma = C_{J1} + C_{J2} + C_g$.

The 'cCPT terms' contribution in Eq. (3.19) is given by

$$\begin{aligned}[] & [I_{C1}(C_g + C_{J2}) - I_{C2} C_{J1}] \sin(\phi/2) \cos(\delta\varphi) \\ & \qquad + [I_{C1}(C_g + C_{J2}) + I_{C2} C_{J1}] \cos(\phi/2) \sin(\delta\varphi) + C_g C_{J1} \dot{V}_g, \end{aligned}$$

where we have introduced a displaced cavity phase $\phi(t)$ to absorb the external flux bias as follows:

$$\phi(t) = \phi_c(0,t) + 2\pi\Phi_{\mathrm{ext}}/\Phi_0. \tag{3.20}$$

The first term on the RHS of Eq. (3.19) represents the CPT's direct coupling to the pump/probe line:

$$\hat{V}_p^{\mathrm{in}}(0,t) = -i \int_0^\infty d\omega \sqrt{\frac{\hbar\omega Z_p}{\pi}} e^{-i\omega t} \times (1 - i\omega Z_p C_{pc})^{-1} a_p^{\mathrm{in}}(\omega) + \text{h.c}, \tag{3.21}$$

to be contrasted with the more familiar indirect CPT coupling to the probe line via the cavity. As we will see in the next steps, the former contribution appears as an unwanted gate modulation, which can however be neglected as long as $C_g \ll C_J$.

We may now similarly proceed as in Sec. 2.3.2 to employ the equation of motion for the cavity phase $\phi_c(x,t)$, and further determine the Lagrangian and Hamiltonian of the cCPT system. However, as this turns out to be a cumbersome task if no approximations are made, we will first focus on the half-difference CPT coordinate $\delta\varphi$, utilizing several valid approximations to simplify the analysis.

3.2.2. The Hamiltonian of the Cooper Pair Transistor

Instead of writing down the open cCPT Hamiltonian which contains contributions from the cavity, CPT, and the pump/probe transmission line, we use the equation of motion in Eq. (3.19) to first obtain the CPT contribution to the Lagrangian,

$$\begin{aligned}\mathscr{L}_{\mathrm{CPT}} \;=\;& \left(\frac{\Phi_0}{2\pi}\right)^2 \frac{2C_{J1}\left(C_{J2}+C_g\right)}{C_\Sigma}\dot{\delta\varphi}^2 \\ &+2\left(E_{J1}+\frac{C_{J1}}{C_\Sigma}\Delta E_J\right)\cos(\phi/2)\cos\left(\delta\varphi\right) \\ &-\frac{2\left[\left(C_g+\Delta C_J\right)E_{J1}-\Delta E_J C_{J1}\right]}{C_\Sigma}\sin(\phi/2)\sin\left(\delta\varphi\right) \\ &+\frac{\Phi_0 C_{J1}C_g}{\pi C_\Sigma}V_g\dot{\delta\varphi}-\frac{\Phi_0 C_{pc}(C_g+\Delta C_J)}{\pi C_\Sigma}\hat{V}_p^{\mathrm{in}}(0,t)\dot{\delta\varphi}. \qquad (3.22)\end{aligned}$$

The momentum conjugate to the half-difference CPT phase coordinate $p_{\delta\varphi}\equiv\partial\mathscr{L}/\partial\dot{\delta\varphi}$ can be derived from the above expression as

$$p_{\delta\varphi}=\left(\frac{\Phi_0}{4\pi}\right)^2\frac{2C_{J1}\left(C_{J2}+C_g\right)}{C_\Sigma}\dot{\delta\varphi}+\frac{\Phi_0}{\pi}\left(\frac{C_{J1}}{C_\Sigma}C_gV_g-\frac{\left(C_g+\Delta C_J\right)}{C_\Sigma}C_{pc}\hat{V}_p^{\mathrm{in}}(0,t)\right). \qquad (3.23)$$

Combining Eqs. (3.22) and (3.23) then yields the following CPT Hamiltonian using $H_{\mathrm{CPT}}=p_{\delta\varphi}\dot{\delta\varphi}-\mathscr{L}$:

$$\begin{aligned}H_{\mathrm{CPT}}=&\left(\frac{2\pi}{\Phi_0}\right)^2\frac{1}{8C_{\mathrm{CPT}}}\left(p_{\delta\varphi}-\frac{\Phi_0}{\pi}\left(\frac{C_{J1}}{C_\Sigma}C_gV_g-\hat{Q}_p^{\mathrm{in}}(0,t)\right)\right)^2 \\ &-2E_J\cos\left(\phi/2\right)\cos\left(\delta\varphi\right)+2\delta E_J\sin\left(\phi/2\right)\sin\left(\delta\varphi\right), \qquad (3.24)\end{aligned}$$

with $\hat{Q}_p^{\mathrm{in}}(0,t)\equiv\left(C_g+\Delta C_J\right)C_{pc}\hat{V}_p^{\mathrm{in}}(0,t)/C_\Sigma$, and the effective Josephson energy coefficients in the potential energy term defined as follows:

$$E_J=\left(E_{J1}+\frac{C_{J1}}{C_\Sigma}\Delta E_J\right) \qquad (3.25)$$

and

$$\delta E_J=\frac{\left[\left(C_g+C_{J2}\right)E_{J1}-E_{J2}C_{J1}\right]}{C_\Sigma}. \qquad (3.26)$$

Here, the Josephson energies of the junctions are defined as before, $E_{J1(2)}=I_{C1(2)}\Phi_0/2\pi$, and $\Delta E_J=E_{J2}-E_{J1}$.

To sum up, the corresponding quantized CPT operators obey the commutation relations $[\hat{\delta\varphi},\hat{N}]=i$, where $\hat{N}\equiv\hat{p}_{\delta\varphi}/\hbar$, as already discussed in 3.1.2. In the more suitable phase coordinate form with unit circle configuration space, the commutation relations take the form:

$$\left[e^{i\delta\hat{\varphi}}, \hat{N}\right] = -e^{i\delta\varphi}. \tag{3.27}$$

Equation (3.27) has a Hilbert space representation spanned by the eigenstates $|N\rangle$ of the operator $\hat{N}$:

$$\hat{N}|N\rangle = N|N\rangle,\ N = 0, \pm 1, \pm 2, \ldots \tag{3.28}$$

i.e., N takes discrete, integer values which can be interpreted as the number of excess Cooper pairs on the CPT island. Similarly, we can also define the gate polarization number n_g in single electron units as follows:

$$n_g \equiv \frac{2\Phi_0 C_{J1} C_g}{\hbar\pi C_\Sigma} V_g = \frac{2C_{J1}C_g}{eC_\Sigma} V_g. \tag{3.29}$$

The CPT Hamiltonian in the number basis then becomes

$$\begin{aligned} H_{\mathrm{CPT}} = 4E_C &\sum_{N=-\infty}^{+\infty} \left[N - \frac{1}{2}\left(n_g - \hat{N}_p^{\mathrm{in}}\right)\right]^2 |N\rangle\langle N| \\ &- E_J \cos(\phi/2) \sum_{N=-\infty}^{+\infty} \left(|N+1\rangle\langle N| + |N-1\rangle\langle N|\right) \\ &- i\delta E_J \sin(\phi/2) \sum_{N=-\infty}^{+\infty} \left(|N+1\rangle\langle N| - |N-1\rangle\langle N|\right), \end{aligned} \tag{3.30}$$

where ϕ is defined in Eq. (3.20), the charging energy $E_C = e^2/(8C_{\mathrm{CPT}})$, and the effective, polarization charge number noise operator is given by $\hat{N}_p^{\mathrm{in}}(t) = 2\hat{Q}_p^{\mathrm{in}}(0,t)/e$. Equation (3.30) reduces to the familiar form of the CPT Hamiltonian [refer to Eq.(3.16)] in the limiting case of junction symmetry $\Delta E_J = \Delta C_J = 0$ and $C_g \ll C_J$ (with $C_J \equiv C_{J1} = C_{J2}$) [75]:

$$\begin{aligned} H_{\mathrm{CPT}} = 4E_c &\sum_{N=-\infty}^{+\infty} \left(N - \frac{n_g}{2}\right)^2 |N\rangle\langle N| \\ -E_J \cos(\phi/2) &\sum_{N=-\infty}^{+\infty} \left(|N+1\rangle\langle N| + |N-1\rangle\langle N|\right), \end{aligned} \tag{3.31}$$

where $E_C \approx e^2/(2 \cdot 2C_J)$.

The cavity's direct coupling to the CPT appears as an unwanted gate modulation, as can be inferred from Eq. (3.30). This can however be neglected as long as $C_g \ll C_J$.

Table 3.1: Numerical values of the parameters used in the simulations. The parameters are based on the experimental cCPT device.

Parameter	Value
Length of microwave resonator l	5135 μm
Capacitance per unit length $\mathcal{C}_c$	0.17 nF/m
Inductance per unit length $\mathcal{L}_c$	0.41 μH/m
Coupling capacitance C_{pc}	7.95 fF
Bare cavity resonance ω_0	5.76 GHz
CPT capacitance C_{CPT}	90 aF
Gate capacitance C_g	6.27 aF
Charging energy E_C/h	53.49 GHz
Josephson energy E_J/h	15.17 GHz
Asymmetry in Josephson energy δE_J	205 MHz

3.2.3. Adiabatic Elimination of the CPT Dynamics

We now look at the CPT dynamics utilizing the Hamiltonian dervied in Eq. (3.30) under the limiting case $E_J < E_C$. Specifically, we will assume the parameter values as given in Table 3.1, and also take into account a small asymmetry in the JJ energies. The accompanying simulations allow us to look at a truncated basis of the CPT Hamiltonian.

Treating $\phi(t)$ and N_p^{in} as static, commuting numbers, the Hamiltonian (3.30) can be diagonalized assuming an approximate, finite dimensional Hilbert space truncation to obtain the CPT energy eigenvalues. Figure 3.4 shows the CPT ground and first excited energy eigenvalue characteristics within a gate polarization range $0 \leq n_g \leq 2$ and a displaced cavity phase range $0 \leq \phi \leq 2\pi$. Figure 3.4a plots the maximum error of the CPT ground energy as a function of ϕ for different charge state basis number truncations relative to a ten charge state basis truncation. As is evident from this figure, a five charge state approximation gives negligible error, and will thus be employed for all subsequent simulations and experimental characterization of the cCPT.

Assuming small N_p^{in}, we see that the CPT approaches charge degeneracy as $n_g \to \pm 1$ (Fig. 3.4b). As a result, the system has an increased probability of transitioning to the first excited energy eigenstate in this limit. The experimental characterization [14] also observes quasiparticle poisoning close to charge degeneracy, as a consequence of lower electrostatic energies of odd electron-states as compared to the CPT charging energy [98, 99]. Taking into account both these factors, we further limit our considered gate polarization range to $-0.9 \leq n_g \leq 0.9$. The CPT level splitting between the ground and excited states over this modified range of bias space (n_g, ϕ) is much

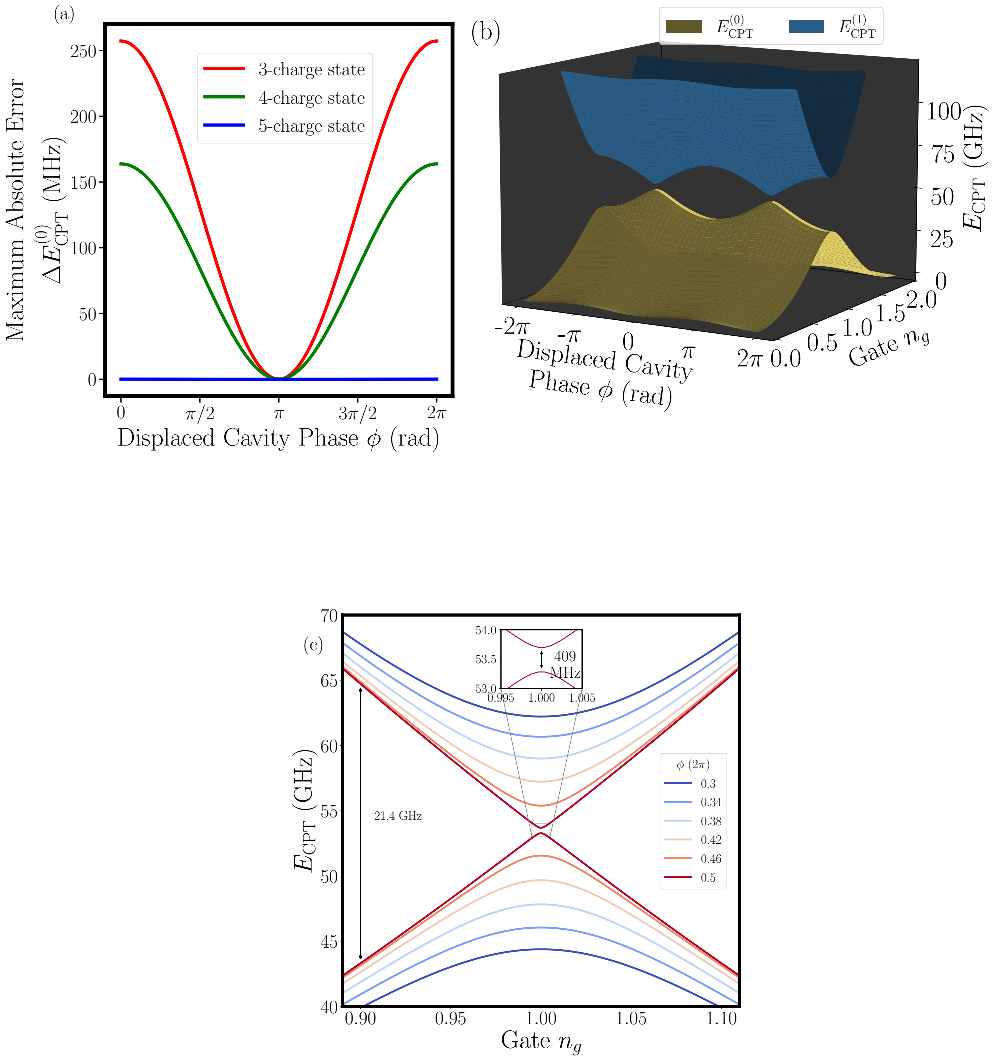

Figure 3.4: (a) Maximum absolute error in the CPT ground state energy for different charge state number-truncations as a function of the displaced cavity phase ϕ. The maximum value is determined by scanning across the entire range of gate-bias n_g. (b) The ground and first excited energy band-structure of the CPT. Note that the adiabatic approximation may break down in the vicinity of charge degeneracy: $n_g = \pm 1$. (b) Energy splitting between the ground and first excited state in the vicinity of charge degeneracy. For $|1 - n_g| \geq 0.1$, the adiabatic approximation holds since the energy splitting is much greater than the characteristic frequencies of the system. The parameter values used for these simulations are provided in Table 3.1.

larger than the other characteristic frequencies of the system, namely the bare cavity fundamental mode frequency and similar drive frequency (≈ 5.76 GHz), and the gate modulation frequency ω_g ($\sim$ tens of MHz) (Fig 3.4c). We thus impose the valid and essential approximation going forward to the effect that if the cavity 'dressed' CPT is initially in its lowest energy eigenstate with energy $E^{(0)}_{\mathrm{CPT}}$, it will remain in this state for the duration of the measurement, evolving adiabatically.

3.2.4. Effective Cavity Dynamics

The adiabatic elimination of the CPT from the total Hamiltonian dynamics effectively replaces the Hamiltonian (3.30) by its ground state energy $E^{(0)}_{\mathrm{CPT}}$, which can subsequently be used to obtain the cavity phase equation of motion counterpart to Eq. (3.19). Invoking the wave equation (2.49) and boundary condition (3.17), we arrive at

$$\phi_c'(0^+,t) - \frac{C_{\mathrm{CPT}}}{\mathcal{C}_c}\phi_c''(0^+,t) - \frac{\mathcal{L}_c}{\mathcal{L}_p}\phi_p'(0^-,t) - \left(\frac{2\pi}{\Phi_0}\right)^2 \mathcal{L}_c \frac{\partial E^{(0)}_{\mathrm{CPT}}}{\partial \phi_c} = -\frac{2\pi\mathcal{L}_c C_g C_{J1}}{\Phi_0 C_\Sigma}\dot{V}_g. \tag{3.32}$$

We identify the above expression as the modified boundary condition at $x = 0$ coupling the cavity and pump/probe transmission line, and including the dressed CPT contribution as a perturbation [c.f. Eq. (2.51)]. We may now follow the same operator scattering method steps as carried out for the bare cavity case in Sec. 2.3.2 to obtain the renormalized resonant cavity fundamental frequency. Before deriving this explicitly, we first simplify Eq. (3.32) by renormalizing the bare cavity Hamiltonian (2.64), which now has an effective potential given by

$$V_{\mathrm{eff}} = (\Phi_0/2\pi)^2\,\phi_0^2/2L_0 + E^{(0)}_{\mathrm{CPT}}(\phi_0), \tag{3.33}$$

restricted to the fundamental phase coordinate mode ϕ_0, where $L_0 = 8\mathcal{L}_c l/\pi^2$ is the corresponding fundamental mode inductance.

The CPT introduces anharmonicity to varying orders when expanded about the equilibrium point $\bar{\phi}_0(n_g, \Phi_{\mathrm{ext}})$ obtained through the condition,

$$\left(\left(\frac{\Phi_0}{2\pi}\right)^2 \frac{\phi_0}{L_0} + \frac{\partial E^{(0)}_{\mathrm{CPT}}}{\partial \phi_0}\right)\Bigg|_{\bar{\phi}_0} = 0. \tag{3.34}$$

As is evident in Fig 3.5a, this shift in equilibrium is much less than one in magnitude over the considered (n_g, Φ_{ext}) bias range, and can be neglected. This simplifies the dependence $\phi(\phi_c, \Phi_{\text{ext}})$ to $\phi(\Phi_{\text{ext}})$ in Eq. (3.20).

Following the same operator scattering method steps as utilized for the bare cavity case (§2.3.2), we can now derive the tunable resonance of the cCPT, but now with the boundary condition (3.32) replacing the simpler, bare cavity boundary condition (2.51). For a sinusoidal gate modulation frequency $\omega_g \ll \omega_0$ and amplitude $\delta n_g^{(0)} \ll 1$, the term in the RHS of Eq. (3.32) can be neglected. Under these assumptions, we proceed by Taylor expanding the term $\partial E_{\text{CPT}}^{(0)}/\partial\phi_c$ in Eq. (3.32) to obtain:

$$\phi_c'(0,t) - \frac{C_{\text{CPT}}}{\mathcal{C}_c}\phi_c''(0,t) - \frac{\mathcal{L}_c}{\mathcal{L}_p}\phi_p'(0,t) \tag{3.35}$$

$$- \left(\frac{2\pi}{\Phi_0}\right)^2 \mathcal{L}_c \sum_{n=1}^{\infty}\sum_{k=0}^{n}\frac{1}{n!}\binom{n}{k}\phi_c(0,t)^k \times \left.\frac{\partial^{n+1}E_{\text{CPT}}^{(0)}}{\partial\phi_c^{k+1}\partial n_g^{n-k}}\right|_{n_g=n_g^{(0)},\phi_c=0}\delta n_g^{n-k} = 0, \tag{3.36}$$

where $\binom{n}{k}$ is the binomial coefficient, $n_g(t) = n_g^{(0)} + \delta n_g(t)$ and the gate modulation $\delta n_g(t) = \delta n_g^{(0)}\cos(\omega_g t) - N_p^{\text{in}}(t)$.

Utilizing the operator scattering solutions in Eq. (2.55) for the cavity phase field and in Eq. (2.56) for the pump phase field, we arrive at the following modified pump-cavity coupled equation in frequency space:

$$\begin{aligned}
&\left\{\cos(\omega l/v_c) - \omega Z_c\left[\frac{C_{pc}}{1+(\omega Z_p C_{pc})^2} + \delta C\right]\sin(\omega l/v_c)\right\} a_c^{\rightarrow}(\omega, t_0)\\
&- i\frac{\left(\omega\sqrt{Z_c Z_p}C_{pc}\right)^2}{1+(\omega Z_p C_{pc})^2}\sin(\omega l/v_c)\, a_c^{\rightarrow}(\omega, t_0) = -ie^{-i\omega(t_0+l/v_c)}\frac{\omega\sqrt{Z_p Z_c}C_{pc}}{1-i\omega Z_p C_{pc}}a_p^{\text{in}}(\omega)\\
&- Z_c\left(\frac{2\pi}{\Phi_0}\right)^2\sum_{n=2}^{\infty}A_{(n,2)}\left.\frac{\partial^{(n+1)}E_{\text{CPT}}^{(0)}}{\partial\phi_c^2\partial n_g^{(n-1)}}\right|_{n_g=n_g^{(0)},\phi_c=0} + \mathcal{O}(\phi_c^2),
\end{aligned} \tag{3.37}$$

where we have limited the expansion to first order in ϕ_c, leaving out anharmonic terms. As for the bare cavity case [Eq. (2.57)], the renormalized frequency due to the CPT and transmission line coupling can be obtained by equating the terms in curly brackets to zero. However, the resonant frequency shift contains an extra term due

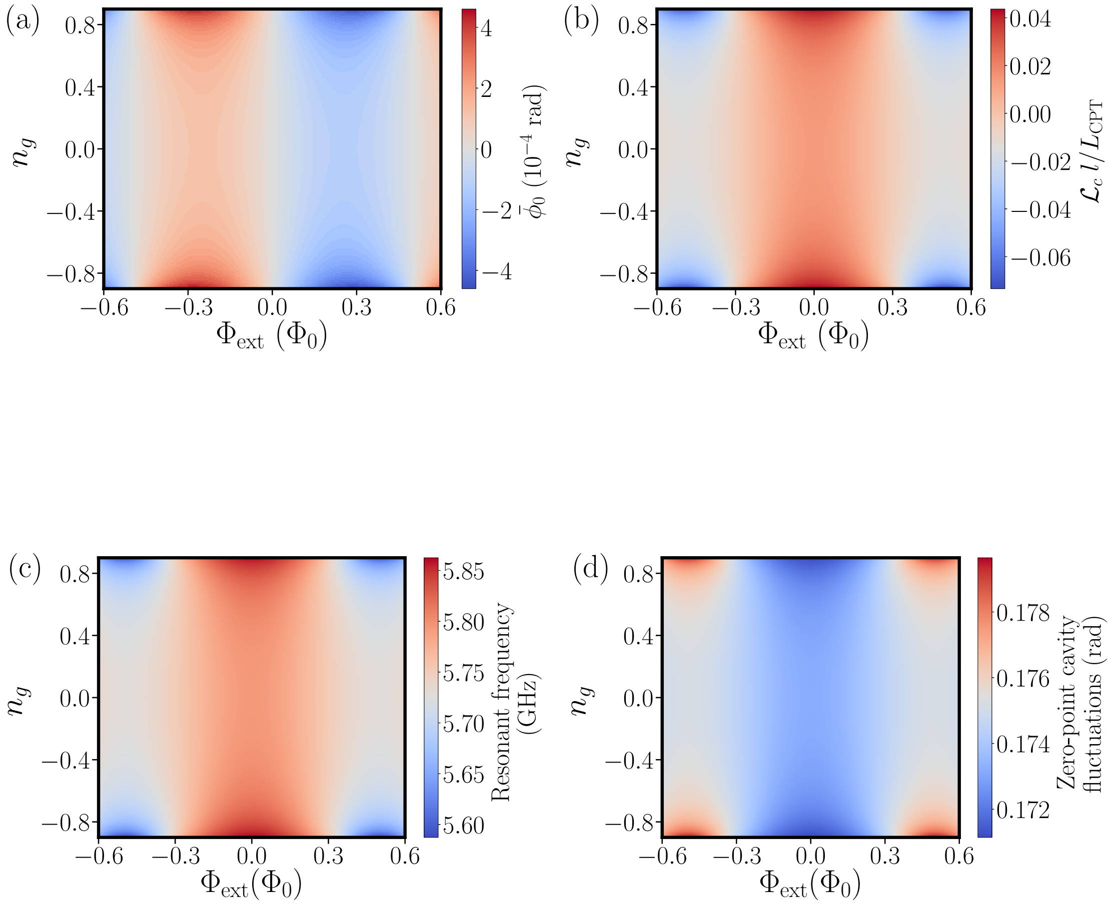

Figure 3.5: (a) The shift in the equilibrium point corresponding to the minimum effective potential energy as function of n_g and $\Phi_{\rm ext}$. (b) The smallness of the ratio of cavity inductance to the CPT inductance ensures that the CPT weakly perturbs the cavity. (c) Resonance frequency shift of the cavity across the tunable bias range. (d) Plot of zero-point fluctuations as a function of n_g and $\Phi_{\rm ext}$. The shift from the original value is negligible for our system.

to the shifted δC in the above expression given by

$$\delta C = C_{\text{CPT}} - \omega^{-2}\left(\frac{2\pi}{\Phi_0}\right)^2 \left.\frac{\partial^2 E^{(0)}_{\text{CPT}}}{\partial \phi_c^2}\right|_{\phi_c=0}. \tag{3.38}$$

The LHS of the second line corresponds to the cavity damping rate due to coupling to the transmission line, the RHS of the second line describes the transmission line noise, and the third line gives the gate voltage and noise modulations of the cavity frequency, where the coefficient $A_{(n,2)}$ takes the form

$$A_{(n,2)} = \frac{1}{2\pi}\int_{-\infty}^{+\infty} dt \int_0^{\infty} \frac{d\omega'}{\sqrt{\omega\omega'}} e^{i(\omega-\omega')(t-t_0-l/v_c)} \frac{\delta n_g(t)^{n-1}}{(n-1)!} \sin\left(\omega' l/v_c\right) a_c^{\rightarrow}(\omega', t_0). \tag{3.39}$$

As before, defining the dimensionless frequency as $\tilde{\omega} \equiv \omega l/v_c$ and the small dimensionless CPT-transmission line coupling parameter $\xi = v_c C_{pc} Z_c/l = C_{pc}/\mathcal{C}_c l \ll 1$, we can express the term in curly brackets as

$$\cos\tilde{\omega} - \left[\frac{\tilde{\omega}\xi}{1+(\tilde{\omega}\xi)^2} + \tilde{\omega}\frac{C_{\text{CPT}}}{\mathcal{C}_c l} - \tilde{\omega}^{-1}\frac{\mathcal{L}_c l}{L_{\text{CPT}}}\right]\sin\tilde{\omega}, \tag{3.40}$$

with the CPT inductance L_{CPT} defined as

$$L^{-1}_{\text{CPT}} = \left(\frac{2\pi}{\Phi_0}\right)^2 \left.\frac{\partial^2 E^{(0)}_{\text{CPT}}}{\partial \phi_c^2}\right|_{\phi_c=0} = \frac{\partial^2 E^{(0)}_{\text{CPT}}}{\partial \Phi^2_{\text{ext}}}, \tag{3.41}$$

utilizing Eq. (3.20). Setting expression (3.40) to zero, and in the limit where the CPT weakly perturbs the cavity fundamental resonance, i.e., $C_{\text{CPT}}/\mathcal{C}_c l$ and $\mathcal{L}_c l/L_{\text{CPT}} \ll 1$ (Fig 3.5b), we obtain the following expression for the tunable resonance:

$$\omega_0(n_g, \Phi_{\text{ext}}) \approx \frac{\pi v_c}{2l}\left[1 - \frac{C_{pc}+C_{\text{CPT}}}{\mathcal{C}_c l} + \left(\frac{2}{\pi}\right)^2 \frac{\mathcal{L}_c l}{L_{\text{CPT}}}\right]. \tag{3.42}$$

The simulated frequency response as per this model for the parameters given in Table 3.1 is plotted in Fig. 3.5c.

3.2.5. The cCPT Hamiltonian

Let us now look at the Hamiltonian of the cavity-CPT system that explicitly shows the inherent nonlinearity of this system. As shown in Eq. (3.33), the higher terms in the expansion of the effective potential V_{eff} give rise to anharmonicity in the combined cCPT system which takes the form:

$$V_{\text{eff}} = \left(\frac{\Phi_0}{2\pi}\right)^2 \frac{\phi_0^2}{2L_0} + \sum_{n=2}^{\infty} \sum_{k=2}^{n} \frac{1}{n!} \binom{n}{k} \phi_0^k \delta n_g^{n-k} \left. \frac{\partial^n E_{\text{CPT}}^{(0)}}{\partial \phi_0^k \partial n_g^{n-k}} \right|_{n_g = n_g^{(0)}, \phi_0 = 0}, \quad (3.43)$$

where renormalization and having the minimum potential at $\phi_0 \sim 0$ lead to vanishing terms for $k = 0$ and 1, respectively. Expression (3.43) also involves an expansion in the gate polarization variation δn_g in order to account for gate voltage modulations relevant for electrometry (discussed in Chapter 5). The total Hamiltonian is

$$H_{\text{cCPT}} = \left(\frac{2\pi}{\Phi_0}\right)^2 \frac{p_0^2}{2C_0} + V_{\text{eff}}, \quad (3.44)$$

where C_0 is renormalized to $C_0 + C_{\text{CPT}}$ following the renormalized frequency expression in Eq. (3.42). As for the bare cavity case [see Eq. (2.64)], the phase operator of the fundamental cavity mode is expressed in terms of the photon creation/annihilation operators as follows: $\phi_0 = \phi_{zp}\left(a_0 + a_0^\dagger\right)$, with the zero-point fluctuations given by [c.f. eq. (2.65)]

$$\phi_{zp} = \left(\frac{2\pi}{\Phi_0}\right) \sqrt{\frac{\hbar}{2C_0\omega_0}}. \quad (3.45)$$

The generalized nonlinear cCPT Hamiltonian thus becomes

$$H_{\text{cCPT}} = \hbar\omega_0(n_g, \Phi_{\text{ext}}) a_0^\dagger a_0 + \sum_{n=3}^{\infty} \sum_{k=2}^{n} V_{n,k} \left(a_0 + a_0^\dagger\right)^k, \quad (3.46)$$

where the resonance shift is tunable as derived in Eq.(3.42) and the coefficient $V_{n,k}$ can be expressed as

$$V_{n,k} = \frac{1}{n!} \binom{n}{k} \phi_{zp}^k \delta n_g^{n-k} \left. \frac{\partial^n E_{\text{CPT}}^{(0)}}{\partial \phi^k \partial n_g^{n-k}} \right|_{n_g^{(0)}, 2\pi\Phi_{\text{ext}}/\Phi_0}. \quad (3.47)$$

We now make a few remarks about the Hamiltonian (3.46). First, the tunability of the cavity frequency results in the tunability of the zero-point fluctuations of the cavity phase coordinate itself, i.e., $\phi_{zp} = \phi_{zp}(n_g, \Phi_{\rm ext})$. Typical applications of similar devices generally operate in the high-photon limit, where the relatively small variations in the zero-point motion of the cavity do not have a substantial effect. In the low-photon limit however, the tunability in the zero-point fluctuations can become relevant, as this may potentially be utilized to access stronger quantum fluctuation regimes. For our device, the range of variation of ϕ_{zp} is found to be $\sim 5\%$ in the tunability range of our interest (Fig 3.5d).

Second, the experimental characterization is typically conducted in the limit of small gate modulation magnitude $|\delta n_g| \ll 1$. Additionally, the noise $N_p^{\rm in}$ originating via the probe coupling to the CPT can also be neglected as long as $C_g \ll C_\Sigma$. We may thus restrict the potential energy expansion in (3.46) to first order in δn_g. The simplified form becomes

$$H_{\rm cCPT} = \hbar\omega_0(n_g, \Phi_{\rm ext}) a_0^\dagger a_0 + \sum_{n=3}^{\infty} V_{n,n} \left(a_0 + a_0^\dagger\right)^n + \sum_{n=3}^{\infty} V_{n,n-1} \left(a_0 + a_0^\dagger\right)^{n-1}. \quad (3.48)$$

The above Hamiltonian can be engineered as per the specific application by fixing the drive frequency and power, as well as via gate and flux modulations. For instance, the cCPT can be selectively setup to perform as an ultra-sensitive (both linear and nonlinear) electrometer, magnetometer, parametric amplifier etc. We will briefly look at some of these interesting regimes below.

Rotating Wave Approximation: We may use a rotating wave approximation (RWA) to simplify the Hamiltonian to contain only terms leading to an unchanged photon number in the cavity. In particular, when we transform to the rotating frame of the pump frequency ω_p driven near the fundamental resonance ω_0, contributions leading to changing photon number rapidly oscillate in this frame and can thus be neglected. For simplicity, we will restrict to the cases valid up to $\mathcal{O}(\phi_0^4)$. Consequently, we arrive at the simplified Hamiltonian of the cCPT device:

$$H_{\rm cCPT} = \hbar\left(\omega_0 + g\delta n_g\right) a_0^\dagger a_0 + \hbar\left(\frac{K}{2} + g_K \delta n_g\right) a_0^{\dagger 2} a_0^2, \quad (3.49)$$

where the renormalized resonance frequency is given by

$$\omega_0(n_g, \Phi_{\rm ext}) \to \omega_0(n_g, \Phi_{\rm ext}) + \frac{\phi_{zp}^4}{2\hbar} \left.\frac{\partial^4 E_{\rm CPT}^{(0)}}{\partial\phi^4}\right|_{(n_g^{(0)}, 2\pi\Phi_{\rm ext}/\Phi_0)}, \quad (3.50)$$

the gate polarization coupling g can be derived as

$$g = \left[\frac{\phi_{zp}^2}{\hbar} \frac{\partial^3 E_{\mathrm{CPT}}^{(0)}}{\partial \phi^2 \partial n_g} + \frac{\phi_{zp}^4}{2\hbar} \frac{\partial^5 E_{\mathrm{CPT}}^{(0)}}{\partial \phi^4 \partial n_g} \right] \Bigg|_{(n_g^{(0)}, 2\pi\Phi_{\mathrm{ext}}/\Phi_0)} , \tag{3.51}$$

the Kerr nonlinear contribution to the cavity is determined by the Kerr coefficient K:

$$K = \frac{\phi_{zp}^4}{2\hbar} \frac{\partial^4 E_{\mathrm{CPT}}^{(0)}}{\partial \phi^4} \Bigg|_{(n_g^{(0)}, 2\pi\Phi_{\mathrm{ext}}/\Phi_0)} , \tag{3.52}$$

and Kerr-enhanced charge sensing can be achieved using the gate polarization g_K

$$g_K = \frac{\phi_{zp}^4}{4\hbar} \frac{\partial^5 E_{\mathrm{CPT}}^{(0)}}{\partial \phi^4 \partial n_g} \Bigg|_{(n_g^{(0)}, 2\pi\Phi_{\mathrm{ext}}/\Phi_0)} . \tag{3.53}$$

In this thesis work, we will focus on the gate polarization coupling g given in Eq. (3.51) in the few-photon limit. Details about the applicability of the cCPT as an ultra-sensitive, quantum-limited electrometer in this regime is presented in chapter 5. Kerr nonlinear applications of the cCPT are discussed extensively in Brock's [65] and Thyagarajan's theses.

Section 3.3

Experimental Realization

The experimental realization of the cCPT sample is presented in the form of a summary in this section. The subsection 3.3.3 provides extraction of the parameters of the cCPT considering its two-dimensional tunability, and a comparison with the theory. For a thorough review of the fabrication and the experimental characterization of the cCPT, consult the theses by Juliang Li [82] and Ben Brock [65], respectively.

3.3.1. Fabrication

The cCPT sample fabrication was primarily carried out by Juliang Li, a former graduate student of the Rimberg Lab. The $\lambda/4$-wave resonators were fabricated by William Braasch, another former graduate student, under the guidance of McDermott's Lab in the University of Wisconsin.

The sample images of the cCPT are shown in Fig. 3.6. The $\lambda/4$-wave resonator is

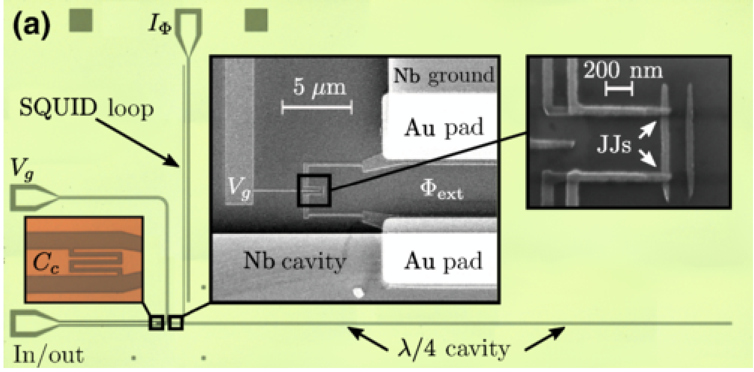

Figure 3.6: cCPT sample images as reported by Brock *et al.* [14]

a Nb cavity with a coplanar waveguide geometry and is fabricated using photolithography. Since Nb becomes superconducting at 9.2 K, the cavity displays a high internal quality factor at cryogenic temperatures due to reduced resistive losses. As shown in this figure, the CPT connects the voltage antinode and the ground plane of the cavity and is formed using two JJs in series. The CPT fabrication involves ebeam lithography and a double layer shadow evaporation with Al acting as the superconductor and Al_2O_3 as the tunnel barrier. The tunability is induced via controlling the charge and flux of the environment. The island charge is tuned via a gate voltage V_g through a capacitance C_g. The cavity phase and the junction phases are coupled via an L-shaped SQUID loop, which is controllable via an external flux, introduced using another coplanar line placed perpendicular to the cavity to reduce cavity losses induced by the current line. The input/output transmission line couples to the cavity through an interdigitated capacitor C_{pc} (labeled C_c in the figure). In order to achieve impedance matching, all the coplanar lines are designed to have a characteristic impedance of 50 Ω.

3.3.2. Measurement Setup

The circuit diagram enabling reflection measurements are shown in Fig. 3.7. The input and outlines are separated via a microwave circulator. The attenuators placed at different temperature stages of the dilution refrigerator ensure high SNR of the input signal entering the cavity. The output signal is amplified at multiple stages, with a HEMT as the first-stage amplifier. Finally, separate rf lines for gate and flux allows for the modulated-response of the cavity.

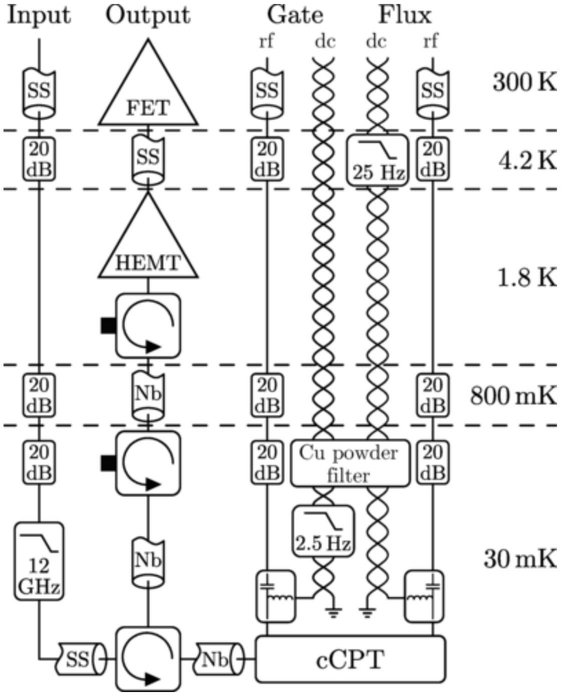

Figure 3.7: Circuit schematic used for the reflection measurements of the cCPT, taken from [14].

3.3.3. cCPT Characterization

In order to compare the validity of our model presented in §3.2, we now characterize the observed tunable resonant frequency response of the cCPT. Note that we may also arrive at an identical expression for $\omega_0(n_g, \Phi_{\text{ext}})$ [see Eq.(3.42)] of the cCPT using a simplified lumped-element model under the limits of C_{CPT}/C_0, $L_0/L_{\text{CPT}} \ll 1$. In this case, the Josephson inductance of the cCPT is modeled as a parallel addition to the lumped-element model of the microwave resonator considered in §2.2 [see Eq. (2.23)], as follows.

Equation (2.15) for the cavity resonant frequency can be reexpressed in terms of a renormalized total capacitance $C_0 \rightarrow C_0 + C_{pc}$ where we consider the fundamental mode $C_n = C_0$. Hence, the addition of the CPT shifts the resonance via an effective capacitance $C_{\text{cCPT}} = C_0 + C_{pc} + C_{\text{CPT}}$, and an effective inductance $L_{\text{cCPT}}^{-1} = L_0^{-1} + L_{\text{CPT}}^{-1}$. Consequently, under the conditions C_{CPT}/C_0, $L_0/L_{\text{CPT}} \ll 1$, the cCPT resonant frequency is renormalized to

$$\omega_{\text{cCPT}} \approx \omega_{\lambda/4}\left(1 + \frac{L_0}{2L_{\text{CPT}}} - \frac{C_{pc} + C_{\text{CPT}}}{2C_0}\right), \tag{3.54}$$

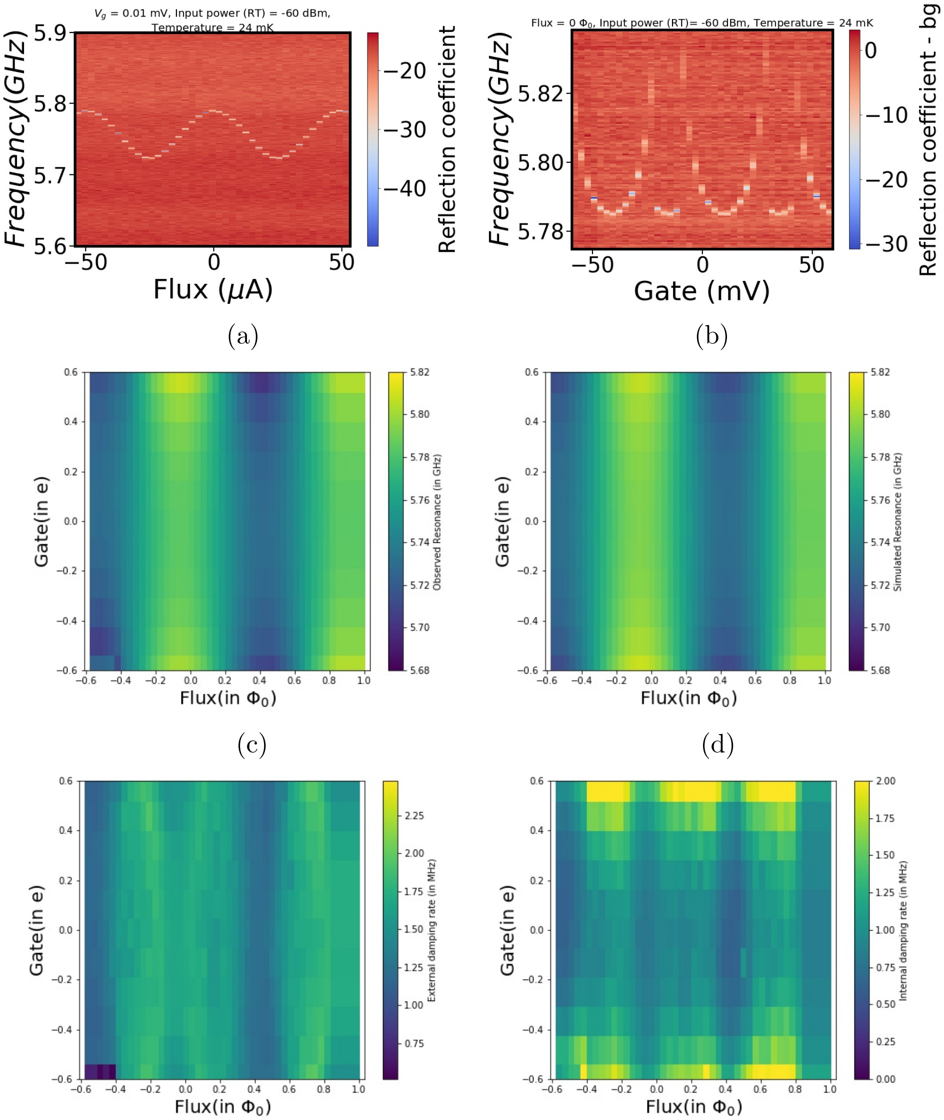

(a) (b)

(c) (d)

(e) (f)

Figure 3.8: (a) Reflection coefficient measured as a function of flux current. This data is used to calibrate the flux offset by identifying the maxima as $\Phi_{\text{ext}} = 0\ \Phi_0$ and minima as $\Phi_{\text{ext}} = 0.5\ \Phi_0$. (b) Reflection coefficient measured as a function of gate voltage at $\Phi_{\text{ext}} = 0\ \Phi_0$. Gate offset is identified from the minimum of the resonant frequency value, and the periodicity $= 2e$. The quasiparticle poisoned regime is also visible in this plot as indicated by the suddent switching from the near-quadratic response of the cCPT. (c) Extracted resonant frequency as a function of gate and flux. (d) Fit for the resonant frequency data in (a) using the theoretical model discussed in §3.2. (e) Extracted value for external damping rate as a function of gate and flux. (f) Extracted values for the internal damping rate. The analysis adopts the reflection coefficient model presented in Eq. (2.37).

Parameter	Value
Length of microwave resonator	5135 μm
Resonant frequency of quarter-wave resonator $\omega_{\lambda/4}$	5.81 GHz
Resonant frequency of loaded quarter-wave resonator ω_0	5.76 GHz
Cavity capacitance per unit length $\mathcal{C}$	1.7e-10 F/m
Cavity inductance per unit length $\mathcal{L}$	4.14e-07 H/m
Cavity capacitance C_0	0.44 pF
Cavity inductance L_0	1.72 nH
Coupling capacitance C_{pc}	7.95 fF
Charging energy E_C	53.5 ± 1.44 GHz
Effective Josephson energy E_J	15.17 ± 0.511 GHz
Josephson energy asymmetry ΔE_J	0.2 ± 0.0187 GHz
Gate capacitance C_g	0.006 fF
cCPT capacitance C_{CPT}	0.09 fF

Table 3.2: Extracted values for the parameters of the cCPT following the experimental characterization and analysis adapting an asymmetric model of the cCPT.

where the mode capacitance $C_n = \mathcal{C}_c l/2 + C_{pc}$ and the mode inductance $L_n = 8\mathcal{L}_c l/(2n+1)^2\pi^2$, as defined in Eq. (2.63).

By measuring the reflection coefficient $S_{21}(\delta\omega)$ of the cCPT as a function of gate and flux, and further using the impedance-mismatched model for $\tilde{S}_{21}$ [see Eq. (2.37)], we first extract the resonant frequency, internal damping rate and external damping rate of the cCPT's response to gate and flux. The relevant parameters shown in Table 3.2 are then extracted by applying the model for the resonant frequency in Eq. (3.54). A 5-charge truncated basis is used for this analysis to extract the inductance L_{CPT} [see Fig. 3.4a]. The analysis is done separately for the symmetric and asymmetric models of the cCPT (i.e., considering $\Delta C_J \neq 0$ and $\Delta E_J \neq 0$).

The results of this analysis are plotted in Fig. 3.8. The deviation of the cCPT characteristics in an experimental setting when compared to our theoretical model occurs due to two limiting factors. One important feature to take note of is the switching of the resonance to the odd parity due to quasiparticle poisoning. In the particular sample used for this analysis, the quasiparticle poisoning begins to dominate at $n_g = 0.65$. As a result, the data points over the regime $|n_g| \leq 0.65$ was used for checking the model validity, and the regime $|n_g| \geq 0.7$ is typically inaccessible at most bias points. Moreover, notice the variation in the internal and external damping rates over varying bias points. This deviation occurs due to increased low-frequency noise in the resonant frequency of the cCPT in the flux and charge sensitive regimes, i.e., near $\Phi_{\mathrm{ext}} = 0.25\ \Phi_0$ and $n_g \to 1$, respectively. These fluctuations are averaged out in reflection measurements by the VNA causing the measured damping rates to increase from the original values. Analysis that takes these fluctuations into account is discussed in Ref. [14]. Stabilization of such frequency fluctuations is important to achieve ultra-sensitive measurements using the cCPT; this can be achieved using feedback techniques as reported in the next chapter.

Chapter 4

Environmental Noise Decoupling[1]

We concluded the previous chapter pointing towards the manifestation of the low-frequency noise in the experimental characterization of the cCPT. The complete noise characterization of this charge- and flux-tunable microwave cavity reported in Ref. [14] addresses the role of the intrinsic noise in charge/flux bias leading to resonant frequency fluctuations, especially in regions where the cCPT can operate as a highly sensitive electrometer/magnetometer. By singling out bias regions where the cCPT is maximally sensitive to charge/flux fluctuations, measurements detected typical charge and flux noise spectral densities of the form $S_{\mathrm{qq}} \propto 1/f\ \mathrm{e}^2/\mathrm{Hz}$, and $S_{\Phi\Phi} \propto \sqrt{1/f}\ \Phi_0^2/\mathrm{Hz}$, respectively.

While there exist several detection techniques for the measurement of such low-frequency noise [100, 67, 101], methods to suppress these fluctuations in real-time can lead to major breakthroughs in several areas of research, ranging from charge detection to applications in qubit metrology [35, 39, 102]. In this chapter, we report a reduction of these resonant frequency fluctuations induced by the intrinsic charge/flux noise on the cCPT. The scheme to achieve this reduction follows the well-established technique of Pound-Drever-Hall (PDH) locking, extensively used in laser optics to stabilize laser sources during cavity reflection measurements [66]. As mentioned in the introduction, such a study is of two-fold importance to the general circuit-QED audience. Firstly, as the cCPT is specifically designed to be a highly sensitive electrometer/magnetometer, it is an ideal candidate for understanding and suppressing

---

[1] We acknowledge that a good volume of this chapter is reproduced from a publication by Kanhirathingal *et. al.* [18], currently under peer review.

the associated effects of such $1/f$-noise commonly found in these devices. Secondly, stabilizing the resonant frequency fluctuations can elevate the cCPT into a superior charge sensing regime compared to previously reported results for the same cCPT device [15].

The chapter layout is as follows. First, in Sec. 4.1, we present a brief review of the Pound locking technique which can be implemented to detect low-frequency noise in microwave resonators. In §4.2, we then describe the basic circuit scheme that suppresses the resonant frequency fluctuations caused by intrinsic charge/flux noise in tunable microwave cavities, along with a theoretical model using cavity field operators. In this same section, we will also discuss the scheme for the specific case of the cCPT, with particular consideration given to its Kerr-nonlinearity, as well as to the two-dimensional parameter space spanned by gate and flux tunability. We next provide the actual experimental setup in Sec. 4.3, discussing in detail the series of steps to maximize the SNR at the single-photon level. Following this, we report the results proving resonant frequency stabilization under feedback locking in Sec. 4.4. In §4.5, the empirical limitations as well as potential improvements of our technique are explored.

Section 4.1

Pound-Drever-Hall Locking

As in the previous chapters, this beginning section presents an overview of the topic of interest. We will set up the concepts describing feedback techniques in the noise characterization of resonators. In particular, we will look at the renowned technique of Pound-Drever-Hall (PDH) locking, originally used in laser optics and further adapted to noise measurements of microwave resonators.

4.1.1. Concept

Pound locking is a well-established technique in optics that ensures the frequency stabilization of unstable laser sources by locking the signal to the resonant frequency of a stable optical cavity. A conceptual discussion of the technique can be found in Black *et. al.* [66]. Here, an unstable commercial laser source is stabilized to provide a signal at the cavity resonance ω_0 using a feedback mechanism. In essence, the idea is to extract an error signal that can correctly track the sign and magnitude of the deviation of the drive signal from resonance and utilize this dynamic information to correct for the net frequency shift. It relies on the fact that the reflected intensity, for e.g., in a Fabry-Perot cavity, is minimum at resonance. As a result, the derivative of reflected intensity with respect to the frequency, about the resonant frequency is antisymmetric, i.e., $\omega < \omega_0$ is negative and $\omega > \omega_0$ is positive. The setup measures and nullifies this variation which is fed back into the laser source, thus correcting the signal frequency in real time.

In practice, the frequency variation required to extract info on the derivative of reflected intensity is better achieved by phase modulating the input signal. Following [66], for a cavity with reflection coefficient given by $r(\omega)$, the reflected power $P_{\mathrm{ref}} = P_0 \left|r(\omega)\right|^2$. Thus for a phase-modulated input beam,

$$P_{\mathrm{ref}}\left(\omega + \omega_{\mathrm{m}}\beta\cos(\omega_{\mathrm{m}}t)\right) \approx P_{\mathrm{ref}}(\omega) + \omega_{\mathrm{m}}\beta\cos(\omega_{\mathrm{m}}t)\frac{dP_{\mathrm{ref}}}{d\omega}, \tag{4.1}$$

where the phase modulation $\theta = \beta\cos(\omega_{\mathrm{m}}t)$ modifies the frequency via $\omega = d\theta/dt$ such that $\omega \to \omega + \omega_{\mathrm{m}}\beta\cos(\omega_{\mathrm{m}}t)$. The sinusoidal features are determined by the phase modulation amplitude β and the modulation frequency ω_{m}. The second term in the above expression thus oscillates at the frequency ω_{m} and contains the quantity of our interest, which is the derivative of the intensity $dP_{\mathrm{ref}}/d\omega$. To extract this quantity, the reflected beam is first directed to a photodetector to measure the reflected power. A mixer then extracts the component at the modulation frequency which is proportional to the derivative of reflected intensity, giving the error signal.

It is important to note that the rate at which the frequency is modulated provides a varying error signal in the regimes $\omega_{\mathrm{m}} \gg \kappa_{\mathrm{tot}}$ and $\omega_{\mathrm{m}} \ll \kappa_{\mathrm{tot}}$. This can be understood in terms of interference of the input signal before entering the cavity with the leaked signal from the cavity. If we vary the frequency slowly, the delayed signal after entering the cavity interferes with the instantaneous input beam of some frequency within the line width of cavity, creating a non-ideal scenario. For faster modulation, the signal produces sidebands about the carrier frequency well outside the line width of the cavity. This ensures the sidebands do not enter the cavity, thus making the detection easier by separating the two tones and resulting in a much sharper and linear response. Demonstration of both these regimes are provided in the following subsection.

4.1.2. Pound Locking in Superconducting Microwave Resonators

Unlike laser optics, measurements in superconducting microwave resonators pose an inverse issue. These resonators are susceptible to higher internal losses, in general caused due to two-level system defects on the substrate. Coupling to such fluctuating systems results in jitter of the resonant frequency of the resonator. Reflection and transmission measurements are mostly done using vector network analyzers (VNAs), where the time span of these measurements are usually larger than the typical fluctuation time scales, leading to inaccuracy in the measured damping rates. Numerous techniques are available in the literature to look into such frequency noise generated in the superconducting resonators [100, 67, 101].

One scheme [67] that has proven incredibly efficient in the detection of these fluctuations is an adaptation of the Pound locking technique. In this case, the extracted error signal is fed back into a PID controller that corrects the drive frequency such that it continuously tracks the fluctuating resonant frequency of the resonator. A few advantages of using such a scheme to characterize low-frequency noise are

- The resonant fluctuations can be tracked in a time scale much faster than typical measurements that use averaged-VNA data or a spectrum analyzer to extract the noise components.
- The efficiency of many cavity-based detectors rely on a steady input tone exactly at the cavity resonance. A real time tracking of the fluctuating resonance (which otherwise affects the efficiency) can thus be helpful towards building detectors with better performance.
- Detection occurs at the phase modulation frequency (typically MHz) which is less susceptible to vibrational and other external noise factors. On the other hand, phase-locked loops operating near the resonant frequency range (typically GHz) can couple to such external noise and limit the characterization of internal noise parameters.

The thesis by Burnett [103] provides an insightful background into theory and a detailed discussion of this setup in microwave systems. Following the analysis in this reference, we obtain the expression for the error signal as

$$V_{err} \propto \Bigg(\mathrm{Re}[S_{21}(\omega_c)]\left\{\mathrm{Im}[S_{21}(\omega_c+\omega_m)]+\mathrm{Im}[S_{21}(\omega_c-\omega_m)]\right\} \\ -\mathrm{Im}[S_{21}(\omega_c)]\left\{\mathrm{Re}[S_{21}(\omega_c+\omega_m)]+\mathrm{Re}[S_{21}(\omega_c-\omega_m)]\right\}\Bigg), \tag{4.2}$$

with $S_{21}(\omega)$ representing the reflection coefficient of the cavity at frequency ω.

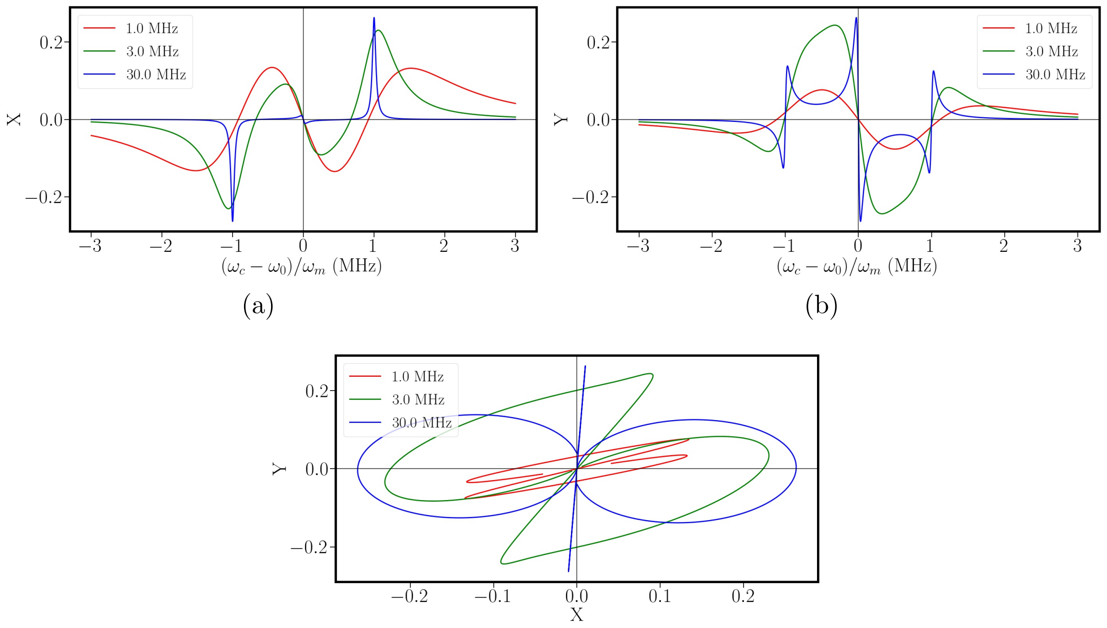

(a)

(b)

(c)

Figure 4.1: (a) Simulated X quadrature as a function of carrier signal for varying modulation frequencies. (b) Corresponding simulated Y quadrature. (c) Parametric plot of X and Y quadrature in phase space. Parameter values: resonant frequency $\omega_0 = 5.756$ GHz, internal quality factor $Q_{\text{int}} = 10^4$, external quality factor $Q_{\text{ext}} = 5000$ and $\beta = 1.8$.

The above expression indicates the response of the error signal for different modulation frequency regimes as mentioned in 4.1.1. We observe that for off-resonance values, the real coefficient of $S_{21}(\omega)$ is one and the imaginary coefficient is zero. Near resonance, the imaginary components are non-zero except exactly at resonance. As a result, in the configuration where $\omega_m \gg \kappa_{\text{tot}}$, the error signal is a monotonic function near resonance and zero elsewhere. Figure 4.1b simulates this response. Clearly, at a higher modulation frequency, the response is sharper and linear as compared to lower values. Also, note the presence of two other peaks at values $\omega_c = \omega_0 \pm \omega_m$ which can accidentally be detected during feedback operation. However, the slopes in these regions is opposite to those of near $\omega_c = \omega_0$. Hence once the feedback polarity is accurately fixed, these regimes are not expected to interfere with the operation.

As a stepping stone towards understanding the operation, limitations and accessibility of the scheme presented in the subsequent sections, we first studied the noise characteristics of the cCPT under the standard Pound locking scheme. For completeness, the circuitry that was used for the detection is given in Fig. 4.2. We will, however, refrain from any detailed discussions of this measurement in this section to remove redundancy.

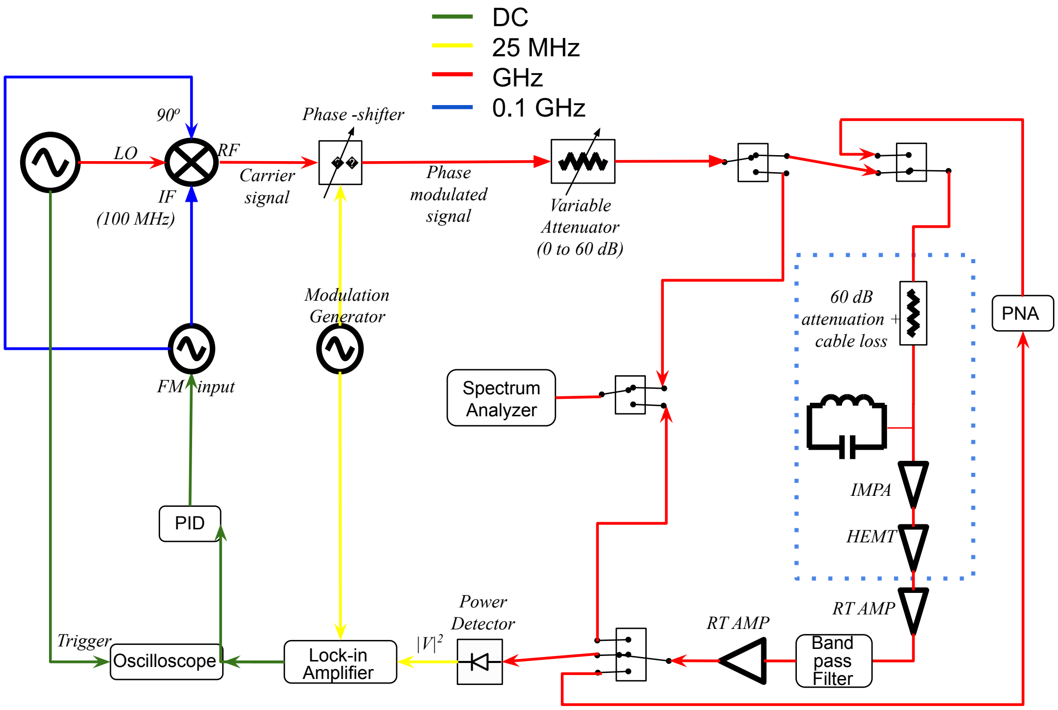

Figure 4.2: Circuitry used for the noise characterization of the cCPT following the standard Pound locking setup. The measurement followed the description given in [103]. The majority of these measurements were carried out at Google's Quantum Computing Hardware Lab in Santa Barbara.

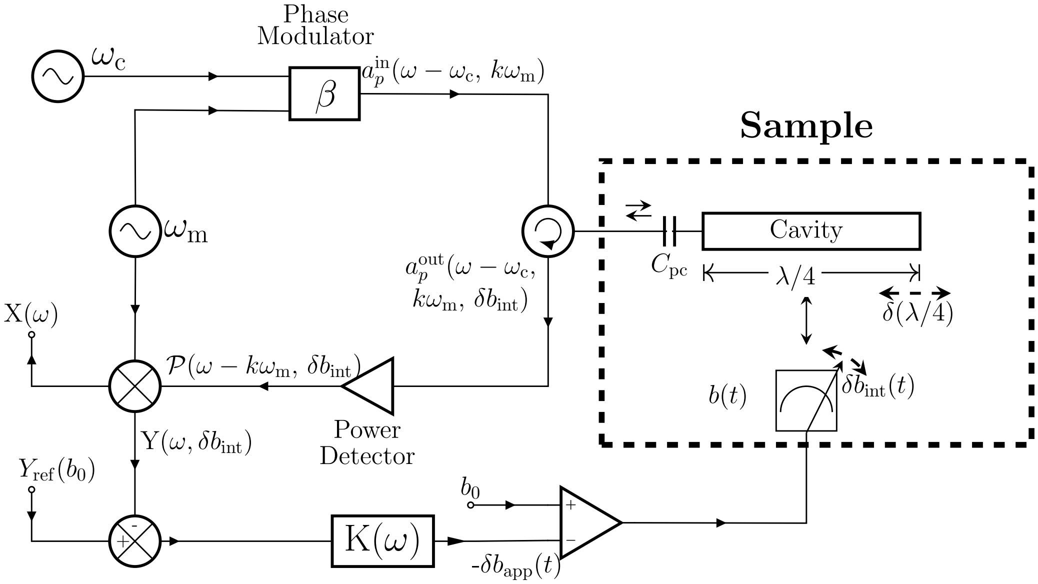

Figure 4.3: Basic feedback-based circuit scheme to stabilize cavity resonant frequency in the presence of intrinsic bias fluctuations $\delta b_{\text{int}}(t)$. The phase-modulated input signal encodes the magnitude of bias fluctuations after reflection from the cavity. By continuously tracking and correcting for the fluctuations in the component of $\mathcal{P}(\omega-k\omega_m,\delta b_{\text{int}})$ oscillating at frequency ω_m, we stabilize the resonance via an applied $\delta b_{\text{app}}(t)$.

Section 4.2

Feedback Stabilization of Microwave Cavities (Theory)

We now move on to the major focus of this chapter, which is the feedback stabilization of the resonant frequency in tunable microwave cavities. This section will begin with a description of the generalized scheme using a field operator approach; we will then look at the details of how to apply the scheme to a two-dimensional tunable cavity – the cCPT.

4.2.1. Concept

We will begin with a tunable cavity at resonance $\omega_0(b)$, displaying a linear reflection coefficient $S_{11}(\Delta)$, with tunability induced via parameter b, and detuning defined by $\Delta=\omega-\omega_0(b)$. The cavity undergoes resonant fluctuations due to undesired coupling with other systems in its environment. Let us assume that these fluctuations are dominated at any time by the intrinsic fluctuations in the bias parameter $b(t)=$

$b_0 + \delta b_{\rm int}(t)$. The exact origins of these fluctuations are not of relevance in the current work. However, we are especially interested in low-frequency noise where the power spectral density (PSD) of the bias noise, given by $S_{bb}(\omega)$, is predominantly $1/f$ in nature. As detailed below, Fig. 4.3 then provides a feedback-based scheme to stabilize the resonant frequency fluctuations by effectively decoupling the low-frequency bias fluctuations from the cavity.

The dashed box in Fig. 4.3 represents our sample, containing a quarter-wave microwave resonator tunable via the parameter b. The cavity undergoes reflection measurements and is connected to the external drive-pump/ measurement-probe transmission line via a coupling capacitor $C_{\rm pc}$. Due to the intrinsic noise $\delta b_{\rm int}(t)$ (typically charge/flux noise), the apparent length of the cavity fluctuates and destabilizes the resonant frequency from its desired point of operation $\omega_0(b_0)$, where we take b_0 to be the bias magnitude at the sample at time t_0. The cavity is driven using a carrier signal $\omega_{\rm c} = \omega_0(b_0)$ phase modulated with a modulation amplitude β and modulation frequency $\omega_{\rm m}$ several times larger than the cavity linewidth $\kappa_{\rm tot}$. As we are particularly interested in cases where the cavity is driven at very low pump powers, we will follow the operator scattering approach used in §3.3 to describe the resulting system dynamics.

Input Field: Treating the system semiclassically, the driving signal is described using $\langle a_p^{\rm in}(t)\rangle$, where $a_p^{\rm in}(t)$ is the annihilation operator of the transmission line input. Phase modulation of the carrier signal transforms the drive as below:

$$\begin{aligned}\langle a_p^{\rm in}(t)\rangle &= \sqrt{\frac{P_p^{\rm in}}{\hbar\omega_{\rm c}}}e^{-i(\omega_c t+\theta_c)} \\ &\rightarrow \sqrt{\frac{P_p^{\rm in}}{\hbar\omega_{\rm c}}}\sum_{k=-\infty}^{k=\infty} J_k(\beta)e^{-i(\omega_c+k\omega_{\rm m})t},\end{aligned} \tag{4.3}$$

where we have applied the Jacobi-Anger expansion to the exponential of the pump phase $\theta_{\rm c} = \beta\sin(\omega_{\rm m}t)$, with $P_{\rm in}$ the average pump power, and where J_k is the Bessel function of the first kind. In Fig. 4.3, we denote the input signal using its spectral components as $a_p^{\rm in}(\omega-\omega_{\rm c}, k\omega_{\rm m})$. We have adopted this notation everywhere in the figure to indicate that the signal is centered around the reference frequency described in the first argument. Thus for the case of $a_p^{\rm in}(\omega-\omega_{\rm c}, k\omega_{\rm m})$ the signal is centered around $\omega_{\rm c}$, and contains sidebands at the second argument $k\omega_{\rm m}$.

Output Field Response: Since the sidebands lie outside the cavity linewidth, the phase of the delayed reflected signal at ω_c interferes with these sideband signals after exiting the cavity. The steady-state system dynamics can be obtained from the quantum Langevin equation, expressed in the time domain as compared to the Fourier domain one in Eq. (2.60):

$$\dot{a}(t) = -i\omega_0(t)a(t) - \frac{\kappa_\mathrm{tot}}{2}a(t) - i\sqrt{\kappa_\mathrm{ext}}a_p^\mathrm{in}(t), \tag{4.4}$$

where $a(t)$ is the cavity annihilation operator, and $\kappa_\mathrm{tot} = \kappa_\mathrm{int} + \kappa_\mathrm{ext}$ is the total damping rate, with κ_int and κ_ext the internal and external damping rates, respectively. Assuming $\delta b_\mathrm{int}(t) \ll b_0$, the fluctuating resonance $\omega_0(t) = \omega_\mathrm{c} + \delta\omega_0(t)$ takes the form

$$\omega_0(t) = \omega_\mathrm{c} + g_b \delta b_\mathrm{int}(t), \tag{4.5}$$

where we define g_b as the coupling coefficient to the bias parameter b: $g_b = (d\omega_0/db)|_{b=b_0}$. Using the transformation $\tilde{a}(t) = a(t)\, e^{i\delta\omega_0 t}$ [104] corresponding to the rotating frame defined by the fluctuations $\delta b_\mathrm{int}(t)$, and the solution ansatz $\tilde{a}(t) = \tilde{\alpha}(t)\exp[-i\omega_\mathrm{c}t - \kappa_\mathrm{tot}t/2]$, we obtain for $\langle a(t)\rangle$:

$$\langle a(t)\rangle = -i\sqrt{\frac{P_p^\mathrm{in}\kappa_\mathrm{ext}}{\hbar\omega_\mathrm{c}}} \sum_{k=-\infty}^{k=\infty} \frac{J_k(\beta)e^{-i(\omega_\mathrm{c}+k\omega_\mathrm{m})t}}{i[\delta\omega_0(t) - k\omega_\mathrm{m}] + \kappa_\mathrm{tot}/2}, \tag{4.6}$$

where we neglect the contributions from the term containing $d\delta\omega_0/dt$ as $(d\delta\omega_0/dt)\Delta t \ll \delta\omega_0(t)$ assuming a nanosecond time scale for Δt (corresponding to the shortest time scale given by inverse of the cavity resonant frequency), compared to slowly changing fluctuations in resonance. Next, we obtain the output field $\langle a_p^\mathrm{out}(t)\rangle$ using the input-output relation $a_p^\mathrm{out}(t) = a_p^\mathrm{in}(t) - \sqrt{\kappa_\mathrm{ext}}a(t)$ [see Eq. (2.67)]:

$$\langle a_p^\mathrm{out}(t)\rangle = \sqrt{\frac{P_p^\mathrm{in}}{\hbar\omega_\mathrm{c}}} \sum_{k=-\infty}^{k=\infty} r_k(t)J_k(\beta)e^{-i(\omega_c+k\omega_\mathrm{m})t}, \tag{4.7}$$

where $r_k(t)$ can be written as,

$$r_k(t) = \frac{k\omega_m - \delta\omega_0(t) + i(\kappa_\mathrm{int} - \kappa_\mathrm{ext})/2}{k\omega_m - \delta\omega_0(t) + i(\kappa_\mathrm{int} + \kappa_\mathrm{ext})/2}. \tag{4.8}$$

Notice that $r_k(t)$ takes the general form of a reflection-coefficient at $\omega_c + k\omega_\mathrm{m}$, but is slowly time-varying due to the low-frequency fluctuations in the cavity resonance itself. Typical measurements of cavity reflection coefficients using a vector network analyzer output the value averaged over the measurement time, and often smear out the effects of these resonant fluctuations [101, 100].

The output power can be obtained using $\langle P_p^{\mathrm{out}}(t)\rangle = \langle V_p^{\mathrm{out}}(t)\rangle^2/Z_p$, where Z_p is the transmission line impedance and $V_p^{\mathrm{out}}(t)$ is the output voltage given by the following [as can be obtained using Eqs. (2.53) and (2.50)]:

$$V_p^{\mathrm{out}}(t) = -i\int_0^{\infty} d\omega \sqrt{\frac{\hbar\omega}{4\pi Z_p}}\,\left[e^{-i\omega t}a_p^{\mathrm{out}}(\omega) - e^{i\omega t}\left(a_p^{\mathrm{out}}(\omega)\right)^{\dagger}\right]. \tag{4.9}$$

Note that the output power spectral components have an implicit dependence on time due to the low-frequency fluctuations $\delta b_{\mathrm{int}}(t)$ of the bias parameter.

Power Detection: Furthermore, detection of $\langle P_p^{\mathrm{out}}(t)\rangle$ will result in an oscillating signal with frequencies $k\omega_{\mathrm{m}}$. The DC component of this signal gives the reflected intensity, and has its minimum at $\delta\omega_0 = 0$, with a symmetric response about this point. As already discussed in §4.1.1, we are interested in measuring the contribution oscillating at ω_{m}, which can be obtained as

$$\begin{aligned}\mathcal{P}(t) =& J_0(\beta)J_1(\beta)P_p^{\mathrm{in}} \\ &\left[e^{i\omega_m t}\left(r_0(t)r_1^*(t) - r_0^*(t)r_{-1}(t)\right) + e^{-i\omega_m t}\left(r_0^*(t)r_1(t) - r_0(t)r_{-1}^*(t)\right)\right],\end{aligned} \tag{4.10}$$

where we have neglected the contribution from the second harmonics and above assuming smallness of $J_k(\beta)$ for $k > 1$.

The above expression represents the first derivative of the reflected intensity encoded in the first sideband ω_{m}, which will behave as a monotonically increasing function with its zero at $\delta\omega_0 = 0$. Thus, as long as $(d\omega_0/db)$ varies monotonically as a function of b, we can utilize this information as a potential error signal to counteract the fluctuations $\delta b_{\mathrm{int}}(t)$. In Fig. 4.3, the output signal is denoted by $a_p^{\mathrm{out}}(\omega - \omega_{\mathrm{c}}, k\omega_{\mathrm{m}}, \delta b_{\mathrm{int}})$, indicating that the signal is centered about ω_{c}, has sidebands at $k\omega_{\mathrm{m}}$, and contains information about the intrinsic bias noise. Similarly, the $\mathcal{P}(\omega - k\omega_{\mathrm{m}}, \delta b_{\mathrm{int}})$ term in Fig. 4.3 indicates that the signal has frequencies at $k\omega_{\mathrm{m}}$.

Extraction of the Error Signal: To maximize the sensitivity in detecting the fluctuations $\delta\omega_0(t)$, we utilize the sine quadrature of expression (4.10). We achieve this experimentally using a lock-in amplifier with the reference signal taken from the original modulation source. Quantitatively, the in-phase cosine quadrature $X(t)$ is insensitive to these resonant fluctuations while the sine quadrature $Y(t)$ is given by [comparable to Eq. (2.53)]

$$\begin{aligned}Y(t) = {} & 2J_0(\beta)J_1(\beta)P_p^{\text{in}} \\ & \Big(\text{Im}[r_0(t)]\big(\text{Re}[r_1(t)] + \text{Re}[r_{-1}(t)]\big) - \text{Re}[r_0(t)]\big(\text{Im}[r_1(t)] + \text{Im}[r_{-1}(t)]\big)\Big).\end{aligned} \tag{4.11}$$

For ω_m well outside the cavity line-width, $\text{Im}[r_{\pm1}(t)] \to 0$ and $\text{Re}[r_{\pm1}] \to 1$ for cavity resonances $\omega_0(b)$ in the vicinity of ω_c. In short,

$$Y(t) = 16\kappa_\text{ext}J_0(\beta)J_1(\beta)P_p^{\text{in}}\,\frac{g_b\delta b_\text{int}(t)}{\kappa_\text{tot}^2 + 4g_b^2\delta b_\text{int}(t)^2}. \tag{4.12}$$

The above expression captures the fluctuations δb_int accurately in the limit $2g_b\delta b_\text{int}(t) \ll \kappa_\text{tot}$. In the regime $2g_b\delta b_\text{int}(t) > \kappa_\text{tot}$, the function starts falling towards zero. The bandwidth where the function monotonicity switches is obtained using the condition

$$\left.\frac{d\,\text{Im}[r_0]}{d\delta\omega_0}\right|_{\omega_0=\omega_{bw}} = 0, \tag{4.13}$$

to give $\omega_{bw} = \kappa_\text{tot}$.

Lock-in Amplifier Characteristics: The normalized transfer function of the lock-in amplifier is that of a single-pole, low-pass filter. In other words, the dynamics of the lock-in amplifier can be modeled as a lumped-element RC low-pass filter via the expression [80]

$$\dot{y}(t) = -\frac{1}{RC}y(t) + \frac{1}{RC}u(t), \tag{4.14}$$

where $u(t)$ and $y(t)$ are the input and output voltages, respectively. In the Fourier domain, this expression becomes

$$\omega y(\omega) = -\frac{1}{RC}y(\omega) + \frac{1}{RC}u(\omega), \tag{4.15}$$

such that the transfer function $G_\text{LA}(\omega) \equiv y(\omega)/u(\omega) = (1+i\omega\tau_\text{LA})^{-1}$, where $\tau_\text{LA} = RC$ is the lock-in amplifier time-constant. As mentioned above, the transfer function has a single pole in the complex plane given by $\omega = -1/\tau_\text{LA}$.

Net transfer function: In the region where the approximation $\delta b_\text{int} \ll \kappa_\text{tot}/2g_b$ is valid, the net transfer function of the open-loop setup can be written as

$$G(\omega) = \frac{Y(\omega)}{\delta b_\text{int}(\omega)} = \frac{G_0}{1 + i\omega\tau_\text{LA}}, \tag{4.16}$$

where G_0 is the net gain,

$$G_0 = \left(\frac{4J_1(\beta)}{J_0(\beta)} \right) n\hbar\omega_0(b_0) g_b G_{\text{amp}}, \tag{4.17}$$

and we have expressed the input power in terms of $n = 4\kappa_{\text{ext}} J_0^2(\beta) P_p^{\text{in}} / \hbar\omega_0(b_0)\kappa_{\text{tot}}^2$, the average number of photons in the cavity. Here, G_{amp} is the net gain of the amplifier chain, including that of the power detector and the lock-in amplifier. Note that we have neglected the secondary fluctuations of n and ω_0 in the above expression, induced due to the bias fluctuations. Also, we withhold commenting on the dimensions of $G(\omega)$ (which is typically dimensionless) as we have considered δb_{int} as a generalized, fluctuating variable to begin with.

Moreover, the PSD of fluctuations in $Y(t)$ takes the form

$$S_{YY}(\omega) = \left(\frac{G_0^2}{1 + \omega^2 \tau_{\text{LA}}^2} \right) S_{bb}(\omega), \tag{4.18}$$

where $S_{bb}(\omega)$ is the PSD of the bias noise.

Feedback Characteristics: We can now close the feedback loop in our setup by applying a control law that effectively counteracts for δb_{int}. For a beginner's overview for understanding the concepts in feedback dynamics, the review article by Bechhoefer [80] is a good starter-reference. Following [80], we may reduce the closed loop dynamics to a block diagram form as given in Fig 4.4.

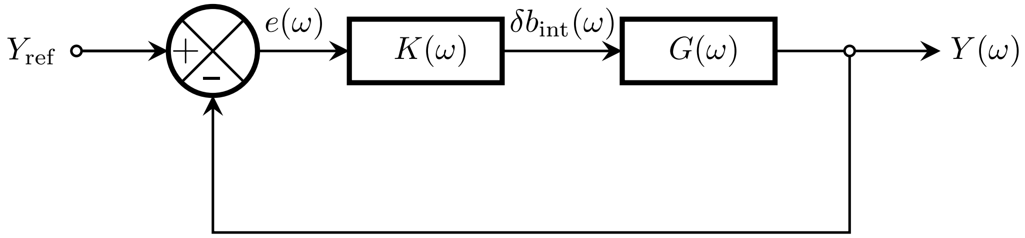

Figure 4.4: Reduced block diagram illustrating the closed-loop control of the fluctuations in a tunable cavity.

In the above figure, the fluctuations δb_{int} is detected by the lock-in amplifier using a net transfer function $G(\omega)$ as derived in Eq. (4.16), which outputs the sine quadrature $Y(\omega)$. The error signal $e(\omega)$ is obtained with reference to the desired control signal $Y_{\text{ref}} = Y(t_0)$ such that $e(\omega) = Y(\omega) - Y_{\text{ref}}$. For cavities with linear reflection coefficients discussed above, note that this control value Y_{ref} is zero for any time t, as can be determined from Eq. (4.11).

We can now apply a control law $K(\omega)$ through a PID controller, such that $Y(t)$ follows the control signal $Y_{\text{ref}} = Y(t_0)$ as closely as possible. Interpreting the diagram, we get the closed loop transfer function as

$$Y(\omega) = K(\omega)G(\omega)e(\omega) = \frac{L(\omega)}{1 + L(\omega)} Y_{\text{ref}}, \tag{4.19}$$

with the loop gain $L(\omega) \equiv K(\omega)G(\omega)$. Hence under the condition of $K(\omega)G(\omega) \gg 1$, $Y(\omega) \to Y_{\text{ref}}$. It may occur to the reader that using high values for $K(\omega)$ might be an efficient way to operate the feedback loop. However, increasing $K(\omega)$ also results in the amplification of the added noise by the amplifier chain. As discussed in more detail in §4.3, balancing these two factors, i.e., fixing $K(\omega)G(\omega) \gg 1$ and $K(\omega)$ such that the loop does not pick up substantial sensor noise [80], turns out to be one major challenge of our setup in the single-photon limit. Once these conditions are met, we can however compensate for the fluctuations $\delta b_{\text{int}}(\omega)$ up to a bandwidth of $1/\tau_{\text{LA}}$.

4.2.2. Application to the cCPT

The scenario discussed in the previous section is frequently observed in many open quantum systems, where the tunability control of the system of interest introduces noise and results in reduced measurement sensitivity or in some cases, decreased coherence properties [40, 105, 106]. In this section we discuss the implementation of the scheme presented in Sec. 4.2 in one such system, the cCPT.

Similar to the system described in Fig. 4.3, the cCPT communicates with the external pump/probe setup through its quarter-wave superconducting microwave resonator. The non-linear Josephson inductance emerging from the Cooper pair transistor introduces two-dimensional tunability to the resonance, either via the gate voltage V_g controlling the island charge of the Cooper pair transistor, or via the external flux bias Φ_{ext}, coupling the cavity phase and the differential phase of the Josephson junctions via a SQUID loop; the current work mainly focuses on the suppression of the resonant frequency fluctuations caused due to charge noise coupling to the cavity at low frequencies. The resulting reduction of the $1/f$-noise, as detailed in Sec. 4.4, is significant enough to potentially allow the cCPT to operate in an ultra-sensitive regime for electrometry.

Operational Bias Regimes: Following the formalism in Sec. 4.2, we now have the bias vector $\vec{b} = (n_g, \Phi_{\text{ext}})$ and the resonant frequency shift $\delta\omega_0(\vec{b})$ inversely

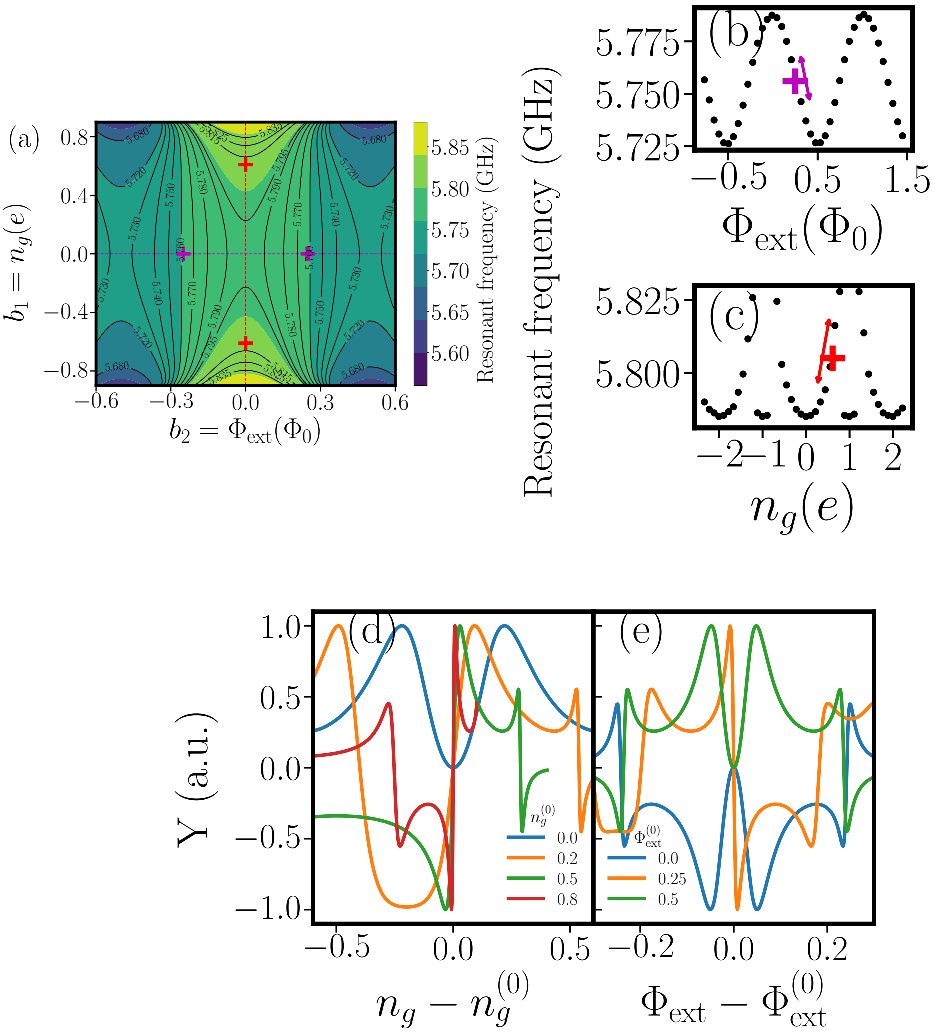

Figure 4.5: (a) Contour plot displaying the resonant frequency ω_0 as a function of the two-dimensional bias space. We avoid feedback locking in regions where the cavity is sensitive to both bias parameters simultaneously, so as to avoid accidentally destabilizing the cavity away from the bias point of interest. (b) Measured resonant response as a function of flux along $n_g = 0$ (purple line in (a)), where the charge noise is minimal. The purple plus sign denotes point of maximum flux sensitivity. (c) Measured resonant response as a function of gate along $\Phi_{\text{ext}} = 0$, where the flux sensitivity is minimal (red line in (a)). The charge sensitivity increases towards charge degeneracy ($n_g = 1$), but we avoid operating the feedback loop in the region $|n_g| > 0.65$ because of quasiparticle poisoning. The red plus sign denotes a point of high gate sensitivity. (d) Simulated $\text{Y}(n_g)$ calculated about different bias values of $n_g^{(0)}$. The monotonicity for small $n_g - n_g^{(0)}$ is steeper for higher values of $n_g^{(0)}$ and non-existent at $n_g^{(0)} = 0$. (e) Simulated $\text{Y}(\Phi_{\text{ext}})$ calculated about different bias values of $\Phi_{\text{ext}}^{(0)}$. Unsuitable points of feedback operation are near $\Phi_{\text{ext}}^{(0)} = 0$ and $\Phi_{\text{ext}}^{(0)} = 0.5\Phi_0$.

proportional to the Josephson inductance L_{CPT} given by [see Eq. (3.41)]

$$L_{\mathrm{CPT}}^{-1} = \frac{\partial^2 E_{\mathrm{CPT}}^{(0)}}{\partial b_2^2}, \tag{4.20}$$

where $E_{\mathrm{CPT}}^{(0)}$ is the ground state energy of the CPT described by the Hamiltonian with matrix coefficients [see Eq. (3.30) considering junction symmetry]

$$\langle N|H_{\mathrm{CPT}}|N\rangle = 4E_c \left(N - \frac{b_1}{2}\right)^2, \tag{4.21}$$

and

$$\langle N|H_{\mathrm{CPT}}|N+1\rangle = \langle N|H_{\mathrm{CPT}}|N-1\rangle = E_J(b_2), \tag{4.22}$$

where E_c and $E_J(b_2 = \Phi_{\mathrm{ext}})$ are the charging and the Josephson energies of the CPT, respectively. The ket $|N\rangle$ denotes the number of excess Cooper pairs on the CPT island and the gate polarization number $b_1 = n_g$ is related to the externally applied gate voltage V_g via $n_g = C_g V_g / e$.

Fig. 4.5(a) provides a simulated 2-D contour plot of the tunable resonant frequency based on the experimental characterization of the cCPT. As can be seen in this contour plot, a single value of ω_0 can correspond to a continuum of possible values in the bias space. The feedback scheme corrects for the bias fluctuations purely based on the detuning of the carrier signal from the resonance. As a result, applying the technique to a simultaneous charge and flux sensitive region can result in increased instability in the applied bias along a contour while still stabilizing the resonant frequency fluctuations. We therefore limit our measurements (presented in later sections) to the regimes where the cCPT is sensitive to one of the bias parameters while minimizing the coupling to the other ones.

Figs. 4.5(b) and 4.5(c) provide the measured frequency response around these bias-sensitive regimes. Fig. 4.5(b) plots $\omega_0(b_2)$ while $b_1 = 0$ such that the gate is effectively decoupled from the cavity. Similarly, Fig. 4.5(c) plots $\omega_0(b_1)$ while b_2 is set to zero, i.e., with minimal flux noise. Notice that for $0.1 \leq |n_g| \leq 0.65$, n_g corresponds to frequency shifts that are monotonic on the order of tens of MHz - several times larger than the typical cavity linewidths. Thus our feedback scheme can be applied across an appreciable span along n_g. The region $|n_g| > 0.65$ is highly prone to quasi-particle poisoning, and we avoid operation in this regime, as discussed later in Sec. 4.4. The simulated $Y(b)$ response is plotted in Figs. 4.5(d) and 4.5(e).

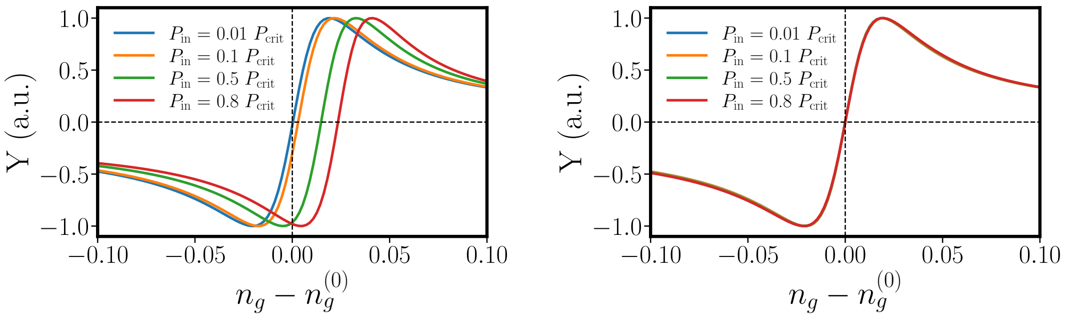

(a) (b)

Figure 4.6: (a) Error signal simulated at $(n_g, \Phi_{\rm ext}) = (0.6, 0)$ for different input powers driving the cCPT and the carrier frequency fixed at $\omega_{\rm c} = \omega_0(b_0) = 5.81$ GHz. The input power is expressed in the units of the critical input power $P_{\rm crit}$, defined at the onset of bistability. The Kerr coefficient $K = -0.67$ MHz. The control value of $Y_{\rm ref}(b_0)$ deviates from zero in this case. For higher input powers, we no longer have a one-to-one mapping between the gate fluctuation and Y. (b) Corresponding plots for $\omega_{\rm c} = \omega_0(b_0) + nK$ that effectively resolve the issues in (a).

As expected, near $n_g^{(0)} = 0$, $Y(n_g)$ is symmetric and does not have a one-to-one mapping onto its respective bias value making this the regime unsuitable for the feedback application. Similar conclusions about feedback applicability in flux noise suppression can be deduced from Fig. 4.5(e).

Limitations due to Kerr Nonlinearity: The results reported in this work also involve driving the cavity to Kerr-shifted regimes. The resulting non-linear reflection coefficient takes the form of Eq. (4.8) with $\delta\omega_0 \to \delta\omega_0 + Kn(\delta\omega_0)$, where K is the Kerr-coefficient and $n(\delta\omega_0)$ is the average number of photons in the cavity given by the roots of the following equation [14]:

$$n^3K^2 + 2\delta\omega_0 K n^2 + [\delta\omega_0^2 + \kappa_{\rm tot}^2/4]n - \kappa_{\rm ext}P_{\rm in}/\hbar\omega_0 = 0. \tag{4.23}$$

As the Kerr-coefficient can be strong enough to produce a Kerr-shift comparable to the cavity linewidth of the cCPT for $n \geq 5$, it is important to look at its effects on the error signal generation. The simulations illustrating these effects are compiled in Fig. 4.6, for input powers less than the critical input power $P_{\rm crit}$, defined at the onset of bistability. Depending on the specific application of interest, we may require driving the cavity exactly at linear resonance with $\omega_{\rm c} = \omega_0(b_0)$. The reference signal $Y_{\rm ref}(b_0)$ in this case corresponds to a non-zero value (as illustrated in Fig. 4.6a), and the Kerr-induced asymmetries in $r_n(t)$ can be strong enough for the error signal to deviate from the preferred, smooth, monotonic behavior about the resonance (as can be seen for $P_{\mathrm{in}} = 0.8P_{\mathrm{crit}}$ in Fig. 4.6a). The former merely requires a recalibration of $Y_{\mathrm{ref}}(b_0)$ at each bias point. However, the latter effectively acts as an upper bound in limiting the application of the feedback technique at higher input powers. This limitation can be circumvented by fixing the carrier signal at the point of minimum reflection coefficient, given by $\omega_{\mathrm{c}} = \omega_0(b_0) + nK$. The feedback scheme can then be applied for input powers $P_{\mathrm{in}} < P_{\mathrm{crit}}$ such that the reference control Y_{ref} remains at zero (see Fig. 4.6b).

Section 4.3

Experimental Setup

We present in this section the experimental realization of the scheme discussed in the previous sections. The underlying circuitry behind the detection of the error signal is similar to the Pound-Drever-Hall technique applied to superconducting microwave resonators [67]. In contrast to the conventional technique, which corrects the drive frequency, we use the PID output to change the bias parameter, thereby stabilizing the resonant frequency of the cavity itself. The circuitry enabling such a measurement is shown in Fig. 4.7, and is detailed in the following.

4.3.1. Circuitry

The input drive consists of a carrier signal ω_{c} at the cavity resonance frequency, which is phase-modulated (using an Analog Devices HMC-C010 phase-shifter) at a frequency ω_{m}. The reflected output signal is amplified at different stages and is sent into a directional coupler where the signal is to split into two routes: the feedback loop component A and the actual measurement component B. The -20 dB coupled port sends signal B to a spectrum analyzer, which can be used to track the power spectral components when the feedback loop is active. Signal A enters a highly sensitive power detector (SDLVA HMC-C088), which outputs a voltage proportional to the input power, with frequency components at the harmonics of ω_{m}. The lock-in amplifier then mixes this signal with the reference signal at ω_{m} to output the two quadrature components. The error signal of interest is contained in the Y-quadrature such that a fluctuation of the cavity resonance frequency is typically measured as a non-zero value [see Fig. 4.11(b)]. When the cCPT is biased at points where flux/charge

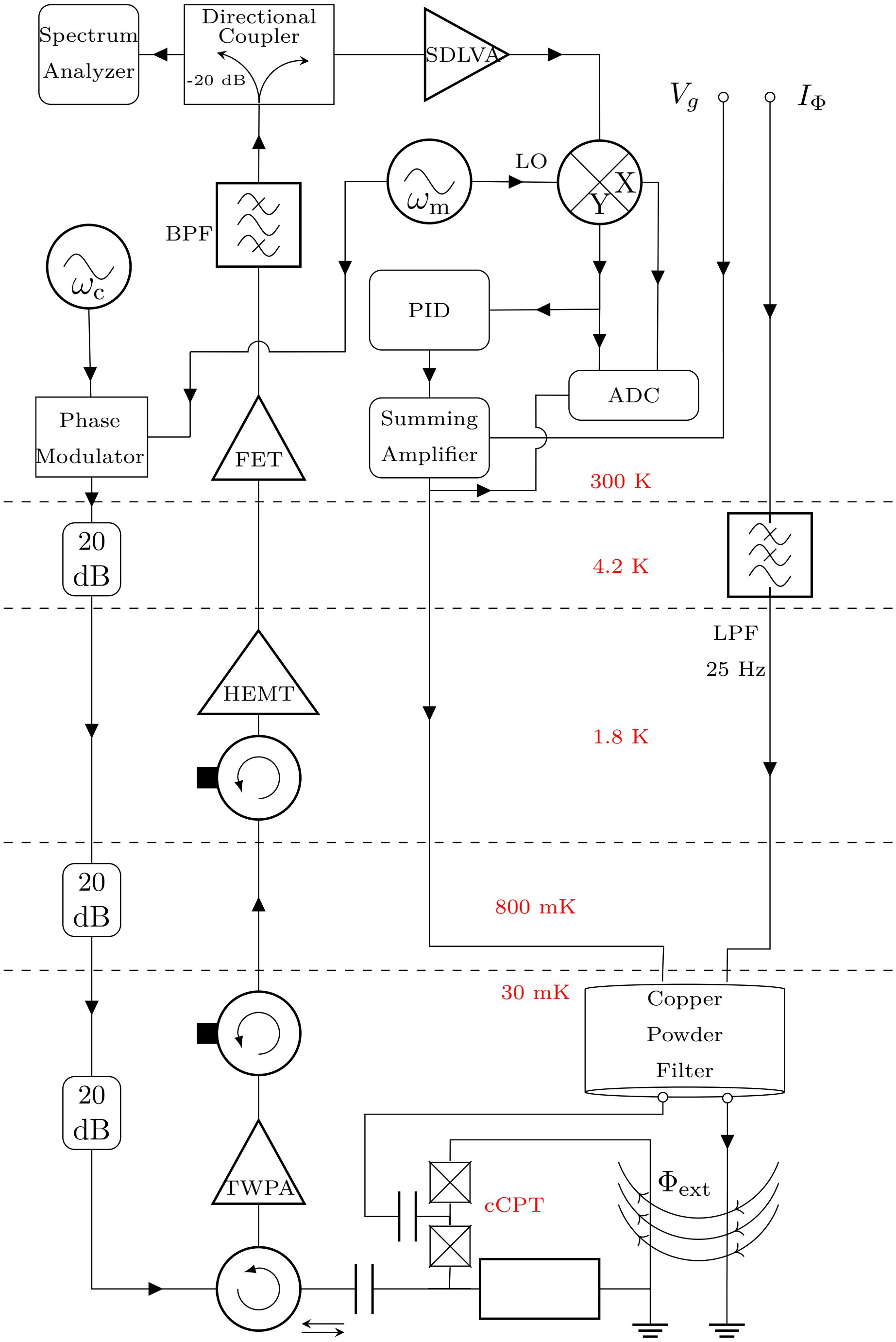

Figure 4.7: Experimental setup for the dynamic feedback control of the intrinsic bias noise coupling to the cavity.

causes the dominant source of intrinsic noise, we attribute these measured resonance frequency fluctuations to disturbances in that bias parameter. The output of the PID controller then corrects the error in the bias parameter (gate voltage in our case) via a summing amplifier. The summing amplifier is bandwidth-limited to 1 MHz. This reduces high-frequency noise, while allowing modulations for charge-sensitivity measurements up to a few 100 kHz. Note that an important modification from the experimental characterization setup at the cryogenic stage (see Fig. 3.7) is removal of the bias tee in the gate line, which otherwise limits the transfer function at ∼1 kHz disabling PID integration with the original gate signal at a faster rate.

The cCPT used for the following measurements is the same sample discussed in §3.3.3, and exhibits a total tunability of about 140 MHz, centered about the bare cavity frequency at 5.757 GHz. Following a model that accounts for frequency fluctuations in the cavity [101], the typical external and internal damping rates observed at $(n_g, \Phi_{\text{ext}}) = (0, 0)$ are ∼0.97 MHz and ∼0.3 MHz, respectively. We therefore fix the modulation frequency ω_{m} to be 30 MHz, one order of magnitude higher than the total damping rate.

4.3.2. Benchmarking

Since the measurements are performed in the few-photon limit, we have optimized our setup at each stage to attain the maximum signal-to-noise ratio (SNR) at the output. Firstly, as the magnitude of the error signal is proportional to $J_1(\beta)/J_0(\beta)$ [refer Eq. (4.17)] for a fixed average photon number in the cavity, we choose $\beta = 1.84$ to provide increased sensitivity. This value is chosen such that $J_1(\beta)$ is maximized, and $J_0(\beta)$ is not too low a coefficient to achieve cavity driving.

The circuitry is further refined to ensure the error signal behaves in a manner discussed in Sec. 4.2. For example, choosing higher values of β implies deviation from our theoretical model as discussed in Eq. (4.10) where we have assumed smallness of β. By increasing β, the error signal Eq. (4.11) can also have increased contributions from the cross-terms involving sidebands at $\pm\omega_m$ and $\pm 2\omega_m$. A tunable bandpass filter with center frequency near resonance and bandwidth less than $4\omega_m$ is inserted after the room temperature amplifiers to partially filter out these extra signals. This prevents unwanted noise in the DC, ω_m and $2\omega_m$ components, reducing the saturation of the power detector and ensuring a larger SNR at the power detector output by reducing the input noise [103].

Figure 4.8a plots the response of the phase modulated signal to varying values of

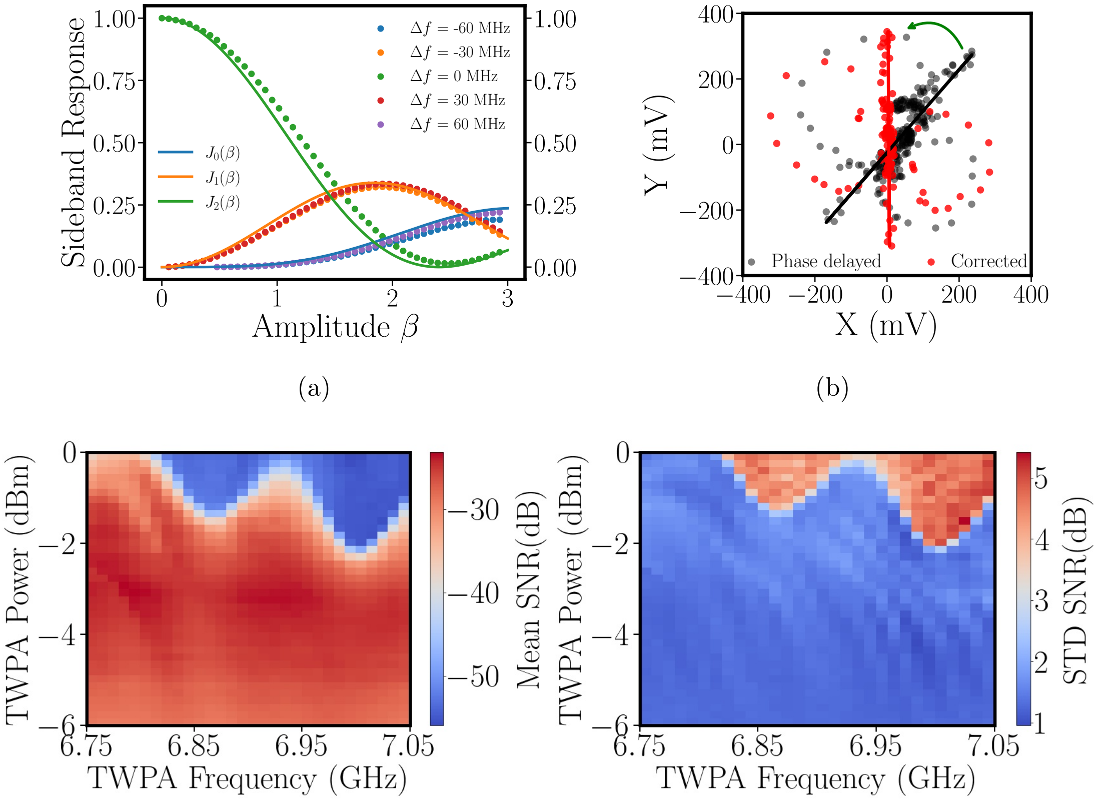

(a) (b)

(c) (d)

Figure 4.8: Initial calibration before the measurements. (a) Phase modulator is calibrated to ensure a reliable control on the number of photons driving the cavity. The sideband peaks are measured for each control voltage of the phase shifter and Bessel function dependence is extracted from this data. (b) Quadrature outputs from the lock-in amplifier displayed as a parametric plot. The data is measured for varying ω_c, with resonance fixed at $\omega_0(0,0)$, where both the flux and charge noise is a minimum for the cCPT, and the cavity is driven at photon number $n = 1$. The black plot represents the data before the phase delay correction. All the feedback measurements are carried out with the phase of the reference signal set to the one in the red plot. This ensures that the error signal has maximum sensitivity to fluctuations. (c) Visualization of TWPA's response to control bias parameters, i.e., the drive frequency and drive power. For this measurement, the gain profile and the noise floor are measured using a VNA, and a spectrum analyzer, respectively. The SNR is calculated corresponding to frequencies in the cCPT's tunable range (5.68-5.82 GHz) and a noise bandwidth of 80 MHz (that of the tunable bandpass filter). (d) Mean standard deviation for the frequency range in (c) to quantify ripples in the profile.

modulation amplitude β. This is an important calibration step that accurately sets the value of β, and therefore ensures a known number of photons driving the cavity, as detailed further below. The phase-shifter is calibrated by measuring the response of the sidebands to varying control voltages, and later fitting these curves to Bessel functions $J_n(\beta)$.

A near quantum-limited traveling wave parametric amplifier (TWPA) [107] at the first-stage amplification improves the real-time detection of the resonant frequency fluctuations at the single-photon level. For the efficient detection of the phase-modulated signal by the power detector, the bias power and frequency of the TWPA pump are chosen such that the mean SNR across the cCPT's tunable range is maximum, corresponding to a noise bandwidth of 80 MHz (equal to that of the tunable bandpass filter), and a signal of one photon. The gain profile also displays minimal ripples at these bias values to achieve relatively symmetric response at either of the sidebands. This ensures the error signal response is not influenced by the gain profile features, and the cavity response is closely tracked. The results plotting the mean and standard deviation of the SNR across the TWPA's bias parameters are plotted in Figs. 4.8c and 4.8d, respectively.

Since the output signal reflected from the cavity goes through several meters of cable and other microwave components as compared to the reference signal used by lock-in amplifier, the sine quadrature output is typically phase-shifted to a different quadrature. We correct for this phase delay using a frequency sweep of the carrier signal and simultaneous measurement of both quadratures, with the cCPT biased at the minimally flux and gate sensitive point $(n_g, \Phi_{\text{ext}}) = (0, 0)$. Figure 4.1c illustrates the quadrature response when the power detector output is mixed to the reference frequency without a delay. As shown in Fig. 4.8b, a phase delay causes a rotation in the phase space, and can be corrected for accordingly.

4.3.3. Charge and Flux Noise in the cCPT

Prior to conducting closed loop measurements to stabilize the resonant frequency of the cCPT, we first ensure the open loop configuration detects the intrinsic charge or flux noise with reliable accuracy. In short, such a measurement involves biasing the cCPT at a point sensitive to the particular noise (charge or flux) we are interested in, while simultaneously protecting the cCPT from coupling to the other noise source, by biasing it in a regime insensitive to the latter source.

The measurement is preceded by a series of calibration steps to ensure the cCPT

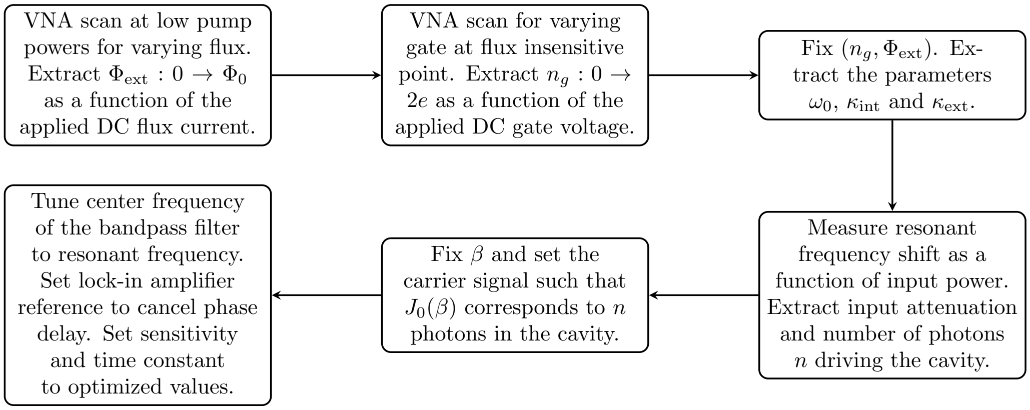

VNA scan at low pump powers for varying flux. Extract $\Phi_{\text{ext}} : 0 \rightarrow \Phi_0$ as a function of the applied DC flux current.

VNA scan for varying gate at flux insensitive point. Extract $n_g : 0 \rightarrow 2e$ as a function of the applied DC gate voltage.

Fix (n_g, Φ_{ext}). Extract the parameters ω_0, κ_{int} and κ_{ext}.

Measure resonant frequency shift as a function of input power. Extract input attenuation and number of photons n driving the cavity.

Fix β and set the carrier signal such that $J_0(\beta)$ corresponds to n photons in the cavity.

Tune center frequency of the bandpass filter to resonant frequency. Set lock-in amplifier reference to cancel phase delay. Set sensitivity and time constant to optimized values.

Figure 4.9: Flow chart for the calibration code that is run before the start of an actual measurement.

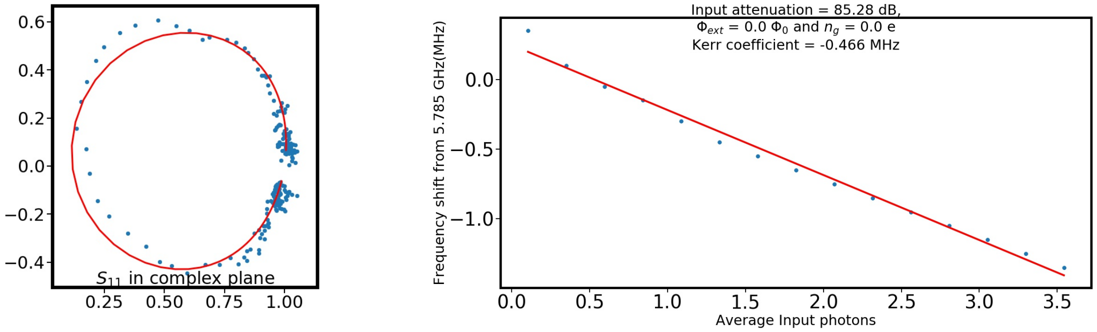

(a) (b)

Figure 4.10: (a) Resonant features of the cCPT at $(n_g, \Phi_{\text{ext}}) = (0.4, 0)$, analyzed using a model that tracks the frequency fluctuations caused due to charge noise [101]. The obtained values are $\omega_0 = 5.79$ GHz, $\kappa_{\text{int}} = 0.55$ MHz and $\kappa_{\text{ext}} = 0.98$ MHz. (b) Linear dependence of the resonance shift on the input power can be used to extract the number of photons n driving the cCPT at the sample [14].

is biased at the right (n_g, Φ_{ext}) and is driven at a known number of photons n in the cavity. These steps are compiled in Fig. 4.9. The resonance parameters such as ω_0, κ_{int} and κ_{ext} are extracted using the frequency fluctuations model reported by Brock *et al.* [101] [see Fig. 4.10a]. The average photon numbers driving the cavity are calculated employing a model that considers the linear relation between the input power at the sample and the associated Kerr-shift in the cavity resonance frequency [14] [see Fig. 4.10b].

Fig. 4.11(a) constitutes an accurate representation of the sine quadrature as a function of carrier signal around resonance, after accounting for the phase delay correction, and for varying average photon number in the cavity. As can be seen, the zero-point of the error signal remains at the Kerr-shifted resonance value, allowing us to set the reference value for the feedback signal at zero, even when the cavity is driven into the Kerr-regime.

The fluctuations in $Y(t)$ as measured by the digitizer, given by $S_{YY}(\omega)$, for the open-loop setup when the cavity is driven at $n = 10$ is provided in Fig. 4.11(b). The PSD of the time-domain data collected over 10 sec at 100 kHz sampling rate is plotted in this figure. The data is scaled to the amplitude of the noise floor to clearly display the signal-to-noise ratio (SNR) of the measurement. The off-resonance noise measurement of the Y-quadrature of the lock-in amplifier outputs a single-pole, low-pass filter transfer function given by $G(\omega) = (1 + i\omega/\omega_{\text{LPF}})^{-1}$, where $\omega_{\text{LPF}} = 2\pi\times$ 1331 Hz, close to the lock-in amplifier bandwidth set by the time constant 100 μsec. The time constant is set to measure a reasonable bandwidth of low-frequency fluctuations; a higher bandwidth detects more fluctuations but it necessitates an associated decrease in the measurement time, negatively affecting the SNR simultaneously.

In order to calculate the PSD of the intrinsic charge noise $S_{qq}^{\text{int}}(\omega)$, we first obtain the DC gain $G_0 = G(\omega)|_{\omega=0}$. This is calculated from the slope of $\bar{Y}(|\delta n_g| \leq 0.01)$, where $\bar{Y}(|\delta n_g|)$ corresponds to the time-averaged value of $Y(|\delta n_g|)$ in the vicinity of our bias point of interest, which for the case discussed in Fig. 4.11(c) is at $n_g = 0.6$. After accounting for the noise floor, we may utilize Eq. (4.18) to obtain the measured charge noise $S_{qq}^{\text{meas}}(\omega)$.

As described in Fig. 4.5(c), the cCPT is susceptible to quasiparticle poisoning (QP) for n_g closer to charge degeneracy. The effects of QP poisoning appear as random telegraph noise in the data and can be modeled as a Lorentzian [14]. We thus employ a combined model including a Lorentzian and a power law fit to describe the measured apparent charge noise $\tilde{S}_{qq}^{\text{meas}}(\omega) = S_{\text{QP}} + S_{qq}^{\text{int}}$. However, the roll-off frequency for the Lorentzian fit is not resolvable using this measurement, as the bandwidth of the fit is limited by the lock-in roll-off frequency 1331 Hz. Moreover, the accuracy decreases for frequencies > 200 Hz where the SNR ~ 1. Hence, the noise floor due to QP appears to be white noise rather than Lorentzian. As the contributions to this offset-noise were observed to decrease for lower n_g values where the effects of quasiparticles are also reduced, we believe our Lorentzian model holds validity. Note that this could potentially have been due to Kerr fluctuations as well, but Fig. 4.11b validates the effects of Kerr fluctuations are in fact minimal. Fig. 4.11(c) displays

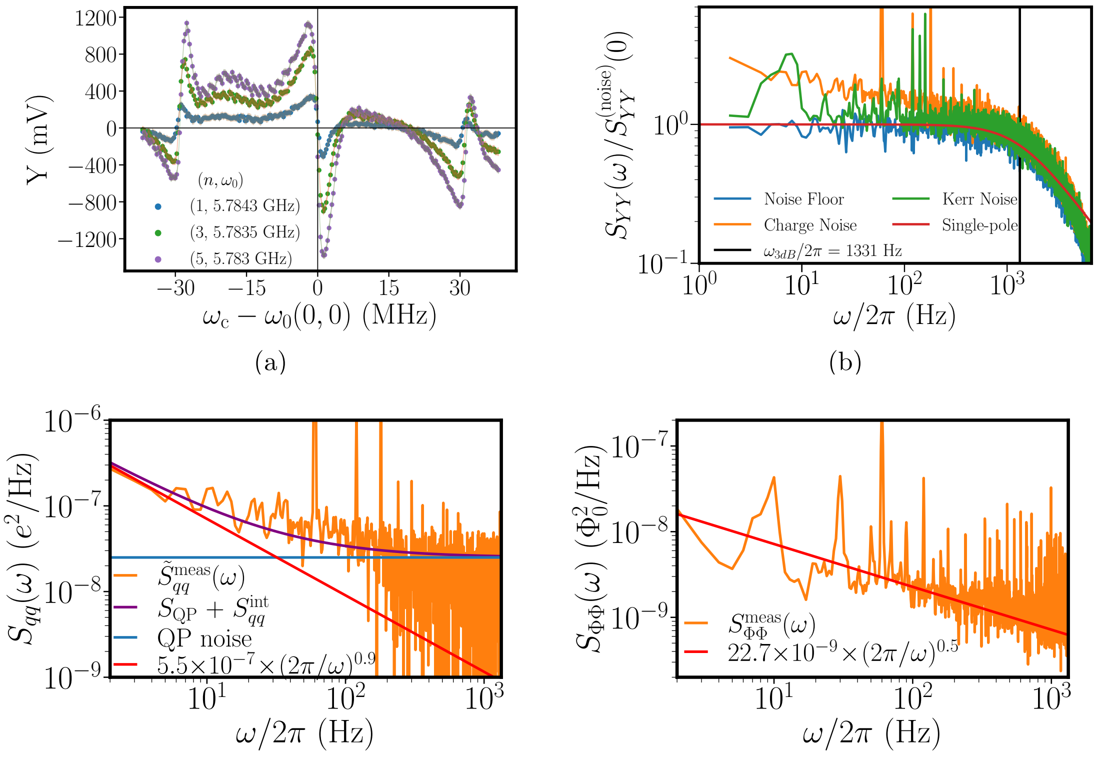

(a) (b)

(c) (d)

Figure 4.11: (a) Measured $Y(\omega_c)$ as a function of the detuning ω_c- $\omega_0(0,0)$ and varying photon number n, where $\omega_0(0,0)$ is the Kerr-shifted resonance. The zero-point of the error signal corresponds to the Kerr-shifted resonance value, enabling us to set the reference value for feedback as zero, even in strongly Kerr-nonlinear regimes. Each point is the average of a 1 sec acquisition with sampling rate of 1 kHz. The time constant of the lock-in amplifier is set to 10 ms to average out fluctuations and improve resolution. The data is taken for $\beta = 1.08$. (b) The PSD of fluctuations in $Y(t)$ given by $S_{YY}(\omega)$ for the open-loop setup. The blue plot displays the noise floor measured at the lock-in amplifier sine quadrature output. The red plot is the single-pole, low-pass filter fit applied to the above data. The cut-off frequency obtained is 1331 Hz, set by the lock-in amplifier time constant. The orange plot captures the charge fluctuations when the cCPT is biased in the increased charge-sensitive regime $(n_g, \Phi_{\mathrm{ext}}) = (0.6,\ 0)$, and the cavity is driven at $n = 10$. The green plot captures the Kerr fluctuations when the cCPT is biased at $(n_g, \Phi_{\mathrm{ext}}) = (0,\ 0)$, and $n = 10$. These measurements are completed in 10 sec with a sampling rate of 100 kHz. The data displayed in the plot is scaled to the amplitude of the noise floor to better indicate the SNR. (c) PSD of the charge noise calculated for the data in (b). $\tilde{S}_{qq}^{\mathrm{meas}}(\omega)$ is the total charge noise with contributions from the intrinsic charge noise fluctuations S_{qq}^{int} at the CPT (red plot varying as $\sim 1/f$), and the fluctuations S_{QP} due to quasiparticle switching with a Lorentzian noise floor (blue plot). Note the Lorentzian floor appears as white noise as the roll-off frequency for Lorentzian fit is not resolvable using this measurement. The purple plot corresponds to the net fit $S_{\mathrm{QP}}+S_{qq}^{\mathrm{int}}$. (d) Calculated flux noise $S_{\Phi,\Phi}(\omega)$. The data is obtained for the maximum flux sensitive point of $(n_g, \Phi_{\mathrm{ext}}) = (0,\ 0.25)$.

the calculated $S_{qq}^{\text{int}}(\omega)$ varying as

$$S_{qq}^{\text{int}}(\omega) = (5.5 \times 10^{-7}) \left(\frac{\omega}{2\pi}\right)^{-0.89} \text{e}^2/\text{Hz}. \tag{4.24}$$

The total standard deviation of charge fluctuations calculated over the bandwidth 1 Hz to $\omega_{\text{LPF}}/2\pi$ Hz is found to be 2.5 $\times 10^{-3}$ electrons. This value aligns with previously reported measurements of charge fluctuations for this device to within an order of magnitude [14], with the discrepancy in magnitude attributed to the approximations and measurement limitations of the two models. Similarly, we can also find the intrinsic flux noise of the cCPT by biasing at the flux sensitive point $(n_g, \Phi_{\text{ext}}) = (0, 0.25)$, the results of which are shown in Fig. 4.11d.

4.3.4. Feedback Control Optimization

As mentioned in Sec. 4.2, ideally we prefer $K(\omega) \gg G(\omega)^{-1}$ such that $Y(t)$ follows Y_{ref} closely. However, this is accompanied by an increase in the pick-up of the noise floor as well [80]. We may balance out the combined effects of faster noise suppression and increased sensor-noise pick-up by shaping the net loop gain. In particular, looking at the behavior of the fluctuations in Fig. 4.11(b), we can qualitatively assert that the control law can have higher magnitude at low frequencies and requires to be of lower magnitude as $\omega \to \omega_{\text{LPF}}$. Thus the net loop gain $T(\omega) \equiv L(\omega)/(1 + L(\omega))$ as derived in Eq. (4.19) in the simplest form is desired to follow a linear, single-pole function $T(\omega) = (1 + i\omega/\omega')^{-1}$, where ω' is the feedback bandwidth.

The control law can be back-calculated from the net loop gain to give

$$K(\omega) = \frac{T(\omega)}{1 - T(\omega)} G^{-1}(\omega) = \frac{\omega'}{G_0 \omega_{\text{LPF}}} \left(1 + \frac{\omega_{\text{LPF}}}{\omega}\right), \tag{4.25}$$

which takes the form of a proportional-integral control, where a control of the form $K_i \int_{-\infty}^{t} e(t')dt'$ in addition to the proportional control term $K_p e(t)$ eliminates a steady-state error that the controller measures over a set timescale. The net control law can then be expressed as

$$K(\omega) = K_p + \frac{K_i}{\omega}, \tag{4.26}$$

with $K_p = \omega'/G_0\omega_{\text{LPF}}$ and $K_i = \omega'/G_0$. We can furthermore choose ω' such that $K(\omega)G(\omega) = \omega'/\omega \gg 1$ in the region where we have an appreciable SNR [refer to Fig. 4.11(b)], but drops later as the SNR plunges.

Another potential approach to optimizing the control values involve simulations,

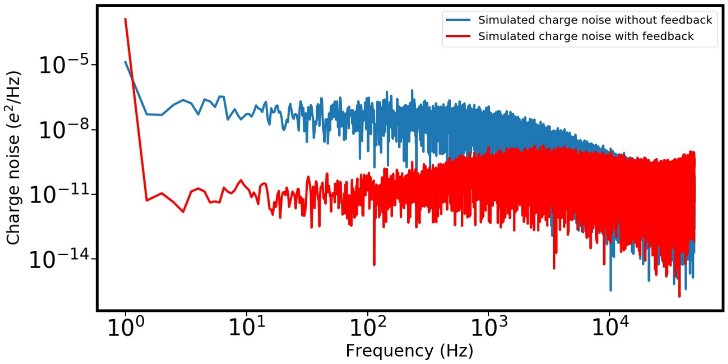

Figure 4.12: Results of the simulation illustrating a decrease in the charge noise. The program input is time-domain, open-loop data that contains information about frequency fluctuations of the cCPT. By applying a PI control to this data, the mean and standard deviation of the response is calculated, and further minimized over a set of K_p, K_i values to find the optimum control parameters.

where the simulated response of a time-domain data to proportional-integral control is optimized over a set of realizable K_p and K_i values. A preliminary illustration of this approach is plotted in Fig. 4.12 where the program outputs (K_p, K_i) values that returns minimum mean and standard deviation of the error signal across a timescale much larger than the rate of frequency fluctuations. It is to be noted that these results are demonstrative in purpose, and there is significant room for improvement in fixing the conditions of the simulation to an experimental scenario.

Finally, the setup can be further refined to accommodate a derivative control that counteracts for sudden fluctuations in the charge noise. This is especially beneficial towards our objective as the detection of resonant frequency fluctuations to the charge nosie is more second-order in nature. Since an addition of the derivative control can often negatively impact the feedback if not properly configured, we do not explore this goal in the current work as the SNR at the few-photon scale is already low to begin with.

Section 4.4

Results

The feedback correction for the charge noise is measured via the simultaneous detection of $Y(t)$ and the input gate correction, by means of a digitizer. Figures 4.13(a) and 4.13(b) provide proof of concept for our scheme. Both $Y(t)$ [refer to 4.13(a)] and

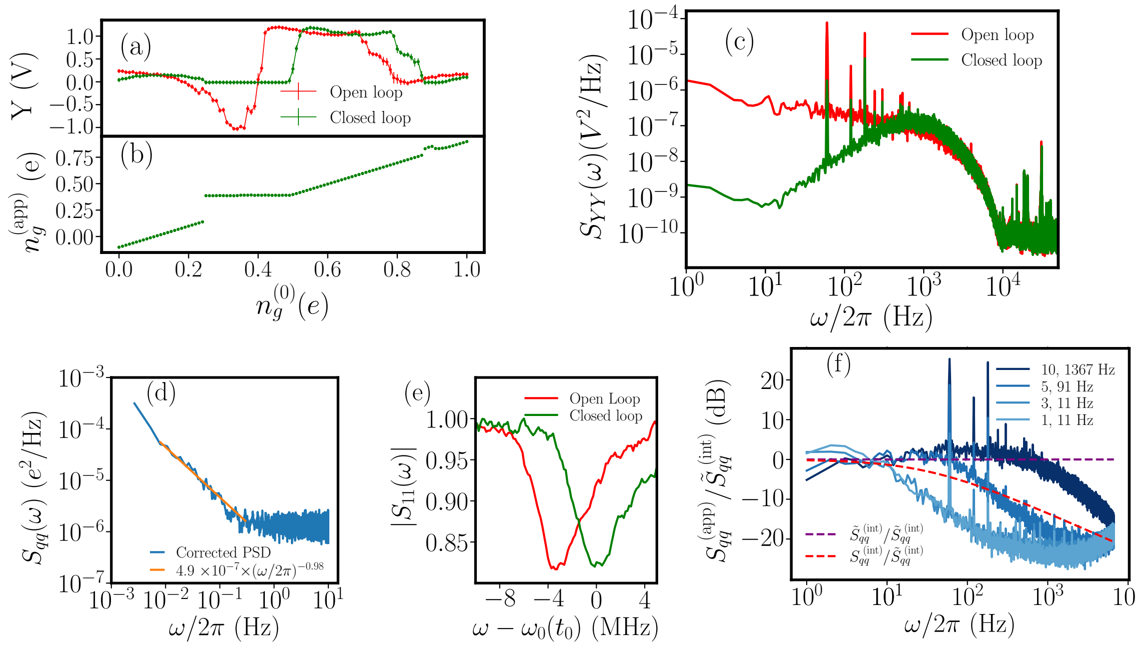

Figure 4.13: (a) Proof of concept for charge noise correction under feedback locking. The cCPT is gate-swept from $0 \leq n_g^{(0)} \leq 1$, for $\omega_c = \omega_0(0.4, 0)$ and $n = 5$. Each point corresponds to the averaged value of the measurements spanning 1 sec with a sampling rate 1 kHz, and the time constant set to 10 msec. Error-bars are also plotted to display the scale of fluctuations. For e.g., at $n_g^{(0)} = 0.4$, the standard deviations of the measured data are 135 mV and 50 mV for open-loop and closed-loop configurations, respectively. (b) Net corrected $n_g^{(\mathrm{app})}$ for the data in (a). (c) Comparison of measured $S_{YY}(\omega)$ displays a definitive suppression in the resonant fluctuations at $n = 10$ and bias point (0.6,0). (d) PSD of $n_g^{(\mathrm{app})}$ correcting the intrinsic bias noise at the cCPT in the frequency range 2-300 mHz. The measurement is completed in 7.5×10^3 sec with a sampling rate of 10 Hz. The cCPT is biased at (0.6,0) and the cavity is driven at $n = 10$. The orange plot displays an inverse-fit to this data accounted for frequencies up to 0.3 Hz. (e) Reflection coefficients of the cavity taken after the measurement in (d). Red and green plots correspond to cCPT biased at $n_g^{(0)} = 0.6$ (red), and $n_g^{(0)} = 0.6 + \delta n_g^{(\mathrm{app})} = 0.622$ (green), respectively. Due to a discrete jump in gate charge, the resonant frequency shifted nearly 4 MHz, and the feedback configuration accurately tracks this event. (f) $S_{qq}^{(\mathrm{app})}(\omega)/\tilde{S}_{qq}^{(\mathrm{int})}(\omega)$ in units of dB for different photon numbers n. The dashed purple plot is the fit obtained from Fig. 4.11(d) and corresponds to the apparent intrinsic charge noise, to act as a reference. The actual intrinsic charge noise is represented in the dashed red plot. The legends display n and the calculated 3 dB roll-off frequency for the corresponding plot. Except for $n = 10$, the rest of the measurements were taken with the lock-in amplifier time constant set at 300 μsec. The cCPT is biased at (0.6, 0) for $n = 10$ and $n = 5$, and at (0.4, 0) for $n = 3$ and $n = 1$.

the total averaged gate charge including the PID correction, $n_g^{(\mathrm{app})}$, [refer to 4.13(b)] are measured as the cCPT is gate-swept from $0 \leq n_g^{(0)} \leq 1$, for $\omega_c = \omega_0(0.4, 0)$. The quadrature $Y(t)$ is nulled, and $n_g^{(\mathrm{app})}$ is set to $n_g = 0.4$, across $|\delta n_g| \leq 0.1$. Note that the feedback correction continues in the right direction as long as $sgn(\delta n_g) = sgn(Y)$, until Y crosses zero; hence the corrected bandwidth applies to $\delta\omega_0 > \kappa_{\mathrm{tot}}$ as well, and the feedback, once locked, is robust against discrete gate-jumps of small magnitude.

The reduction of resonant frequency fluctuations can be directly observed by comparing the open and closed loop PSDs for $Y(t)$. This is shown in Fig. 4.13(c) and is measured under the same configuration as discussed in Figs. 4.11(c) and 4.11(d). Note that the detected 60, 120 and 180 Hz peaks are primarily from the compressors and pumps feeding our cryostat, and are sources of external noise. The system was monitored for 7.5×10^3 sec (∼2 hours), with $n_g^{(0)}$ chosen as 0.6 and the flux at a minimally sensitive point, with the cavity driven at $n = 10$. Figures 4.13(d) and (e) demonstrate the efficiency of the closed-loop system during the event of a discrete jump in gate charge, as mentioned above. Figure 4.13(d) displays the PSD of $n_g^{(\mathrm{app})}$ in the frequency range 2-300 mHz, corresponding to time-domain data collected with a sampling rate of 20 Hz. Figure 4.13(e) plots the reflection coefficient $|S_{11}(\omega)|$ after the measurement, with $n_g^{(0)} = 0.6 + \delta n_g^{(\mathrm{app})}$ corresponding to the feedback-locked value (green), and with $n_g^{(0)} = 0.6$ corresponding to the unlocked value (red). As can be seen, the resonance undergoes a shift of nearly 4 MHz due to a gate-charge jump during the measurement, and gets accurately tracked by the loop. It is to be noted that longer measurements also undergo a slow drift in the internal bias noise due to the presence of low-frequency components. As a result, $Y(t)$ deviates from the linear response described in Eq.(4.11), and becomes second-order, picking up contributions from $\delta b_{\mathrm{int}}^2(t)$. The PSD of the charge noise extraction from $S_{\mathrm{YY}}(\omega)$ as described in Eq. (4.18) breaks down in this regime.

Finally, Fig. 4.13(f) captures the feedback response for varying photon numbers $n = 10$, 5, 3 and 1, by plotting the PSD of the applied gate charge, $S_{qq}^{(\mathrm{app})}(\omega)$, in comparison to the apparent intrinsic charge noise $\tilde{S}_{qq}^{(\mathrm{int})}(\omega)$. The dashed purple and red plots are shown for reference, and represent the 0 dB point and $S_{qq}^{(\mathrm{int})}(\omega)/\tilde{S}_{qq}^{(\mathrm{int})}(\omega)$, respectively. We cannot accurately extract the noise floor in the closed loop setup since the gain of the transfer function changes. However, by placing $\tilde{S}_{qq}^{(\mathrm{int})}(\omega)$ as a reference, we can ensure that the net corrected gate PSD does not over-compensate for the noise floor fluctuations. This is important because of the smallness of the SNR, especially at $n = 1$. As can be observed, at $n = 10$, $n_g^{(\mathrm{app})}(\omega)$ follows the measured apparent charge noise closely. This implies a significant correction for the intrinsic charge noise, and the stabilization of the resonant frequency, with a roll-off set by the 3 dB point at ∼1.4 kHz. Due to the decrease in SNR(ω) as n is lowered [refer to Eq.(4.17)], we use a longer time constant for n=5 through n=1, resulting in a significant decrease in roll-off frequency near the single-photon limit.

Note that since the chosen bias point for n=10 and 5 in Fig. 4.13(e) is $(n_g, \Phi_{\text{ext}}) = (0.6, 0)$, the net applied gate charge also accounts for the QP switching noise. This is evident from the figure where the correction overshoots the actual intrinsic charge noise $S_{qq}^{(\text{int})}(\omega)$, represented by the dashed red plot. In contrast, the bias point is fixed at $(n_g, \Phi_{\text{ext}}) = (0.4, 0)$ for the cases of $n = 3$ and 1. The resulting feedback response better tracks the actual intrinsic noise in this regime since the QP interference is significantly reduced.

Section 4.5
Discussion

We observe that a major limitation in the efficient correction for charge noise at single photon occupancy of the cavity is the drastic decrease in SNR(ω). Along with the noise contributions from the amplifier chain at the TWPA, HEMT, and FET stages, the power detector amplifies the noise floor correlations at ω_{m} over the tunable bandpass filter bandwidth of 80 MHz. This can be best circumvented by using a series of notch filters before the detector with effective stop-bands within the 80 MHz bandwidth of the band-pass filter, but with pass-bands at ω_{c} and $\omega_{\text{c}} \pm \omega_{\text{m}}$. This ensures that detector input consists of mostly signal frequencies, thus decreasing the noise floor of the transfer function [refer to Fig. 4.11(c)].

As is evident in the previous discussion, another limiting constraint in our setup is the existence of quasiparticle poisoning in the CPT. This affects our choice of parameters in three ways. Firstly, the probability of switching to the odd electron state increases steadily towards charge degeneracy, due to its more favorable electrostatic energy configuration as compared to CPT's even band [98, 99]. The effect of quasiparticles on the extraction of the error signal can be observed in Fig. 4.13(a) near n_g = 0.8, where the resonance has completely switched to the odd parity. We therefore avoid operating the feedback at $|n_g| \geq 0.65$ to evade accidental destabilization of the loop. Moreover, near $n_g = 0.5$, $\delta\omega_0^{\text{qp}} = |\delta\omega_0^{(\text{odd})} - \delta\omega_0^{(\text{even})}| < \kappa_{\text{tot}}$. This can smear out the smooth monotonic function preferred for the accurate detection of charge noise using $Y(t)$. Finally, ω_{m} is chosen such that the sidebands are ensured to be away from both of the resonant frequencies. If $|\omega_{\mathrm{m}} - \delta\omega_0^{\mathrm{qp}}| < \kappa_{\mathrm{tot}}$, this assumption does not hold and results in a non-zero $|Y(n_g)|$ at resonance. In other cases, the sine quadrature is expected to detect a null signal whenever the cavity switches out of resonance (typically at frequencies 1 kHz - 100 kHz) and the effects of QP can be accounted for empirically as discussed in Sec. 4.3 [108].

The demonstration of charge noise correction reported in this work can also, in principle, be extended to reduce the effects of flux noise in the cCPT. However, in our setup, the DC flux line undergoes heavy filtering (with a cut-off frequency of 10 Hz) due to the RC low pass filter formed by the current limiting resistor and capacitor. The parasitic capacitance in the gate line leads to a RC filtering with cut-offf frequency >400 kHz. This ensures the feedback correction is not affected by the transfer function of the gate line itself, as opposed to the flux source.

Chapter 5

Measurement Imprecision

The highly tunable and strongly nonlinear nature of the cCPT is evident from the analysis in Chapter 3. In this chapter, we narrow our focus to examine the operation of the cCPT as a linear charge detector. A comprehensive understanding in the linear response regime is an essential first step before widening the scope of the device operation to include nonlinear contributions, for example to realize phase-sensitive amplification via squeezing.

In §5.1, we theoretically investigate the potential of the cCPT to be operated in the quantum-limited electrometric regime. In §5.2 we present actual charge sensitivity measurements using feedback techniques borrowed from Chapter 4, effectively demonstrating improvements in the observed charge sensitivity with and without environmental noise decoupling.

Section 5.1

cCPT as a linear electrometer (Theory)[1]

In the simplest terms, we see from Eq. (3.49) how a sinusoidal modulation in the gate charge appears as a renormalization-shift in the cavity resonance frequency. In particular, this gate modulation may be induced using a mechanical quantum dynamical system coupled at the CPT gate [34], thus facilitating sensing of the mechanical system via charge detection. A typical measurement involves driving the cavity near resonance, and detecting the sidebands via measurements of the output power averaged over some time T_M that is long compared to the characteristic time-scales of the

---

[1] We acknowledge that the bulk of this section is reproduced from a Journal of Applied Physics publication by Kanhirathingal *et. al.* [13], with major contributions from Prof. Blencowe.

cCPT-mechanical system dynamics.

In line with such a scheme, we will first look into the output power generation in the presence of an electrically simulated, sinusoidal gate modulation "signal" $\delta n_g(t) = \delta n_g^{(0)} \cos(\omega_g t)$. This will enable a determination of the charge sensitivity of the cCPT in the low-average photon number drive limit, which we will find to be comparable to previously reported or predicted values for electrometers [109, 33, 30, 110, 111, 112, 32]. Most importantly, the behavior of the cCPT in this low drive power regime is limited by photon shot noise in the transmission line, which results in an attainable quantum-limited lower bound for charge sensitivity.

5.1.1. Output Power

The output power at the sample stage in the presence of a gate modulated signal can be estimated using the same series of steps as for the bare cavity in Sec. 2.4. In particular, we proceed to derive a modified quantum Langevin equation (5.1) and then extend the resulting input-output equation to find the analogous expression to Eq. (2.76) that represents the output power (5.8). Details of this derivation are given below, where we observe from Eqs. (5.4)-(5.7) that the gate modulation introduces sidebands into the cavity frequency spectrum, and is detected by measuring the output power as expressed in Eq. (2.74).

Internal noise/losses are modeled as a second, internal thermal bath denoted as ρ_ι, modifying the total input state: $\rho_{\text{in}} = \rho_{\alpha,p} \otimes \rho_\iota$. The thermal occupancies of the pump n_p and internal bath n_ι are usually assumed to be identical, as the temperature variations at different locations in the device are neglected. However, in reality, the internal bath may have a different noise temperature due, for example, to coupling with two-level defects [95].

Limiting the relevant frequency space to the region of the fundamental cavity mode frequency: $|\omega - \omega_0| \ll \omega_0$, we obtain from Eq. (3.37) the following, approximate modified quantum Langevin equation to first order in $\xi = C_{pc}/(\mathcal{C}_c l) \ll 1$:

$$\left(\omega - \omega_0 + i\frac{\kappa_{\text{ext}}}{2}\right) a_0(\omega) = \sqrt{\kappa_{\text{ext}}}\, a_p^{\text{in}}(\omega) + g \int_0^\infty d\omega' F(\omega, \omega'), \tag{5.1}$$

where a_0 is given by Eq. (2.61) for ω in the vicinity of the cCPT renormalized, fundamental mode frequency ω_0 [Eq. (3.42)] and κ_{ext} is given by Eq. (2.59) similarly in terms of the cCPT renormalized fundamental resonance frequency. Note that the

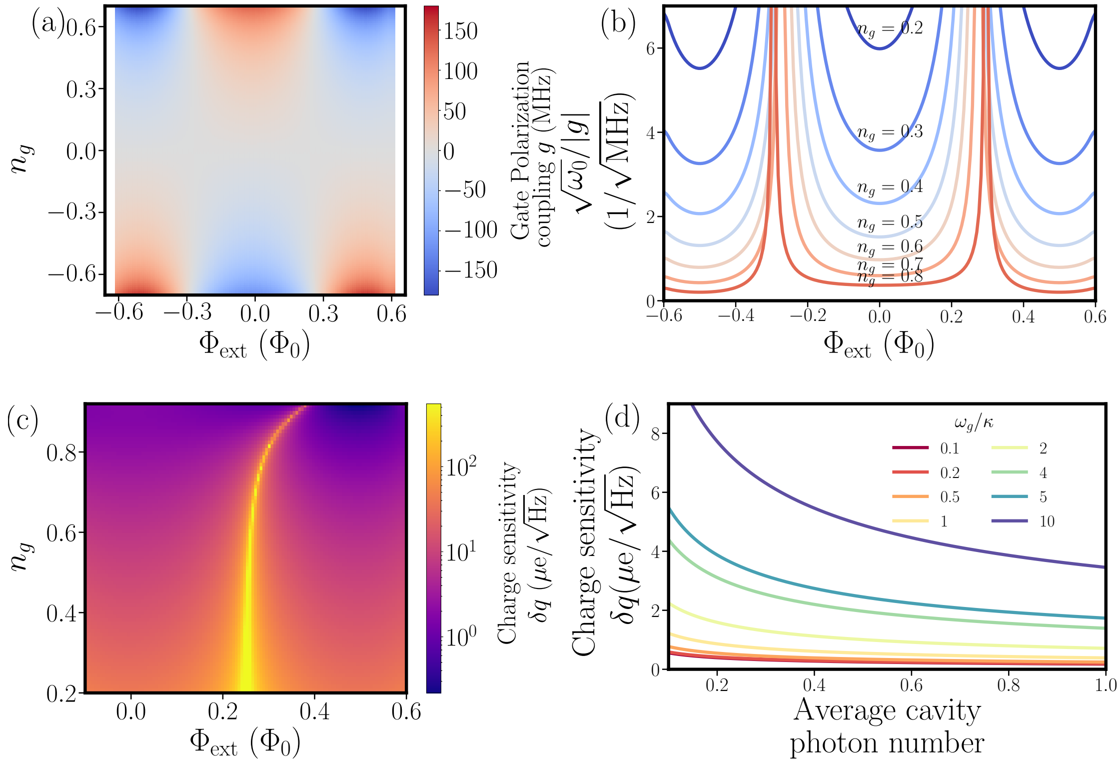

Figure 5.1: (a) Gate polarization coupling in MHz across the tunable bias range. The coupling becomes stronger in the direction of charge degeneracy. (b) The ratio $\sqrt{\omega_0}/|g|$ as a function of $\Phi_{\rm ext}$ for different values of n_g. The fundamental charge sensitivity δq is proportional to this ratio and the improved values are attained closer to charge degeneracy. (c) δq for an average of one photon in the cavity, with $\omega_g/\kappa = 1$. The values reported here assume contribution from a single side-band. (d) Comparing δq in the bad-cavity and good-cavity limit. The bias point is chosen at ($\Phi_{\rm ext} = 0.5\Phi_0, n_g = 0.9$) which gives $\delta q = 0.17$ $\mu e/\sqrt{\rm Hz}$ for an average of one photon in the cavity in the bad-cavity limit.

gate modulation introduces higher order corrections to $a_0(\omega)$ via the term

$$\begin{aligned}F(\omega,\omega') = &\frac{1}{\sqrt{2\pi}}\frac{\omega_0}{\sqrt{\omega\omega'}}e^{-i(\omega-\omega')l/v_c}\\ &\times\left\{\sqrt{\frac{\pi}{2}}\delta n_g^{(0)}\left[\delta\left(\omega-\omega'+\omega_g\right)+\delta\left(\omega-\omega'-\omega_g\right)\right]\right.\\ &\left.-N_p^{\text{in}}(\omega-\omega')\right\}\sin\left(\omega' l/v_c\right)a_0(\omega'). \end{aligned} \tag{5.2}$$

We may further simplify Eq. (5.1) by neglecting $N_p^{\text{in}}(\omega-\omega')$ in Eq. (5.2) owing to the smallness of its noise contribution, and noting also that the ω, ω' dependent terms multiplying $a_0(\omega')$ in Eq. (5.2) can be approximately evaluated at ω_0 since we assume $\omega_g, \kappa_{\text{ext}}, \Delta\omega \ll \omega_0$, where $\Delta\omega$ is the measured output power bandwidth centered at the pump frequency ω_p. Introducing internal effective cavity losses using a phenomenological constant damping rate κ_{int}, channeled via an additional non-measurable input port $a_\iota^{\text{in}}(\omega)$, we obtain:

$$\left(\omega-\omega_0+i\frac{\kappa_{\text{tot}}}{2}\right)a_0(\omega) = \sqrt{\kappa_{\text{ext}}}a_p^{\text{in}}(\omega)+\sqrt{\kappa_{\text{int}}}a_\iota^{\text{in}}(\omega)+g\int_0^\infty d\omega' A(\omega-\omega')a_0(\omega') \tag{5.3}$$

where

$$A(\omega) = \frac{1}{2}\delta n_g^{(0)}\left[\delta\left(\omega+\omega_g\right)+\delta\left(\omega-\omega_g\right)\right]. \tag{5.4}$$

Solving Eq. (5.3) perturbatively in the limit of small g, we have

$$a_0(\omega) = \sum_{n=0} g^n\,\mathcal{I}_n(\omega), \tag{5.5}$$

where the zeroth order term in (5.5) is

$$\mathcal{I}_0(\omega) = \frac{\sqrt{\kappa_{\text{ext}}}a_p^{\text{in}}(\omega)+\sqrt{\kappa_{\text{int}}}a_\iota^{\text{in}}(\omega)}{\left(\omega-\omega_0+i\frac{\kappa_{\text{tot}}}{2}\right)}, \tag{5.6}$$

and the iterative solution relation for $\mathcal{I}_n(\omega)$ is given by

$$\mathcal{I}_n(\omega) = \int_0^\infty d\omega'\,\frac{\mathcal{I}_{n-1}(\omega')A(\omega-\omega')}{\omega-\omega_0+i\frac{\kappa_{\text{tot}}}{2}}. \tag{5.7}$$

Considering the time-domain expression for $a_0(t)$ using Eq. (5.3), we obtain the following necessary condition for linear charge detection: $g\delta n_g^{(0)}/\omega_g \ll 1$. In this linear detection regime, the output power reaching the first-stage amplifier is given by

$$\begin{aligned} P^{\text{out}}(\omega_0, \Delta\omega) = P_p^{\text{in}} \int_{\omega_0-\Delta\omega/2}^{\omega_0+\Delta\omega/2} d\omega \Bigg\{ & \frac{\delta\omega^2 + \left(\frac{\kappa_{\text{ext}}-\kappa_{\text{int}}}{2}\right)^2}{\delta\omega^2 + \left(\frac{\kappa_{\text{tot}}}{2}\right)^2} \delta(\omega-\omega_p) + \frac{\left(\kappa_{\text{ext}} g \delta n_g^{(0)}/2\right)^2}{\delta\omega^2 + \left(\frac{\kappa_{\text{tot}}}{2}\right)^2} \\ & \times \left[\frac{1}{\left(\delta\omega+\omega_g\right)^2 + \left(\frac{\kappa_{\text{tot}}}{2}\right)^2} \delta(\omega+\omega_g-\omega_p) + \frac{1}{\left(\delta\omega-\omega_g\right)^2 + \left(\frac{\kappa_{\text{tot}}}{2}\right)^2} \delta(\omega-\omega_g-\omega_p) \right] \Bigg\} \\ & + \frac{\hbar\omega_0}{2\pi} \int_{\omega_0-\Delta\omega/2}^{\omega_0+\Delta\omega/2} d\omega \left[n_p(\omega) + \frac{1}{2} + \frac{\kappa_{\text{ext}}\kappa_{\text{int}} \left(n_\iota(\omega) - n_p(\omega)\right)}{(\omega-\omega_p)^2 + \left(\frac{\kappa_{\text{tot}}}{2}\right)^2} \right]. \end{aligned} \tag{5.8}$$

Since $g\delta n_g^{(0)}/\omega_g \ll 1$, we neglect the noise floor contribution of g^2 order. We also neglect the order g^2 signal contribution at $\omega = \omega_p$, which is dominated by the reflected pump tone; the actual signal is obtained from either (or both) of the sidebands at $\omega_p \pm \omega_g$.

5.1.2. Photon Shot-noise Limited Charge Sensitivity (Theory)

The major motivation behind the theoretical framework provided in this section is to identify the potential applicability and fundamental limitations of the cCPT as a linear charge detector subject to the laws of quantum mechanics. This essentially implies disregarding the sources of noise that may arise from any experimental materials complexity and which are not limited in principle by quantum mechanics. To address this fundamental charge sensitivity limit, we shall therefore neglect the internal bath by setting $\kappa_{\text{int}} = 0$, and consider the response of the cCPT at absolute zero temperature for the pump/probe line, i.e., $n_p = 0$. The cCPT performance under these conditions is determined by its essential coupling with the pump/probe line at the output and the measured system at the input. In the absence of a physical system at the input, the noise feeding the input of the subsequent amplifier stage thus originates from the vacuum photon shot noise of the transmission line, determining the lower bound for the charge-sensitivity. In reality, additional noise source channels can prevent achieving this fundamental charge sensitivity limit, as discussed further below.

The charge sensitivity δq (e/$\sqrt{\text{Hz}}$) of an electrometer is defined as the rms charge modulation amplitude that corresponds to a signal-to-noise ratio of one (in a bandwidth of 1 Hz) at the amplifier input [30]. We can thus solve for the fundamental charge sensitivity of the cCPT from the total output power expression (5.8) by setting $\omega_p = \omega_0$, and looking at the output power variation about $\omega_0 \pm \omega_g$ within a bandwidth of $\Delta\omega = 2\pi \times 1$ Hz to obtain:

$$\delta q = |g|^{-1} \sqrt{\frac{\hbar\omega_0 \left(\omega_g^2 + (\kappa/2)^2\right)}{4P_p^{\text{in}}}} \, \text{e}/\sqrt{\text{Hz}}, \tag{5.9}$$

where κ now denotes the damping solely due to the coupling to pump/probe line κ_{ext}, given by Eq. (2.59) in terms of the cCPT renormalized fundamental resonance frequency (3.42). Equation (5.9) may alternatively be expressed in terms of the average photon number in the cavity n_{cav} as follows:

$$\delta q = |g|^{-1} \sqrt{\frac{\left(\omega_g^2 + (\kappa/2)^2\right)}{\kappa \, n_{\text{cav}}}} \, \text{e}/\sqrt{\text{Hz}}. \tag{5.10}$$

The sensitivity may be further improved using a homodyne detection scheme, where the combined contribution of both the sidebands lead to values lower by a factor of $\sqrt{2}$ [111].

The most charge sensitive points can be identified using the plots in Fig. 5.1. Regardless of the input drive and signal frequency ω_g, the charge sensitivity in general improves as n_g approaches (but does not equal) one [Fig. 5.1(b)]. In the case of an average of one photon in the cavity with $\omega_g/\kappa = 1$, Fig. 5.1(c) shows the fundamental charge sensitivity behavior across the entire bias range for a single sideband. We obtain $\delta q = 0.39\,\mu\text{e}/\sqrt{\text{Hz}}$ at $(\Phi_{\text{ext}}, n_g) = (0.5\,\Phi_0, 0.9)$ for the above parameter values, while working well within the adiabatic approximation limit. Moreover, the efficiency of the charge detector can be best exploited in the bad-cavity limit $\omega_g \ll \kappa$, where the value of δq saturates to $0.17\,\mu\text{e}/\sqrt{\text{Hz}}$ for an average of one cavity photon [Fig. 5.1(d)]. The values used in our numerical simulations are given in Table 3.1; however an optimization of the E_C, E_J values may further improve the charge sensitivity slightly.

Kerr Considerations: It is worthwhile noting that the highly anharmonic, effective potential (3.47) of the cCPT leads to non-negligible contributions from the quartic Kerr potential term even near an average of one cavity photon. In theory, it is possible to substantially improve the performance of the cCPT by driving the cavity at the onset of bistability (and where the cCPT still behaves as a linear electrometer) as long as the signal is within $g\delta n_g^{(0)}/\omega_g \ll 1$ [64, 30].

Section 5.2

cCPT as a linear electrometer (Experiment)

Despite the cCPT's potential as an ultra-sensitive charge detector as demonstrated through theory in the previous section, the experimental limitations during fabrication and measurements can hinder its ability to perform at this optimum sensitivity. In addition to the noise contributions at the sample stage, the measurement precision is also limited by the noise added at the subsequent amplifier stages (where the minimum noise added by a quantum-limited phase insensitive amplifier is $\hbar\omega_0/2$). As mentioned in §3.5, other transport mechanisms such as quasiparticle poisoning may dominate the resonance characteristics when we operate closer to charge degeneracy. The internal damping of the cavity further limits the charge sensitivity, modifying the fundamental, quantum limited expression (5.9) as follows:

$$\delta q = |g|^{-1}\frac{\kappa_{\text{tot}}}{\kappa_{\text{ext}}}\sqrt{\frac{\hbar\omega_0\left(\omega_g^2+(\kappa_{\text{tot}}/2)^2\right)}{4P_p^{\text{in}}}}\ \text{e}/\sqrt{\text{Hz}}. \tag{5.11}$$

The sources of these internal losses primarily considers the direct interactions of the cavity with its local environment [52, 92, 93]. As investigated in detail in chapter 4, in practice, there also exist sources of dephasing via microscopic two level system (TLS) degrees of freedom located in the vicinity of the CPT, for example within the underlying substrate and Josephson tunnel junction oxide layers. These defects couple via their electric and magnetic dipole moments to the cCPT system charge and flux coordinates [39, 113, 114] and cause resonant frequency fluctuations during real-time measurements that are typically manifested as $1/f$ noise (see Fig. 4.11). This makes it challenging to precisely set the pump tone on resonance as we have assumed in the last section. While characterizing the experimental device performance, it is thus crucial to take these fluctuations into account since they can be erroneously equated with additional damping.

The observed charge sensitivity of the actual cCPT device in the presence of such intrinsic charge noise is reported to be nearly three times worse than our theoretical predictions [15] and is limited by the low-frequency resonant frequency fluctuations of the cCPT. In this section, we investigate methods to improve the experimental electrometric properties of the cCPT closer to the photon shot-noise limited value. In particular, we will utilize the techniques discussed in Chapter 4 to decouple the charge noise and stabilize the resonant frequency of the cavity.

5.2.1. Measurement Setup

In essence, the measurement of the charge sensitivity in an experimental setting requires driving the cavity near resonance, in the presence of a gate modulated signal $\delta n_g(t) = \delta n_g^{(0)} \cos(\omega_g t)$, and further analysing the sideband features of the output field. The latter can be achieved either by the direct measurement of the power spectrum using a spectrum analyzer [15], or using a homodyne/heterodyne detection scheme via a digitizer. A homodyne detection essentially mixes the output with a local oscillator (LO) at the resonant frequency. This results in increased SNR by combining the information-carrying sidebands into one single frequency. As the detection is ultimately limited by the low-frequency noise near the DC, a heterodyne scheme (involving LO displaced from resonance) is sometimes preferred, especially at lower ω_g values.

In this section, we will however perform power spectral density measurements using a spectrum analyzer. Such a measurement is more easy to incorporate into the circuit scheme given in Fig. 4.7, where a directional coupler is used to route one component of the output signal to a spectrum analyzer, and the other component simultaneously allowing for feedback correction of the resonant frequency. The output power measured at the spectrum analyzer is directly proportional to the expression in Eq. (5.8), with the proportionality constant determined by the gain features of the subsequent amplifier chain. However, the noise floor is elevated due to the presence of the near-quantum-limited amplifier, the TWPA, that further adds few photons of noise into the signal, besides the photon shot-noise represented by the third line in Eq. (5.8). It may thus help to consider the cCPT as a zeroth-stage, linear, quantum-limited amplifier of charge fluctuations, followed by another quantum-limited amplifier in the first stage of the net chain (see Fig. 5.2). As each of these amplifiers add a minimum of $\hbar\omega/2$ of noise, the detection is quantum-limited by a noise floor of $\hbar\omega$.

Finally, following the definition for charge sensitivity δq presented above Eq. (5.9), we may measure the magnitude of δq from the power spectral output using [15]

$$\delta q = \frac{q_{\mathrm{rms}}}{\sqrt{2B} \times 10^{\mathrm{SNR}/20}}, \tag{5.12}$$

where q_{rms} is the rms of the charge modulation amplitude $\delta n_g^{(0)}$, B is the resolution bandwidth of the spectrum analyzer, and SNR is the signal-to-noise ratio of the

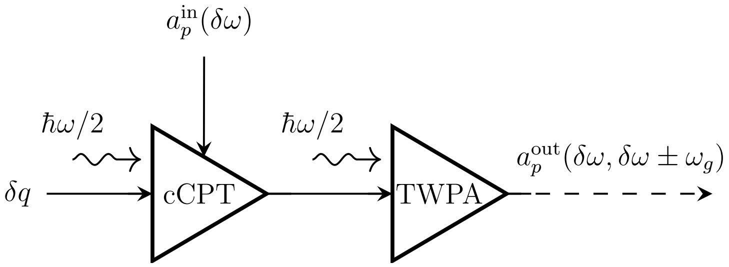

Figure 5.2: Quantum-limited charge sensing using the cCPT and TWPA which adds a total of $\hbar\omega$ of noise during detection.

single sideband in dB. We can thus compare the observed magnitudes to the theoretical model predicted using Eq. (5.11) and determine the fidelity of charge sensing measurement in the quantum limit.

5.2.2. Charge Modulation Amplitude at 30 mK

For the accurate extraction of q_{rms} at the sample stage, a measurement of the attenuation in the gate line is required since the applied voltage at room temperature undergoes a low-pass transfer function. In our setup, this attenuation occurs in two stages. Firstly, the summing amplifier that adds the input gate, PID correction, and the gate modulation is bandwidth-limited near 1 MHz. Therefore, we first measure the transfer function of the gate line at room temperature before it enters the dilution fridge (see Fig. 5.3a). Next, since the Cu wire used as the gate line inside the fridge and the associated parasitic capacitance forms a second RC filter, the applied q_{rms} is further attenuated at 30 mK. The output power at the sidebands in Eq. (5.8) as a result can be re-expressed as

$$P^{\mathrm{out}}(\omega_p \pm \omega_g) = \frac{BP_p^{\mathrm{in}}(\omega_p)}{\left[\delta\omega^2 + (\kappa_{\mathrm{tot}}/2)^2\right]} \frac{\left(\kappa_{\mathrm{ext}} g q_{\mathrm{rms}}^{\mathrm{RT}}\right)^2}{\left[(\delta\omega \mp \omega_g)^2 + (\kappa_{\mathrm{tot}}/2)^2\right]\left[1 + (\omega_g/\omega_{\mathrm{Cu}})^2\right]}, \quad (5.13)$$

where $q_{\mathrm{rms}}^{\mathrm{RT}}$ is the rms gate modulation amplitude measured at the room temperature (obtained for $\omega_g = 0$), and ω_{Cu} is the single-pole, low-pass cutoff frequency of the gate line down to 30 mK.

Hence for n_g values where the charge noise does not add a substantial $1/f$-noise to $\delta\omega$, we may use the above expression to extract ω_{Cu}. In order to remove any Kerr nonlinear effects, we also fix $P_p^{\mathrm{in}}(\omega_p)$ corresponding to $n < 1$. As a result, Eq. (5.13)

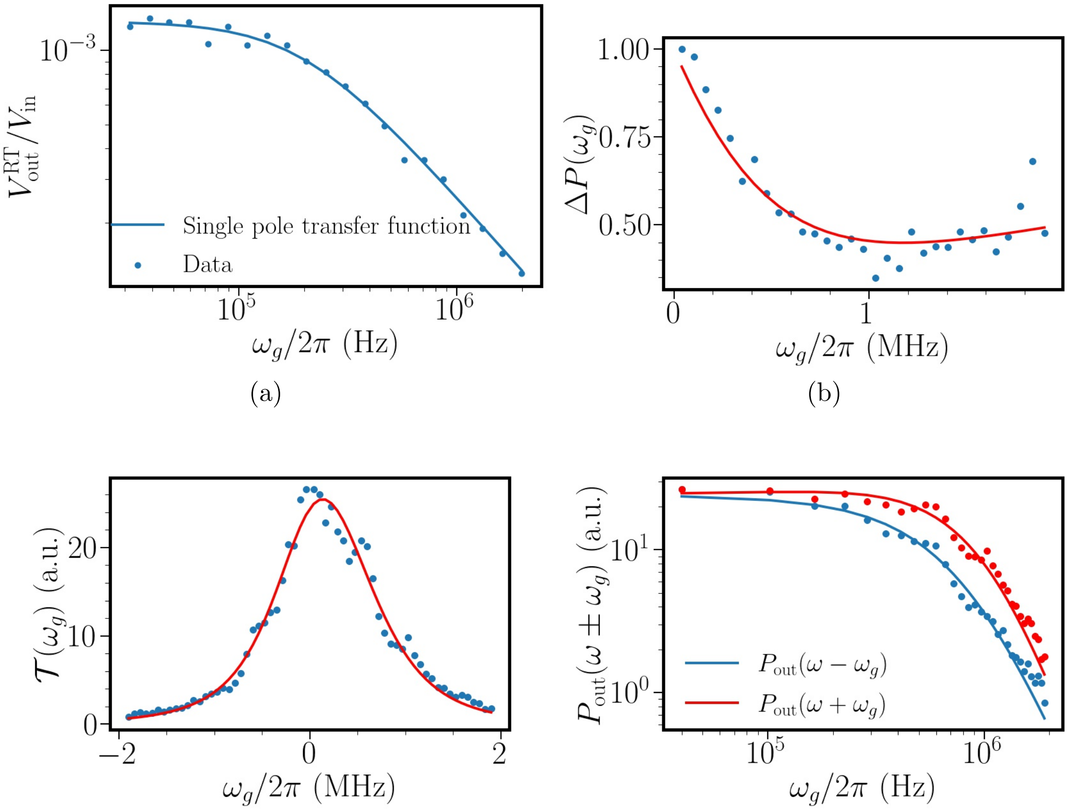

(a)

(b)

(c)

(d)

Figure 5.3: (a) Transfer function of the gate line at room temperature with contributions from the summing amplifier and the voltage divider. The cutoff frequency obtained for the fit is 0.2 MHz, and the voltage divider ratio is 765. (b) Fitting ΔP as given in Eq. (5.15). Results of the fit are $\delta\omega/2\pi = 0.44$ MHz and $\kappa_{\text{tot}}/2\pi = 2.17$ MHz. Note the total damping rate of the fit is higher as we have not included the frequency fluctuations due to low-frequency noise and the backaction from TWPA in this model. (c) Fitting the output power of both the sidebands as a function of gate frequency ω_g, per Eq. (5.14). The values obtained are $\kappa_{\text{tot}}/2\pi = 2.18$ MHz and $\omega_{\text{Cu}}/2\pi = 0.736$ MHz and $\delta\omega/2\pi = 0.44$ MHz. This cutoff frequency is close to the estimated value at room temperature considering the length of the Cu wire. (d) Output power of each sideband plotted in log scale, following the fits in (b) and (c).

can be used to obtain ω_{Cu} using the model

$$\mathcal{T}(\omega_g) = \frac{C}{\left[(\delta\omega - \omega_g)^2 + (\kappa_{\mathrm{tot}}/2)^2\right]\left[1 + (\omega_g/\omega_{\mathrm{Cu}})^2\right]}, \tag{5.14}$$

under a change of variable $\omega_g \rightarrow -\omega_g$ for negative sidebands, and C set as the proportionality constant (including the gain of the amplifier chain). Furthermore the asymmetry can be quantified using $\Delta P \equiv P^{\mathrm{out}}(-\omega_g)/P^{\mathrm{out}}(+\omega_g)$:

$$\Delta P = \frac{(\delta\omega - \omega_g)^2 + (\kappa_{\mathrm{tot}}/2)^2}{(\delta\omega + \omega_g)^2 + (\kappa_{\mathrm{tot}}/2)^2}. \tag{5.15}$$

The results of these fits are plotted in Fig. 5.3, where we obtain a cut-off frequency of 736 kHz for the gate line.

5.2.3. Enhanced Charge Sensing

We are now equipped to look at the enhanced charge sensing properties of the cCPT as a consequence of its decoupling from the environmental charge noise, achievable through feedback techniques detailed in Chapter 4. In short, we measure the charge sensitivity of the cCPT by looking at the output power response as given in Eq. (5.12), with and without feedback. The results of these measurements are given in Fig. 5.4 where the cavity is driven at $n = 10$ and $n = 1$, and is biased at the charge-sensitive point $(n_g, \Phi_{\mathrm{ext}}) = (0.6, 0)$.

As illustrated in Fig. 5.4a, we observe a definite improvement in the magnitude of the charge sensitivity in the presence of feedback. This improvement is significant for $n = 10$, especially for higher ω_g values. We attribute this enhancement to the resonant frequency stabilization in the low-frequency noise up to 1.4 kHz, as previously demonstrated through Fig. 4.13. However, it is to be noted that this operation is well outside the single-photon charge sensing regime discussed in §5.1, since for $n = 10$ the Kerr-effects are significant to even drive the cavity beyond the Kerr bifurcation point. Thus Fig. 5.4a is to be looked at from a demonstrative viewpoint only.

On the other hand, Fig. 5.4b demonstrates enhancement of the charge sensing capabilities of the cCPT at the single photon level. Unfortunately, we observe that the detection scheme we adopted measures charge modulations approximately 10 times worse than the optimized value reported for the same device by Brock *et. al* [15], even in the absence of the feedback. Such a drastic difference is a consequence of two factors that were not taken care of during these preliminary measurements.

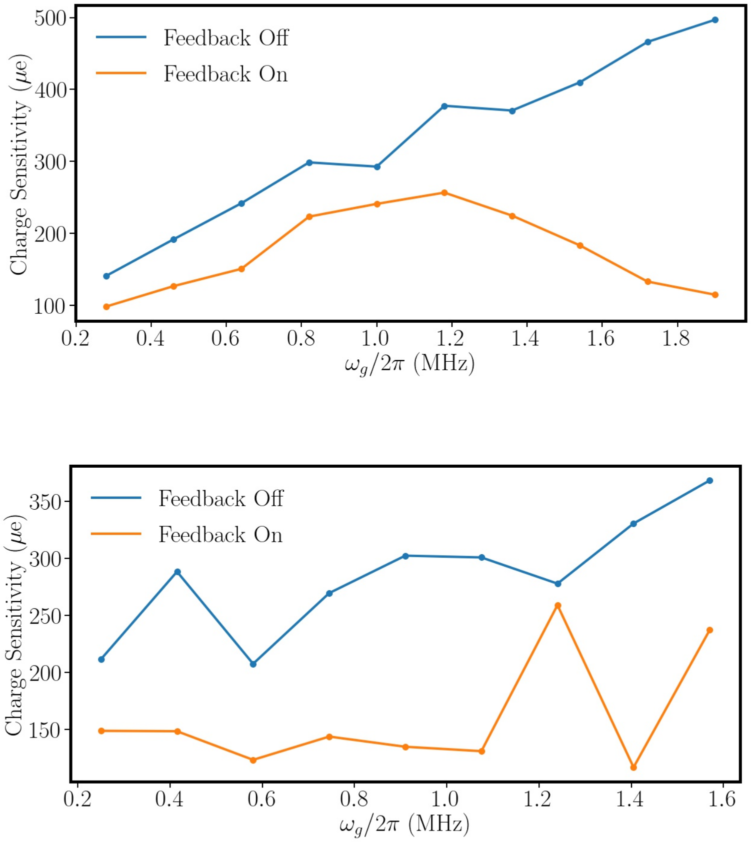

Figure 5.4: Results of the charge sensitivity measurement by the spectrum analyzer with and without feedback. The cavity is biased at $(n_g, \Phi_{\text{ext}}) = (0.6, 0)$ and the resolution bandwidth of the specturm analyzer is set to 1 Hz. (a) The cavity is driven at an average of 10 photons, which is well into the bifurcation regime. (b) The cavity is driven at the single-photon level.

One, the gate input line in Fig. 4.7 is devoid of any attenuators and bias tees as opposed to the circuit scheme used by [14]. As a result, the minute charge modulation voltage amplitudes applied at room temperature undergo a decrease in SNR due to addition of thermal noise, thus making the system prone to high-frequency external noise. Secondly, the TWPA parameters used to achieve first-stage amplification is the optimized value for the cCPT's entire tunable range. By optimizing the TWPA's drive pump and frequency such that the added noise at this stage when the cCPT is biased at $(n_g, \Phi_{\text{ext}}) = (0.6, 0)$ corresponds to ~1.2 photons as reported by [14], we can potentially elevate the measurement performance to a comparable regime.

Nevertheless, it can be safely deduced from these promising results that the cCPT can perform as a near quantum-limited electrometer in the single-photon limit, by decoupling the intrinsic charge noise and stabilizing it's resonant frequency in real time. The underpinning detrimental features of the setup utilized in this scheme has significant room for improvement, and can be implemented via the addition of attenuators along the gate line and a recalibration of the TWPA's drive parameters.

Chapter 6

Future Work

In this chapter, we present a summary of the future directions branching out of the main content presented in this thesis. In particular, §6.1 details the need for investigating the concept of phase operator measurement in the low-photon regime. Section 6.2 covers topics on ways to generalize the suppression of environmentally-induced noise in superconducting, tunable microwave cavities. In §6.3, we briefly look at an alternate mode of charge sensing possible using the cCPT – phase-sensitive detection.

Section 6.1

Standard Quantum Limit in the Single-photon Regime

One of the key applications of the cCPT is to perform quantum measurements using phase-preserving amplification of an observable of another measurable quantum system, such as a qubit or a mechanical resonator. Of particular interest is a tripartite coupling involving the cavity and a mechanical resonator interacting via the CPT, where the resulting, tunable CPT-induced effective optomechanical interaction may approach the single photon-single phonon ultrastrong coupling regime [34].

Since the device operation is limited by quantum noise, a natural extension of the work presented in §5.1.2 is to investigate how closely the cCPT detector approaches the standard quantum limit, with the back-action of the cCPT on the measured system taken into account. In the conventional case of large photon driving, the coupling term in the opto-mechanical Hamiltonian can be linearized in the cavity and mechanical oscillator coordinates, and the information about the position of the mechanical resonator can be extracted using a single quadrature measurement [79], as discussed in Appendix A.

Furthermore, the force acting on the mechanical resonator (MR) due to the action of cavity can be obtained using

$$F_L = \frac{\partial \hat{\mathcal{H}}}{\partial \hat{x}} = \frac{\sqrt{2}\hbar \mathcal{G}}{x_{zp}} X, \tag{6.1}$$

where X is the in-phase quadrature of the cavity [Eq. (A.14)], $\mathcal{H}$ is the open-system Hamiltonian [Eq. (A.8)], and $\mathcal{G}$ is the optomechanical coupling as defined in Appendix A. The radiation pressure force power spectral density thus becomes

$$S_{FF}(\omega) = \frac{8}{\kappa}\left(\frac{\hbar \mathcal{G}}{x_{zp}}\right)^2 S_{X_{\text{in}}X_{\text{in}}}(\omega), \tag{6.2}$$

where we used the relation in Eq. (A.14). Similarly, the minimum possible measurement (imprecision) noise S_{xx}^{imp} is obtained from Eq. (A.14) as

$$S_{xx}^{\text{imp}} = \frac{\kappa}{8}\left(\frac{x_{zp}}{\mathcal{G}}\right)^2 S_{Y_{\text{in}}Y_{\text{in}}}. \tag{6.3}$$

Combining the two results in (6.2) and (6.3), we obtain the uncertainty in the back-action noise $S_{FF}(\omega)$ and the imprecision noise in position $S_{xx}^{\text{imp}}(\omega)$ bounded by the inequality [79]

$$S_{FF}(\omega) S_{xx}^{\text{imp}}(\omega) \geq \left(\frac{\hbar}{2}\right)^2 \tag{6.4}$$

using the commutation relation $[X_{\text{in}}, Y_{\text{in}}] = i$.

In the low average cavity photon number limit, however, we must retain the original form of the opto-mechanical Hamiltonian [62]:

$$\mathcal{H} \;=\; \hbar\Delta a^\dagger a + \hbar\Omega\, b^\dagger b + \hbar G a^\dagger a x, \tag{6.5}$$

where a and b denote the cavity and mechanical resonator annihilation operators respectively, x is the oscillator position, $\Delta = \omega_0 - \omega_p$, Ω is the mechanical oscillator frequency, and G determines the optomechanical coupling. As shown in Appendix B, the information about the position of the mechanical resonator can no longer be extracted using a X quadrature measurement; rather, the displacement information is encoded in the phase of the reflected signal.

Furthermore, the force experienced by the the MR due to the cavity is given by [following the definition in Eq. (6.1)]

$$F_L = \left(\frac{\hbar G}{x_{zp}}\right) a^\dagger a, \tag{6.6}$$

and subsequently, the radiation pressure force power spectral density takes the form

$$S_{FF}(\omega) = \left(\frac{\hbar G}{x_{zp}}\right)^2 S_{NN}(\omega), \tag{6.7}$$

where S_{NN} is the cavity photon number noise and x_{zp} is the mechanical resonator position zero-point uncertainty. Drawing parallels between the two regimes, we deduce that the corresponding imprecision noise spectral density $S_{xx}^{\mathrm{imp}}(\omega)$ depends on $S_{\theta\theta}(\omega)$ (since $[X_{\mathrm{in}}, Y_{\mathrm{in}}] = [N, \theta] = i$).

Investigations probing the standard quantum limits achievable in the combined cCPT-mechanical oscillator system in the presence of low average photon number drive thus requires considering ways to measure the phase operator $\hat{\theta}(\omega)$ itself. However, the definition of the phase operator has evolved over the years; one possible definition is the Susskind-Glogower (SG) formalism [78, 115]. In short, we may define the operators

$$\begin{aligned} \hat{E} &\equiv (aa^\dagger)^{-1/2} a = e^{i\hat{\theta}} && (6.8)\\ \hat{E}^\dagger &\equiv a^\dagger (aa^\dagger)^{-1/2} = e^{-i\hat{\theta}} && (6.9)\\ \hat{C} &= \frac{1}{2}\left(\hat{E} + \hat{E}^\dagger\right) && (6.10)\\ \hat{S} &= \frac{1}{2i}\left(\hat{E} - \hat{E}^\dagger\right) && (6.11) \end{aligned}$$

where the relevant commutation relations are $[\hat{C}, \hat{N}] = i\hat{S}$ and $[\hat{S}, \hat{N}] = -i\hat{C}$. As before, we can similarly write down the equations of motion for some of these observables and try solving these in Fourier space. However, these calculations get excessively complicated unless the approximation $\hat{S} \approx \hat{\theta}$ is made.

Thus the measurement of the phase operator in experiments typically assumes the smallness of θ. For example, using a definition of θ that relates $a_{\mathrm{out}} = re^{i\theta} a_{\mathrm{in}}$, Clerk's review [1] approximates $\langle\theta\rangle = \langle Y\rangle/\langle X\rangle$. While this form is valid for high n, further investigations are required to devise a formalism to measure the phase operator in the low-photon limit, especially how it shows up in the quadrature detection schemes.

It is worthwhile noting that the above approximation for the phase in terms of the quadratures, $\langle\hat{\theta}\rangle = \langle\hat{Y}\rangle/\langle\hat{X}\rangle$, no longer holds in this limit (refer Appendix C); further studies at a fundamental level are required to understand the behaviour of the phase operator, both theoretically and experimentally [116, 117, 118, 119, 120, 115].

Section 6.2

Environmental Noise Decoupling in Tunable Superconducting Cavities - Generalization

As extensively discussed in Chapter 4, it is possible to achieve resonant frequency stabilization in the cCPT by decoupling charge noise over a bandwidth greater than 1 kHz, while the cavity is driven at an average of 10 photons. The cCPT is a cavity-qubit system that mimics the tunability and noise features of many cQED architectures. Hence the future directions would by default involve the generalization of this technique – to capture and decouple noise in tunable superconducting microwave cavities.

Noise Decoupling in the 2-dimensional Space: The technique we discuss in this thesis work is based on PDH locking, where we extract an error signal that monotonically depends on the magnitude of fluctuations of the tunable bias parameter (i.e., island gate charge). A major caveat of our study is that in order to enable efficient feedback locking, the cCPT must be biased at points where the charge response is significant with the flux effectively decoupled, or vice-versa. An optimized operation of this particular technique, involving a simultaneous compensation for the intrinsic charge and flux noise in tunable microwave cavities, has direct applications in devices where the performance is affected by intrinsically induced resonant frequency fluctuations.

A potential approach towards this objective is the use of double feedback. In particular, the goal would be to route the error signal between two feedback loops, by distinguishing the contribution from each noise source separately. Clearly, this would require a precalibration step, where the extent of noise fluctuations along each source is first extracted by biasing the cCPT with sole contributions from that particular source.

Detection of Coherent Noise Contributions: Apart from the low-frequency noise, another significant noise phenomenon observed is the coupling between the electric dipole moment of a fluctuating near-resonant TLS, and the oscillating electric fields in the device [121, 122]. This coupling manifests itself as an avoided crossing or suppressed T_1 time in tunable qubit systems as the qubit frequency is tuned near the coherent TLS frequency. It may be possible to explore the combined dynamics of such systems using a scheme that utilizes positive feedback to amplify the magnitude of such couplings, both theoretically and experimentally. The key objective here is to get insights into the interesting dynamical processes occurring at a fast time scale on the substrate interface and potentially explore ways to minimize its manifestation during readout. Needless to say, as the noise regime we are interested in is at GHz frequencies, the associated error signal detection would entail an entirely different scheme as opposed to the low-frequency lock-in amplifier setup.

Detection of Poisson Process Switching: As detailed in §4.5, the suppression of the frequency noise in the cCPT was primarily limited by the interference of quasiparticle poisoning in the cCPT. These processes are Poissonian in general, where the switching between the odd and even parity energy states of the cCPT are incoherent. It is important to extract the lifetimes of each state [123] in order to understand the physical origins of these processes.

One potential implementation is to use the concepts discussed in Chapter 4 to detect such random telegraph switching events that cause additional channels of dissipation in cQED systems [98]. In particular, Fig. 6.1a provides an extrapolation of the odd and even energy band structure of the cCPT. The discussions in Chapter 4 exploited the information in the Y quadrature to extract frequency fluctuations about resonance. On the other hand, we observe that the X quadrature is insensitive to these fluctuations at resonance, with peaks corresponding to carrier frequency values at $\omega_0 \pm \omega_{\mathrm{m}}$. As a result, the modulation frequency can be chosen such that $\omega_{\mathrm{m}} = \delta\omega_0^{\mathrm{qp}}$ or $2\omega_{\mathrm{m}} = \delta\omega_0^{\mathrm{qp}}$, where $\delta\omega_0^{\mathrm{qp}} = \omega_0^{(\mathrm{odd})} - \omega_0^{(\mathrm{even})}$ is the difference between the resonant frequencies. Subsequently, the resonance switching events can be detected by the lock-in amplifier with high sensitivity in real time. A proof of concept for this scheme is discussed in Appendix D, where we introduce a deterministic switching event via a gate pulse signal that is detected by the lock-in amplifier accurately.

The reflection measurement using a vector network anaylzer at the bias points where quasiparticle switching events are frequent, outputs incorrect damping rates during the analysis. Quantitatively, the total reflection coefficient is modified as

$$S_{11}^{(\mathrm{VNA})}(\Delta) = P_{(\mathrm{even})} S_{11}(\Delta) + P_{(\mathrm{odd})} S_{11}(\Delta - \delta\omega_0^{\mathrm{qp}}), \tag{6.12}$$

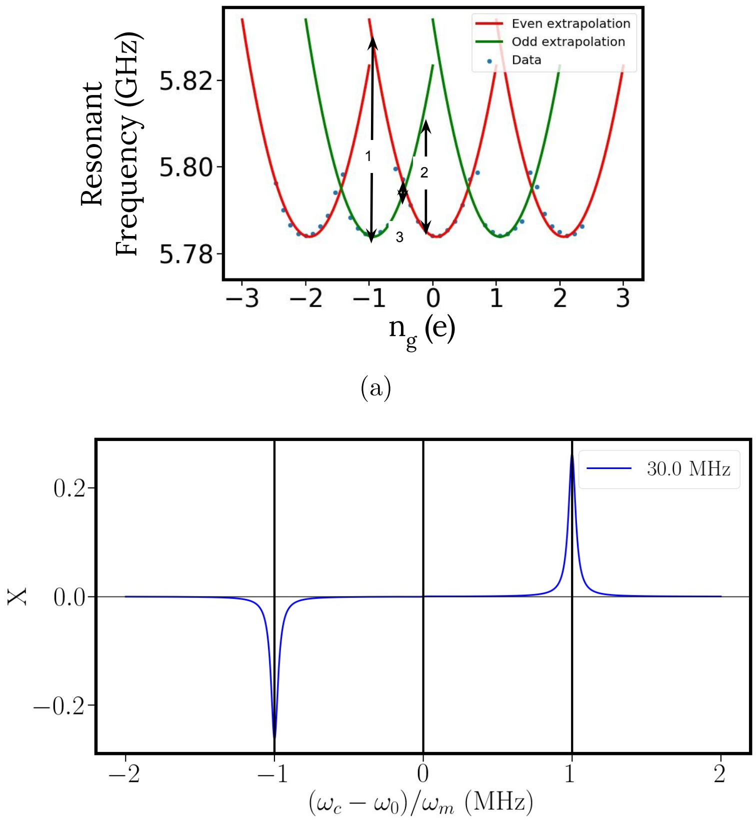

(a)

(b)

Figure 6.1: (a) Extrapolated energy band states of the odd and even parity resonances of the cCPT corresponding to $\Phi_{\text{ext}} = 0$. (b) Response of the X-quadrature as a function of carrier frequency discussed in Fig. 4.1.

where P_i is the probability of the cCPT to being in the state i. Extraction of the proper characteristic time scales of these switching events using the above methodology can be used to calculate P_i. This in turn provides us with the actual damping rates of the cavity using an otherwise incorrect VNA measurement.

Section 6.3

Phase Sensitive Detection using the cCPT

Let us recall the generalized nonlinear cCPT Hamiltonian obtained in §3.2.5 [Eq. (3.43)] with focus on the second-order term: $(a_0 + a_0^\dagger)^k$, where $n = k = 2$. The component we are interested in can be expressed as

$$V_{n,k}\left(a_0+a_0^\dagger\right)^k=\frac{\phi_{zp}^2}{2}\left.\frac{\partial^2 E_{\mathrm{CPT}}^{(0)}}{\partial\phi^2}\right|_{n_g,2\pi\Phi_{\mathrm{ext}}^{(0)}/\Phi_0}\left(a_0^2+a_0^{\dagger 2}+a_0a_0^\dagger+a_0^\dagger a_0\right), \tag{6.13}$$

where we now allow a flux modulation via $\Phi_{\mathrm{ext}}=\Phi_{\mathrm{ext}}^{(0)}+\delta\Phi_{\mathrm{ext}}\cos(\omega_f t+\theta_f)$, with the flux modulation frequency fixed at twice the drive frequency of the cavity near resonance, i.e., $\omega_f\sim 2\omega_p$. In the earlier case of the rotating wave approximation without a flux modulation, the terms a_0^2 and $a_0^{\dagger 2}$ were neglected as these were fast-rotating terms. However, comparing to the CPT Hamiltonian in Eq. (3.30), these terms rotate in the lab frame in the presence of a flux modulation as assumed in the current case. As a result, we may selectively amplify or attenuate either of the quadratures a_0^2 or $a_0^{\dagger 2}$ by fixing the modulation phase accordingly. This mode of detection is phase-sensitive, and can be utilized to extract information about the coupled quantum mechanical system via a single quadrature measurement, as mentioned in Chapter 1.

Chapter 7

Conclusion

Recognizing the importance of gaining better insights into the techniques leading to optimal quantum detection, this thesis covered topics on understanding the fundamental limits determining the measurement imprecision of charge sensing, as well as devising experimental schemes that leads to environmental noise decoupling. In the first phase of this dissertation, the open system dynamics of the cCPT were theoretically explored [13] where we propose that this device can perform quantum-limited, linear charge sensing at very low pump powers. Furthermore, since the cCPT can operate at the single-photon limit, it can be coupled to another quantum system such as a mechanical resonator [34], or a qubit, with minimal back-action. However, experimentally, the sensitivity of the cCPT was observed to be primarily limited by charge noise induced by the two-level system defects in its environment [15]. Hence in the next phase, we successfully demonstrated the suppression of resonant frequency fluctuations induced by this intrinsic charge noise via dynamic feedback control of the system [18]. The relevant results of these two projects are summarized as follows.

In Chapter 3, we presented a first principles, theoretical model of a quantum-limited linear electrometer. The model uses adiabatic elimination of the CPT dynamics, such that the cCPT passively mediates the interactions between the microwave cavity and the measured system (e.g., mechanical resonator) via linear charge sensing. For parameters similar to those of the experimental device described in Ref. [14], we predict the fundamental, quantum noise limited charge sensitivity of the cCPT linear electrometer to be $0.12\,\mu\mathrm{e}/\sqrt{\mathrm{Hz}}$ under a homodyne detection scheme, as discussed in Chapter 5. This sensitivity corresponds to the pumped cavity having an average of one photon, with the cCPT operated in the gate tunable range $0 \leq n_g \leq 0.9$, where the adiabatic approximation is valid and the effects of quasiparticle poisoning may be reduced in an experimental device.

In Chapter 4, we successfully demonstrated the feedback stabilization of a tunable microwave cavity against intrinsic charge noise by locking the cavity to a stable reference. We report stabilization of the cavity resonance over a 3dB bandwidth of 1.4 kHz at $n = 10$. When the cavity is driven at the single photon level, this bandwidth is reduced to 11 Hz, due to the accompanying decrease in SNR. Compensation for intrinsic bias noise stabilizes the resonant frequency with respect to the carrier signal over the course of an actual measurement, as in electrometry and qubit readout. We believe that the resulting enhancement in charge sensitivity can raise the cCPT's performance to operate in the regime of single photon-phonon coupled optomechanics.

Moreover, the feedback scheme reported here can also be extended to tunable microwave cavities in general, provided the dominant source of resonant frequency fluctuations originate from the intrinsic bias noise at the sample. The technique can thus realize real-time detection and correction for bias noise in these devices, potentially improving the coherence and measurement fidelities in superconducting qubits.

In order to demonstrate the feasibility of the concepts discussed in the above mentioned projects, we further complete a charge sensitivity measurement in the few-photon regime, while the cCPT is decoupled from low-frequency noise. As expected, we observe the electrometric capabilities of the cCPT are enhanced in the presence of the feedback, with significant potential for improvement under some circuit remodeling.

In summary, the cCPT forms a mesoscopic system functioning at the classical-quantum regime capable of achieving phase-preserving, near quantum-limited, ultra-sensitive charge detection in the single-photon limit. This device thus have enormous potential to be operated in both linear and non-linear regimes, mediating interactions between quantum systems without the addition of significant backaction.

Appendix A

Linearized Optomechanical Hamiltonian

Let us begin with a cavity described using the photon annihilation operator $\hat{a}$ and a mechanical oscillator defined by the phonon operator $\hat{b}$. The amplitude and phase quadrature operators $\hat{X}$ and $\hat{Y}$ for the cavity can then be defined as

$$\hat{X} = \frac{a + a^\dagger}{\sqrt{2}} \tag{A.1}$$

$$\hat{Y} = \frac{a - a^\dagger}{\sqrt{2}i}. \tag{A.2}$$

Similarly the dimensionless position and momentum operators $\hat{Q}$ and $\hat{P}$ for the mechanical resonator (MR) are

$$\hat{Q} = \frac{b + b^\dagger}{\sqrt{2}} = \frac{1}{\sqrt{2}}\frac{\hat{x}}{x_{zp}} \qquad\qquad \hat{P} = \frac{b - b^\dagger}{\sqrt{2}i}. \tag{A.3}$$

The quantum Langevin equations for the resonator and the cavity can then be deduced from the Heisenberg equation of motion for a closed system given by

$$\dot{\hat{O}} = -\frac{i}{\hbar}[\hat{O}, \mathcal{H}] + \frac{\partial \hat{O}}{\partial t}. \tag{A.4}$$

In short, we will assume that the cavity is weakly coupled to a bath of independent oscillators, where the cavity damping κ remains constant in our frequency region of interest, i.e., taking the Markovian limit. Assuming a coherent input drive at a frequency ω_p near resonance with $\alpha_{\text{in}} = \langle a_{\text{in}} \rangle \neq 0$, and performing a rotating wave approximation on the system-bath Hamiltonian $\mathcal{H} = \mathcal{H}_{\text{sys}} + \mathcal{H}_{\text{bath}}$ where we neglect the counter-rotating terms, the quantum-Langevin equation can be modified into the familiar form [79]

$$\dot{\hat{O}} = -\frac{i}{\hbar}[\hat{O}, \mathcal{H}] - [\hat{O}, a^\dagger]\left(\frac{\kappa}{2}a - \sqrt{\kappa}a_{\text{in}}(t)\right) + \left(\frac{\kappa}{2}a^\dagger - \sqrt{\kappa}\, a_{\text{in}}^\dagger(t)\right)[\hat{O}, a]. \tag{A.5}$$

For the mechanical resonator case, the analogous form can be written as

$$\dot{\hat{O}} = -\frac{i}{\hbar}[\hat{O}, \mathcal{H}] + i\sqrt{2\Gamma}\;[\hat{O}, \hat{Q}]\; P_{\text{in}}(t) + \frac{\Gamma}{2i\Omega}\left\{[\hat{O}, \hat{Q}], \dot{\hat{Q}}\right\}, \tag{A.6}$$

where Ω and Γ denote the resonant frequency and damping of the resontator, respectively, and P_{in} is the dimensionless input momentum fluctuations.

In the limit of high intra-cavity photon number $n = \langle a \rangle^2 \equiv \alpha^2$, we can simplify the dynamics by looking at the small quantum fluctuations around a classical steady state. To that end, we may displace $a \to \alpha + a$ and $b \to \beta + b$, and the coherent optical drive in (A.5) can be absorbed into the system Hamiltonian such that a_{in} in (A.5) can also be written as the quantum fluctuations about α_{in}. The generalized open optomechanical Hamiltonian thus becomes [79]

$$\mathcal{H} = \hbar\Delta a^\dagger a + \hbar\Omega\, b^\dagger b + \hbar G a^\dagger a \hat{x} + \hbar\epsilon(a + a^\dagger), \tag{A.7}$$

where $\epsilon \propto \alpha_{in}$. With an appropriate choice of steady-state optical and mechanical displacement, i.e., α and β, the effects of coherent optical driving and coherent mechanical driving can be cancelled (Refer §2.7 of [79]). As a result, the linearized optomechanical Hamiltonian can be written as

$$\mathcal{H} = \hbar\Delta a^\dagger a + \hbar\Omega\, b^\dagger b + \hbar\mathcal{G}(a + a^\dagger)(b + b^\dagger), \tag{A.8}$$

where the overall detuning $\Delta \to \Delta + 2\mathcal{G}^2/\Omega$ with $\mathcal{G} \equiv x_{zp} G\alpha$. Furthermore, for zero detuning $\Delta = 0$, the equations of motion for the quadrature operators can be obtained using (A.5) and (A.6) as

$$\begin{aligned}
\dot{X} &= -\frac{\kappa}{2}X + \sqrt{\kappa}X_{\text{in}}, && \text{(A.9)}\\
\dot{Y} &= -\frac{\kappa}{2}Y + \sqrt{\kappa}Y_{\text{in}} - 2\mathcal{G}Q, && \text{(A.10)}\\
\dot{Q} &= \Omega P, && \text{(A.11)}\\
\dot{P} &= -\Omega Q - 2\mathcal{G}X + \sqrt{2\Gamma}P_{\text{in}} - \Gamma P. && \text{(A.12)}
\end{aligned}$$

Remark A.1. Note that X and Y equations of motion are independent and the mechanical displacement information is contained in the Y quadrature alone. As discussed in §6.1 and appendix B, this is not the case for cCPT-MR and the equations are more complicated to solve.

In the bad cavity limit $\kappa \gg \Omega$, we can treat X, Y with the assumption that these reach equilibrium much faster than other system variables, i.e., $\dot{X} = \dot{Y} = 0$. As a result,

$$\begin{aligned}
X &= \frac{2X_{\text{in}}}{\sqrt{\kappa}}, && \text{(A.13)}\\
Y &= \frac{2}{\kappa}\left(\sqrt{\kappa}Y_{\text{in}} - 2\mathcal{G}Q\right). && \text{(A.14)}
\end{aligned}$$

Remark A.2. In the proposed cCPT-MR system [34], the dynamics occurs closer to the good cavity limit for the actual device. However, as the charge sensitivity can be best exploited at the bad cavity limit as discussed in Fig. 5.1d, we first focus on this scenario.

Using the input-output relation $a_{\text{out}} = a_{\text{in}} - \sqrt{\kappa}a$ and Eq (A.14), the output phase quadrature fluctuations can be written as

$$Y_{\text{out}} = -Y_{\text{in}} + \sqrt{\frac{8}{\kappa}}\left(\frac{\mathcal{G}}{x_{zp}}\right)x. \tag{A.15}$$

Thus the information about the position of the mechanical resonator can be extracted using a single quadrature measurement of the cavity.

Appendix B

Single-photon Optomechanics

In the single-photon regime with n closer to 1, we retain the general form of Hamiltonian such that

$$\begin{aligned}\mathcal{H} &= \hbar\Delta a^\dagger a + \hbar\Omega\, b^\dagger b + \hbar G a^\dagger a \hat{x} \\ &= \hbar\Delta a^\dagger a + \hbar\Omega\, b^\dagger b + \hbar\mathcal{G} a^\dagger a \hat{Q}, \end{aligned} \tag{B.1}$$

where $\Delta = \omega_c - \omega_p$ and $\mathcal{G} = \sqrt{2}x_{zp}G$, with the definitions following description in Appendix A.

Solution for the photon annihilation operator $a(\omega)$***:*** Let's begin by writing down the relevant equations of motion derived from Eqs. (A.5) and (A.6):

$$\dot{a}(t) = -i\left(\Delta + \mathcal{G}Q(t)\right)a(t) - \frac{\kappa}{2}a(t) + \sqrt{\kappa}\left(a_{\mathrm{in}}(t) + \alpha_{\mathrm{in}}\right) \tag{B.2}$$

where $a_{\mathrm{in}} \to \alpha_{\mathrm{in}} + a_{\mathrm{in}}$ with $\alpha_{\mathrm{in}} = \langle a_{\mathrm{in}}\rangle$ is a constant in the pump rotating frame. For the mechanical resonator,

$$\dot{Q}(t) = \Omega P(t) \tag{B.3}$$

$$\dot{P}(t) = -\Omega Q(t) - \mathcal{G}a^\dagger a + \sqrt{2\Gamma}P_{\mathrm{in}} - \Gamma P \tag{B.4}$$

can be combined into a single second-order equation

$$\ddot{Q}(t) + \Gamma\dot{Q}(t) + \Omega^2 Q(t) = \sqrt{2\Gamma}P_{\mathrm{in}} - \mathcal{G}a^\dagger a. \tag{B.5}$$

As we are interested in the steady-state solution, we obtain in the Fourier domain

$$Q(\omega) = \chi(\omega)\left(\sqrt{2\Gamma}P_{\mathrm{in}}(\omega) - \mathcal{G}a^\dagger a(\omega)\right) \tag{B.6}$$

where $\chi(\omega) = \Omega/(\Omega^2 - \omega^2 - i\omega\Gamma)$. Thus the solution for $Q(\omega)$ is a Lorentzian with peaks at $\pm\Omega$. For further calculation, $Q(\omega)$ is approximated to be delta functions at $\pm\Omega$.

As a result, we can now find the steady-state solution for $a(\omega)$ at $\Delta = 0$ using Eq.(B.6) as

$$\left(-i\omega + \frac{\kappa}{2}\right)a(\omega) = \sqrt{\kappa}\Big(a_{in}(\omega) + \alpha_{in}\delta(\omega)\Big) - i\mathcal{G}\Big(Q(\Omega)a(\omega-\Omega) + Q(-\Omega)a(\omega+\Omega)\Big) \tag{B.7}$$

where we used the Fourier property

$$\mathcal{F}\left(\hat{O}_1(t)\hat{O}_2(t)\right) \;=\; \int_{-\infty}^{\infty}\hat{O}_1(\omega-\omega')\hat{O}_2(\omega')d\omega'. \tag{B.8}$$

Similarly writing down (B.7) for $\omega = \omega \pm \Omega$ and neglecting the corresponding second side band terms $a(\omega \pm 2\Omega)$, we obtain

$$\left(-i(\omega\pm\Omega) + \frac{\kappa}{2}\right)a(\omega\pm\Omega) = \sqrt{\kappa}a_{\mathrm{in}}(\omega\pm\Omega) - i\mathcal{G}\;Q(\pm\Omega)a(\omega). \tag{B.9}$$

Substituting for $a(\omega \pm \Omega)$ in (B.7) using (B.9), we get the solution for $a(\omega)$ close to zero-detuning as

$$\begin{aligned}\left(-i\omega + \frac{\kappa}{2}\right)a(\omega) \;=\;& \sqrt{\kappa}\Big(a_{\mathrm{in}}(\omega) + \alpha_{\mathrm{in}}\delta(\omega)\Big)\\ & -i\sqrt{\kappa}\mathcal{G}\left(\frac{Q(\Omega)a_{\mathrm{in}}(\omega-\Omega)}{-i(\omega-\Omega)+\frac{\kappa}{2}} + \frac{Q(-\Omega)a_{\mathrm{in}}(\omega+\Omega)}{-i(\omega+\Omega)+\frac{\kappa}{2}}\right)\\ & +\mathcal{O}(\mathcal{G})^2.\end{aligned} \tag{B.10}$$

Note that this coincides with the result obtained in Eq. (5.3) that descibes detection of a sinusoidal gate modulation (a simulated environment instead of an actual mechanical resonator) by the cavity component of the cCPT.

Displacement information in quadrature Writing down the equations of motion for $X(t)$ and $Y(t)$ gives

$$\begin{aligned}\dot{X}(t) &= \mathcal{G}Q(t)Y(t) - \frac{\kappa}{2}X(t) + \sqrt{\kappa}\left(X_{\text{in}}(t) + \sqrt{2}\alpha_{\text{in}}\right) &\text{(B.11)}\\ \dot{Y}(t) &= -\mathcal{G}Q(t)X(t) - \frac{\kappa}{2}Y(t) + \sqrt{\kappa}Y_{\text{in}}(t) &\text{(B.12)}\end{aligned}$$

Note that the two equations are coupled, and both the quadrature information is required to measure the displacement of mechanical resonator.

Furthermore, let's also look at the equation of motion for $a^\dagger(t)a(t)$ given by

$$\frac{d}{dt}\left(a^\dagger(t)a(t)\right) = -\kappa a^\dagger(t)a(t) + \sqrt{\kappa}\left(X_{\text{in}}(t)X(t) + Y_{\text{in}}(t)Y(t)\right). \tag{B.13}$$

As can be deduced from the above expression, there is no Q information stored in the number quadrature of the cavity $a^\dagger a(t)$, implying the need to investigate its conjugate observable $\hat{\theta}$.

Appendix C

The Phase Operator

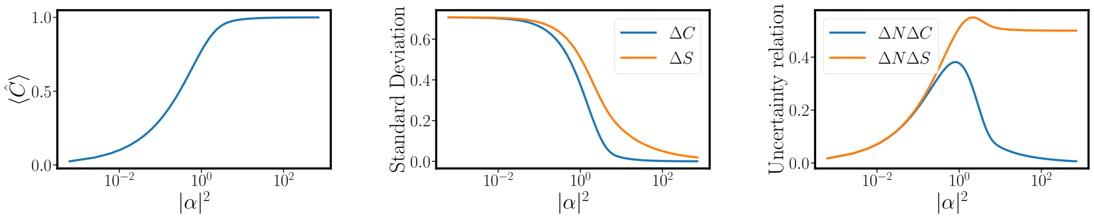

Figure C.1: (a) Expectation of cos operator with $\langle C\rangle \to 1$ for $N \gg 1$. (b) Standard deviation of phase operators both die down for $N \gg 1$. (c) Corresponding uncertainty relations with $\Delta N \Delta S = \Delta N \Delta\theta = 1/2$ for $N \gg 1$.

As mentioned in §6.1, it is important to look at the range of fluctuations of the phase shift. This can be verified by looking into $\langle\hat{C}\rangle$ and $\langle\hat{S}\rangle$, and the variance around the expectations ΔC and ΔS. We will assume an input coherent state such that $a_{\text{in}}|\alpha\rangle = (\alpha + \delta a_{\text{in}})|\alpha\rangle$ and the cavity annihilation operator $a \approx 2a_{\text{in}}/\sqrt{\kappa} + \mathcal{O}(\mathcal{G})$ at resonance using (B.10). Hence we will assume that the cavity state is a coherent state as well, with a photon number closer to 1. We will also take $\langle \delta a_{\text{in}}^{\dagger} \delta a_{\text{in}}\rangle \ll |\alpha|^2$ since $k_B T/\hbar\omega$ ratio gives very low photon occupancy. Thus for a coherent state

$$|\alpha\rangle = e^{-|\alpha|^2/2} \sum_{n=0}^{\infty} \frac{\alpha^n}{\sqrt{n!}} |n\rangle. \tag{C.1}$$

For real α, we have $\langle\hat{C}\rangle = \langle\hat{E}\rangle$ and $\langle\hat{S}\rangle = 0$. Hence we can make the assumption

$\hat{S} \approx \hat{\theta}$ if ΔS is small.

$$\langle \hat{C} \rangle = \langle \hat{E} \rangle = \langle \hat{E}^{\dagger} \rangle = e^{-|\alpha|^2} \sum_{n=0}^{\infty} \frac{|\alpha|^{2n}\alpha}{n!\sqrt{n+1}}. \tag{C.2}$$

Clearly for $|\alpha| < 1$, $\langle \hat{E} \rangle = \mathcal{O}(\alpha)$ and $\langle \hat{E} \rangle^2 = \mathcal{O}(\alpha^2)$. Similarly,

$$\langle \hat{E}^2 \rangle = \langle \hat{E^{\dagger}}^2 \rangle = e^{-|\alpha|^2} \sum_{n=0}^{\infty} \frac{|\alpha|^{2n}\alpha^2}{n!\sqrt{(n+1)(n+2)}}. \tag{C.3}$$

The variance ΔC^2 is given by $\langle \hat{C}^2 \rangle - \langle \hat{C} \rangle^2$ where

$$\langle \hat{C}^2 \rangle = \frac{1}{2}\left(1 + \langle E^2 \rangle\right). \tag{C.4}$$

Similarly,

$$\Delta S^2 = \frac{1}{2}\left(1 - \langle E^2 \rangle\right). \tag{C.5}$$

As seen in Fig C.1, the variations in sin operator $\hat{S}$ dies down in the high photon limit making it possible to make the approximation $\hat{S} \approx \hat{\theta}$. Since $\Delta N = \sqrt{N}$, the uncertainty relation $\Delta N \Delta \theta = 1/2$ for $N \gg 1$ as expected.

Note that for $N = 1$, $\Delta S = 0.51$ and $\sin\theta \approx \theta$ may hold ($\sin^{-1} 0.51 = 0.54$). Hence we may assume the fluctuations about $\hat{S}$ to be small in the lower photon limit as long as $N > 1$, enabling us to proceed our calculations using $\hat{S} \approx \hat{\theta}$. But as seen in Fig C.1(c), the uncertainty relation $\Delta N \Delta \theta$ peaks above 1/2 before saturating.

Appendix D

Detection of Two-mode Switching

Following figures provide a proof of concept for the the real-time detection of Poisson processes using a phase-modulated tone. These measurements are completed by pulse-modulating the gate of the cCPT at 50 Hz. As result, the X quadrature of the derivative of the reflected intensity captures the switching events with high sensitivity, when the modulation frequency is half the difference of the resonant frequencies of the two states.

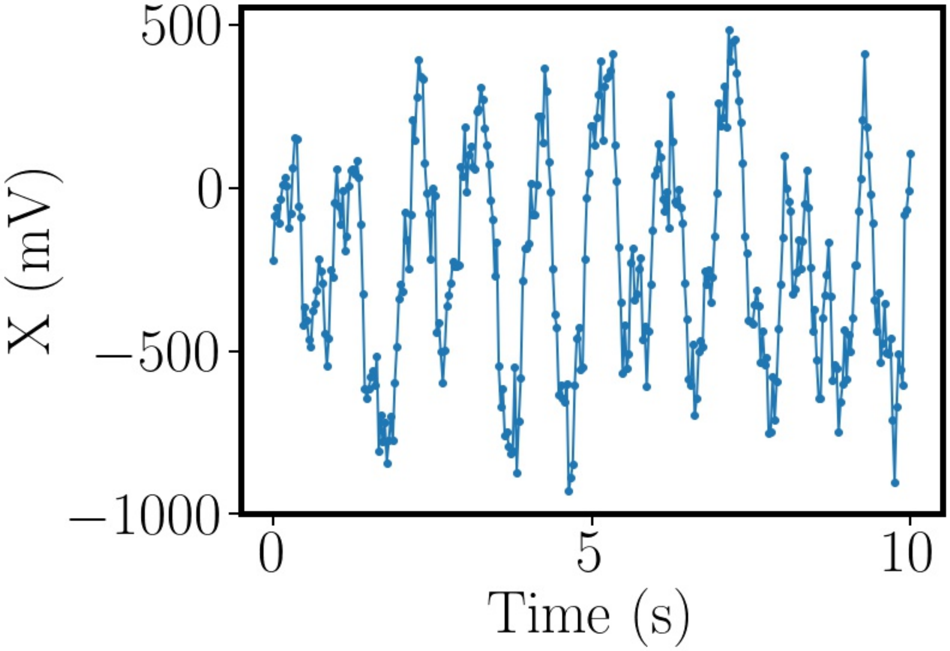

Figure D.1: Detection of the switching between two n_g states. Following the scheme discussed in §6.2, the lock-in amplifier detects the switching events occurring at 50 Hz frequency and a duty cycle of 50%, as is illustrated in this time-domain measurement.

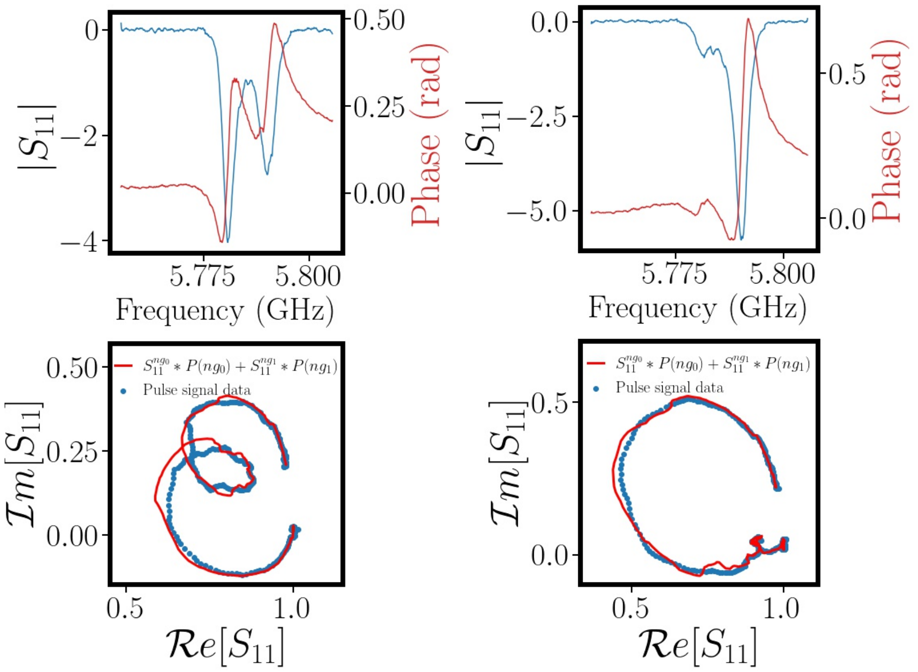

Figure D.2: Reflection measurement using VNA with the cCPT gate modulated using a pulse signal with different duty cycles D. The pulse frequency of the gate input and the IF bandwidth of the VNA are set to 50 and 10 Hz, respectively, such that the switching between two bias points is captured. Duty cycles for the plots on the left is 50% and on the right is 90%. The bottom plots capture the response in the complex plane with corresponding fits following Eq.(6.12), where $P_1 = D/100$ and $P_2 = 1 - D/100$.

Bibliography

[1] A. A. Clerk, M. H. Devoret, S. M. Girvin, Florian Marquardt, and R. J. Schoelkopf. Introduction to quantum noise, measurement, and amplification. *Rev. Mod. Phys.*, 82(2):1155–1208, April 2010.

[2] Francesco Massel, Tero T Heikkilä, J-M Pirkkalainen, Sung-Un Cho, Heini Saloniemi, Pertti J Hakonen, and Mika A Sillanpää. Microwave amplification with nanomechanical resonators. *Nature*, 480(7377):351–354, 2011.

[3] Christopher Eichler, Deniz Bozyigit, and Andreas Wallraff. Characterizing quantum microwave radiation and its entanglement with superconducting qubits using linear detectors. *Physical Review A*, 86(3):032106, 2012.

[4] Carlton M Caves. Quantum limits on noise in linear amplifiers. *Physical Review D*, 26(8):1817, 1982.

[5] Jeremy B Clark, Florent Lecocq, Raymond W Simmonds, José Aumentado, and John D Teufel. Observation of strong radiation pressure forces from squeezed light on a mechanical oscillator. *Nature Physics*, 12(7):683–687, 2016.

[6] Junho Suh, AJ Weinstein, CU Lei, EE Wollman, SK Steinke, Pierre Meystre, Aashish A Clerk, and KC Schwab. Mechanically detecting and avoiding the quantum fluctuations of a microwave field. *Science*, 344(6189):1262–1265, 2014.

[7] Alexandre M Souza, Gonzalo A Álvarez, and Dieter Suter. Robust dynamical decoupling. *Philosophical Transactions of the Royal Society A: Mathematical, Physical and Engineering Sciences*, 370(1976):4748–4769, 2012.

[8] M Mück, C Heiden, and J Clarke. Investigation and reduction of excess low-frequency noise in rf superconducting quantum interference devices. *Journal of Applied Physics*, 75(9):4588–4592, 1994.

[9] Alexander N Korotkov. Quantum bayesian approach to circuit qed measurement with moderate bandwidth. *Physical Review A*, 94(4):042326, 2016.

[10] Aashish A Clerk and Steven Bennett. Quantum nanoelectromechanics with electrons, quasi-particles and cooper pairs: effective bath descriptions and strong feedback effects. *New Journal of Physics*, 7(1):238, 2005.

[11] MP Blencowe, Jara Imbers, and AD Armour. Dynamics of a nanomechanical resonator coupled to a superconducting single-electron transistor. *New Journal of Physics*, 7(1):236, 2005.

[12] AA Clerk, SM Girvin, AK Nguyen, and AD Stone. Resonant cooper-pair tunneling: quantum noise and measurement characteristics. *Physical review letters*, 89(17):176804, 2002.

[13] S Kanhirathingal, B. L. Brock, A. J. Rimberg, and M. P. Blencowe. Charge sensitivity of a cavity-embedded Cooper pair transistor limited by single-photon shot noise. *Journal of Applied Physics*, 130(11):114401, 2021.

[14] B. L. Brock, Juliang Li, S. Kanhirathingal, B. Thyagarajan, W. F. Braasch, M. P. Blencowe, and A. J. Rimberg. Nonlinear charge- and flux- tunable cavity derived from an embedded cooper-pair transistor. *Phys. Rev. Appl.*, 15:044009, 2021.

[15] B. L. Brock, Juliang Li, S. Kanhirathingal, B. Thyagarajan, M. P. Blencowe, and A. J. Rimberg. Fast and ultrasensitive electrometer operating at the single-photon level. *Physical Review Applied*, 16:L051004, Nov 2021.

[16] Vladimir B Braginsky, Vladimir Borisovich Braginski, and Farid Ya Khalili. *Quantum measurement*. Cambridge University Press, 1995.

[17] Gerd Breitenbach, S Schiller, and J Mlynek. Measurement of the quantum states of squeezed light. *Nature*, 387(6632):471–475, 1997.

[18] S Kanhirathingal, B Thyagarajan, BL Brock, Juliang Li, E Jeffrey, MP Blencowe, JY Mutus, and AJ Rimberg. Feedback stabilization of the resonant frequency in tunable microwave cavities with single-photon occupancy. *arXiv preprint arXiv:2202.04227*, 2022.

[19] K. W. Lehnert, K. Bladh, L. F. Spietz, D. Gunnarsson, D. I. Schuster, P. Delsing, and R. J. Schoelkopf. Measurement of the excited-state lifetime of a microelectronic circuit. 90:027002, 2003.

[20] J. J. Pla, K. Y. Tan, J. P. Dehollain, W. H. Lim, J. J. L. Morton, D. N. Jamieson, A. S. Dzurak, and A. Morello. A single-atom electron spin qubit in silicon. *Nature*, 489:541–545, 2012.

[21] O. Naaman and J. Aumentado. Time-domain measurements of quasiparticle tunneling rates in a single-Cooper-pair transistor. 73:172504, 2006.

[22] M. D. LaHaye, O. Buu, B. Camarota, and K. C. Schwab. Approaching the quantum limit of a nanomechanical resonator. *Science*, 304:74–77, 2004.

[23] R. J. Schoelkopf, P. Wahlgren, A. A. Kozhevnikov, P. Delsing, and D. E. Prober. The radio-frequency single-electron transistor (RF-SET): A fast and ultrasensitive electrometer. *Science*, 280:1238–1242, 1998.

[24] Rupert M Lewis, Charles Thomas Harris, and Eric A Shaner. A single electron transistor charge sensor in strong rf fields. *AIP Advances*, 8(10):105317, 2018.

[25] Michel H. Devoret and Robert J. Schoelkopf. Amplifying quantum signals with the single-electron transistor. *Nature*, 406(6799):1039–1046, aug 2000.

[26] A. N. Korotkov. Nonideal quantum detectors in Bayesian formalism. *Phys. Rev. B*, 67:235408, 2003.

[27] A. A. Clerk. Quantum-limited position detection and amplification: A linear response perspective. *Phys. Rev. B*, 70:245306, 2004.

[28] M. A. Sillanpää, T. Lehtinen, A. Paila, Yu. Makhlin, L. Roschier, and P. J. Hakonen. Direct Observation of Josephson Capacitance. *Phys. Rev. Lett.*, 95(20):206806, November 2005.

[29] F. Persson, C. M. Wilson, M. Sandberg, and P. Delsing. Fast readout of a single Cooper-pair box using its quantum capacitance. *Phys. Rev. B*, 82:134533, 2010.

[30] L. Tosi, D. Vion, and H. Le Sueur. Design of a Cooper-pair box electrometer for application to solid-state and astroparticle physics. *Phys. Rev. Appl.*, 11(5):054072, May 2019.

[31] Mika A Sillanpää, Leif Roschier, and Pertti J Hakonen. Inductive single-electron transistor. *Phys. Rev. Lett.*, 93(6):066805, 2004.

[32] A. B. Zorin. Radio-frequency Bloch-transistor electrometer. *Phys. Rev. Lett.*, 86:3388–3391, 2001.

[33] Mika A. Sillanpää, Leif Roschier, and Pertti J. Hakonen. Charge sensitivity of the inductive single-electron transistor. *Appl. Phys. Lett.*, 87(9):092502, August 2005.

[34] A. J. Rimberg, M. P. Blencowe, A. D. Armour, and P. D. Nation. A cavity-Cooper pair transistor scheme for investigating quantum optomechanics in the ultra-strong coupling regime. *New J. Phys.*, 16(5):055008, May 2014.

[35] Clemens Müller, Jared H. Cole, and Jürgen Lisenfeld. Towards understanding two-level-systems in amorphous solids: insights from quantum circuits. *Rep. Prog. Phys.*, 82(12):124501, October 2019.

[36] Lara Faoro and Lev B Ioffe. Interacting tunneling model for two-level systems in amorphous materials and its predictions for their dephasing and noise in superconducting microresonators. *Physical Review B*, 91(1):014201, 2015.

[37] P W Anderson, Bertrand I Halperin, and C M Varma. Anomalous low-temperature thermal properties of glasses and spin glasses. *Philosophical Magazine*, 25(1):1–9, 1972.

[38] Steffen Schlör, Jürgen Lisenfeld, Clemens Müller, Alexander Bilmes, Andre Schneider, David P Pappas, Alexey V Ustinov, and Martin Weides. Correlating decoherence in transmon qubits: Low frequency noise by single fluctuators. *Physical Review Letters*, 123(19):190502, 2019.

[39] E. Paladino, Y. M. Galperin, G. Falci, and B. L. Altshuler. $1/f$ noise: Implications for solid-state quantum information. *Rev. Mod. Phys.*, 86(2):361–418, April 2014.

[40] Jonathan J Burnett, Andreas Bengtsson, Marco Scigliuzzo, David Niepce, Marina Kudra, Per Delsing, and Jonas Bylander. Decoherence benchmarking of superconducting qubits. *npj Quantum Information*, 5(1):1–8, 2019.

[41] S. M. Anton, Clemens Müller, J. S. Birenbaum, S. R. O'Kelley, A. D. Fefferman, Dmitri S Golubev, G. C. Hilton, H-M Cho, K. D Irwin, Frederick C Wellstood, et al. Pure dephasing in flux qubits due to flux noise with spectral density scaling as $1/f^\alpha$. *Physical Review B*, 85(22):224505, 2012.

[42] Yong Lu, Andreas Bengtsson, Jonathan J Burnett, Baladitya Suri, Sankar Raman Sathyamoorthy, Hampus Renberg Nilsson, Marco Scigliuzzo, Jonas Bylander, Göran Johansson, and Per Delsing. Quantum efficiency, purity and stability of a tunable, narrowband microwave single-photon source. *npj Quantum Information*, 7(1):1–8, 2021.

[43] A. B. Zorin, F-J Ahlers, J Niemeyer, Th Weimann, H Wolf, V. A. Krupenin, and S. V. Lotkhov. Background charge noise in metallic single-electron tunneling devices. *Physical Review B*, 53(20):13682, 1996.

[44] Martin V Gustafsson, Arsalan Pourkabirian, Göran Johansson, John Clarke, and Per Delsing. Thermal properties of charge noise sources. *Physical Review B*, 88(24):245410, 2013.

[45] G Zimmerli, Travis M Eiles, Richard L Kautz, and John M Martinis. Noise in the coulomb blockade electrometer. *Applied Physics Letters*, 61(2):237–239, 1992.

[46] Frederick C Wellstood, Cristian Urbina, and John Clarke. Low-frequency noise in dc superconducting quantum interference devices below 1 K. *Applied Physics Letters*, 50(12):772–774, 1987.

[47] M Hatridge, R Vijay, D. H. Slichter, John Clarke, and I Siddiqi. Dispersive magnetometry with a quantum limited SQUID parametric amplifier. *Physical Review B*, 83(13):134501, 2011.

[48] E. M. Levenson-Falk, R Vijay, N Antler, and I Siddiqi. A dispersive nanosquid magnetometer for ultra-low noise, high bandwidth flux detection. *Superconductor Science and Technology*, 26(5):055015, 2013.

[49] D Cattiaux, I Golokolenov, S Kumar, M Sillanpää, L Mercier de Lépinay, R. R. Gazizulin, X Zhou, A. D. Armour, O Bourgeois, A Fefferman, and E Collin. A macroscopic object passively cooled into its quantum ground state of motion beyond single-mode cooling. *Nature Communications*, 12(1):1–6, 2021.

[50] AD Fefferman, RO Pohl, AT Zehnder, and JM Parpia. Acoustic properties of amorphous silica between 1 and 500 mK. *Physical Review Letters*, 100(19):195501, 2008.

[51] CM Quintana, Yu Chen, Daniel Sank, AG Petukhov, TC White, Dvir Kafri, Ben Chiaro, Anthony Megrant, Rami Barends, Brooks Campbell, et al. Observation of classical-quantum crossover of 1/f flux noise and its paramagnetic temperature dependence. *Physical review letters*, 118(5):057702, 2017.

[52] S. E. de Graaf, L. Faoro, J. Burnett, A. A. Adamyan, A. Ya Tzalenchuk, S. E. Kubatkin, T. Lindström, and A. V. Danilov. Suppression of low-frequency charge noise in superconducting resonators by surface spin desorption. *Nat. Commun*, 9(1):1143, March 2018.

[53] Long B Nguyen, Yen-Hsiang Lin, Aaron Somoroff, Raymond Mencia, Nicholas Grabon, and Vladimir E Manucharyan. High-coherence fluxonium qubit. *Physical Review X*, 9(4):041041, 2019.

[54] P Kumar, S Sendelbach, M. A Beck, J. W. Freeland, Zhe Wang, Hui Wang, C Yu Clare, R. Q. Wu, D. P. Pappas, and R McDermott. Origin and reduction of $1/f$ magnetic flux noise in superconducting devices. *Physical Review Applied*, 6(4):041001, 2016.

[55] Carolyn T Earnest, Jérémy H Béjanin, Thomas G McConkey, Evan A Peters, Andreas Korinek, Hui Yuan, and Matteo Mariantoni. Substrate surface engineering for high-quality silicon/aluminum superconducting resonators. *Superconductor Science and Technology*, 31(12):125013, 2018.

[56] Corey Rae Harrington McRae, Haozhi Wang, Jiansong Gao, Michael R Vissers, Teresa Brecht, Andrew Dunsworth, David P Pappas, and Josh Mutus. Materials loss measurements using superconducting microwave resonators. *Review of Scientific Instruments*, 91(9):091101, 2020.

[57] Jens Koch, M Yu Terri, Jay Gambetta, Andrew A Houck, David I Schuster, Johannes Majer, Alexandre Blais, Michel H Devoret, Steven M Girvin, and Robert J Schoelkopf. Charge-insensitive qubit design derived from the Cooper pair box. *Physical Review A*, 76(4):042319, 2007.

[58] Takashi Nakajima, Yohei Kojima, Yoshihiro Uehara, Akito Noiri, Kenta Takeda, Takashi Kobayashi, and Seigo Tarucha. Real-time feedback control of charge sensing for quantum dot qubits. *Physical Review Applied*, 15(3):L031003, 2021.

[59] Lin Tian. Correcting low-frequency noise with continuous measurement. *Physical Review Letters*, 98(15):153602, 2007.

[60] J Kelly. *Fault-tolerant superconducting qubits.* PhD thesis, 2015.

[61] Tero T Heikkilä, Francesco Massel, Jani Tuorila, Raphaël Khan, and Mika A Sillanpää. Enhancing optomechanical coupling via the Josephson effect. *Physical Review Letters*, 112(20):203603, 2014.

[62] A. Nunnenkamp, K. Børkje, and S. M. Girvin. Single-photon optomechanics. *Physical Review Letters*, 107(6):063602, August 2011.

[63] J-M Pirkkalainen, SU Cho, Francesco Massel, J Tuorila, TT Heikkilä, PJ Hakonen, and MA Sillanpää. Cavity optomechanics mediated by a quantum two-level system. *Nature communications*, 6(1):1–6, 2015.

[64] Catherine Laflamme and Aashish A Clerk. Quantum-limited amplification with a nonlinear cavity detector. *Phys. Rev. A*, 83(3):033803, 2011.

[65] B. L. Brock. *Ultrasensitive electrometry at the single-photon level.* PhD thesis, Dartmouth College, 2021.

[66] Eric D Black. An introduction to Pound–Drever–Hall laser frequency stabilization. *American Journal of Physics*, 69(1):79–87, 2001.

[67] Tobias Lindström, Jonathan Burnett, Mark Oxborrow, and A Ya. Tzalenchuk. Pound-locking for characterization of superconducting microresonators. *Review of Scientific Instruments*, 82(10):104706, 2011.

[68] David Niepce, Jonathan J Burnett, Marina Kudra, Jared H Cole, and Jonas Bylander. Stability of superconducting resonators: Motional narrowing and the role of Landau-Zener driving of two-level defects. *Science advances*, 7(39):eabh0462, 2021.

[69] Jonathan Burnett, Lara Faoro, I Wisby, V. L. Gurtovoi, A. V. Chernykh, G. M. Mikhailov, V. A. Tulin, R Shaikhaidarov, V Antonov, PJ Meeson, et al. Evidence for interacting two-level systems from the 1/f noise of a superconducting resonator. *Nature Communications*, 5(1):1–6, 2014.

[70] Rami Barends, James Wenner, Michael Lenander, Yu Chen, Radoslaw C Bialczak, Julian Kelly, Erik Lucero, Peter O'Malley, Matteo Mariantoni, Daniel Sank, et al. Minimizing quasiparticle generation from stray infrared light in superconducting quantum circuits. *Applied Physics Letters*, 99(11):113507, 2011.

[71] V Zaretskey, B Suri, S Novikov, FC Wellstood, and BS Palmer. Spectroscopy of a cooper-pair box coupled to a two-level system via charge and critical current. *Physical Review B*, 87(17):174522, 2013.

[72] David M. Pozar. *Microwave Engineering.* Wiley, 4th ed edition, 2012.

[73] Crispin Gardiner, Peter Zoller, and Peter Zoller. *Quantum noise: a handbook of Markovian and non-Markovian quantum stochastic methods with applications to quantum optics.* Springer Science & Business Media, 2004.

[74] Hermann Grabert and Michel H Devoret. *Single charge tunneling: Coulomb blockade phenomena in nanostructures*, volume 294. Springer Science & Business Media, 2013.

[75] P Joyez. *The single Cooper pair transistor: a macroscopic quantum system.* PhD thesis, 1995.

[76] Alexandre Blais, Arne L Grimsmo, SM Girvin, and Andreas Wallraff. Circuit quantum electrodynamics. *Reviews of Modern Physics*, 93(2):025005, 2021.

[77] David Isaac Schuster. *Circuit quantum electrodynamics.* Yale University, 2007.

[78] Daniel F Walls and Gerard J Milburn. *Quantum optics.* Springer Science & Business Media, 2007.

[79] Warwick P Bowen and Gerard J Milburn. *Quantum optomechanics.* CRC press, 2015.

[80] John Bechhoefer. Feedback for physicists: A tutorial essay on control. *Reviews of modern physics*, 77(3):783, 2005.

[81] Gene F Franklin, J David Powell, Abbas Emami-Naeini, and J David Powell. *Feedback control of dynamic systems*, volume 4. Prentice hall Upper Saddle River, 2002.

[82] Juliang Li. *Near Quantum Limited Charge Detector and Beyond*. PhD thesis, Dartmouth College, 2018.

[83] B Thyagarajan. *The cavity-embedded Cooper pair transistor as a charge detector operating in the nonlinear regime"*. PhD thesis, Dartmouth College, 2022.

[84] Benjamin A. Mazin. *Microwave Kinetic Inductance Detectors*. PhD thesis, California Institute of Technology, 2005.

[85] A. Megrant, C. Neill, R. Barends, B. Chiaro, Yu Chen, L. Feigl, J. Kelly, Erik Lucero, Matteo Mariantoni, P. J. J. O'Malley, D. Sank, A. Vainsencher, J. Wenner, T. C. White, Y. Yin, J. Zhao, C. J. Palmstrøm, John M. Martinis, and A. N. Cleland. Planar superconducting resonators with internal quality factors above one million. *Appl. Phys. Lett.*, 100(11):113510, March 2012.

[86] Anja Metelmann and Aashish A Clerk. Nonreciprocal photon transmission and amplification via reservoir engineering. *Physical Review X*, 5(2):021025, 2015.

[87] Yu Chen, D Sank, P O'Malley, T White, R Barends, B Chiaro, J Kelly, E Lucero, M Mariantoni, A Megrant, et al. Multiplexed dispersive readout of superconducting phase qubits. *Applied Physics Letters*, 101(18):182601, 2012.

[88] Uri Vool and Michel Devoret. Introduction to quantum electromagnetic circuits. *Int. J. Circuit Theory Appl.*, 45(7):897–934, 2017.

[89] Ananda Roy and Michel Devoret. Introduction to parametric amplification of quantum signals with Josephson circuits. *Comptes Rendus Physique*, 17(7):740–755, August 2016.

[90] C. W. Gardiner and M. J. Collett. Input and output in damped quantum systems: Quantum stochastic differential equations and the master equation. *Physical Review A*, 31(6):3761–3774, June 1985.

[91] Bernard Yurke and John S. Denker. Quantum network theory. *Phys. Rev. A*, 29(3):1419–1437, March 1984.

[92] H Wang, M Hofheinz, J Wenner, M Ansmann, RC Bialczak, M Lenander, Erik Lucero, M Neeley, AD O'Connell, D Sank, et al. Improving the coherence time of superconducting coplanar resonators. *Appl. Phys. Lett.*, 95(23):233508, 2009.

[93] R Barends, N Vercruyssen, A Endo, PJ De Visser, T Zijlstra, TM Klapwijk, P Diener, SJC Yates, and JJA Baselmans. Minimal resonator loss for circuit quantum electrodynamics. *Appl. Phys. Lett.*, 97(2):023508, 2010.

[94] SM Barnett and PL Knight. Thermofield analysis of squeezing and statistical mixtures in quantum optics. *JOSA B*, 2(3):467–479, 1985.

[95] John M Martinis and M Nahum. Effect of environmental noise on the accuracy of coulomb-blockade devices. *Phys. Rev. B*, 48(24):18316, 1993.

[96] Brian David Josephson. Possible new effects in superconductive tunnelling. *Physics letters*, 1(7):251–253, 1962.

[97] Michael Tinkham. *Introduction to superconductivity.* Courier Corporation, 2004.

[98] J. Aumentado, Mark W. Keller, John M. Martinis, and M. H. Devoret. Nonequilibrium quasiparticles and $2e$ periodicity in single-Cooper-pair transistors. *Phys. Rev. Lett.*, 92(6):066802, February 2004.

[99] R. M. Lutchyn. Effect of quantum fluctuations on even-odd energy difference in a Cooper-pair box. *Phys. Rev. B*, 75(21):212501, June 2007.

[100] C Neill, A Megrant, R Barends, Yu Chen, B Chiaro, J Kelly, J. Y. Mutus, P. J. J. O'Malley, D Sank, J Wenner, et al. Fluctuations from edge defects in superconducting resonators. *Applied Physics Letters*, 103(7):072601, 2013.

[101] B. L. Brock, M. P. Blencowe, and A. J. Rimberg. Frequency fluctuations in tunable and nonlinear microwave cavities. *Physical Review Applied*, 14(5):054026, 2020.

[102] Yuan-Chi Yang, S. N. Coppersmith, and Mark Friesen. Achieving high-fidelity single-qubit gates in a strongly driven charge qubit with $1/f$ charge noise. *npj Quantum Inf.*, 5(1):1–6, January 2019.

[103] Jonathan Burnett. *High Precision Readout of Superconducting Resonators.* PhD thesis, PhD thesis, 2013.

[104] Hui Wang, M. P. Blencowe, A. D. Armour, and A. J. Rimberg. Quantum dynamics of a Josephson junction driven cavity mode system in the presence of voltage bias noise. *Physical Review B*, 96(10):104503, 2017.

[105] András Gyenis, Pranav S Mundada, Agustin Di Paolo, Thomas M Hazard, Xinyuan You, David I Schuster, Jens Koch, Alexandre Blais, and Andrew A Houck. Experimental realization of a protected superconducting circuit derived from the 0–π qubit. *PRX Quantum*, 2(1):010339, 2021.

[106] Jonas Bylander, Simon Gustavsson, Fei Yan, Fumiki Yoshihara, Khalil Harrabi, George Fitch, David G Cory, Yasunobu Nakamura, Jaw-Shen Tsai, and William D Oliver. Noise spectroscopy through dynamical decoupling with a superconducting flux qubit. *Nature Physics*, 7(7):565–570, 2011.

[107] Chris Macklin, K O'brien, D Hover, M. E. Schwartz, V Bolkhovsky, X Zhang, W. D. Oliver, and I Siddiqi. A near–quantum-limited Josephson traveling-wave parametric amplifier. *Science*, 350(6258):307–310, 2015.

[108] Jose A Aumentado. *Handbook of nanophysics: The Cooper Pair Transistor.* 2010.

[109] Leif Roschier, P. Hakonen, K. Bladh, P. Delsing, K. W. Lehnert, Lafe Spietz, and R. J. Schoelkopf. Noise performance of the radio-frequency single-electron transistor. *J. Appl. Phys.*, 95(3):1274–1286, January 2004.

[110] A. B. Zorin. Quantum-limited electrometer based on single Cooper pair tunneling. *Phys. Rev. Lett.*, 76(23):4408–4411, June 1996.

[111] Henrik Brenning, Sergey Kafanov, Tim Duty, Sergey Kubatkin, and Per Delsing. An ultrasensitive radio-frequency single-electron transistor working up to 4.2 K. *J. Appl. Phys.*, 100(11):114321, December 2006.

[112] W. W. Xue, Z. Ji, Feng Pan, Joel Stettenheim, M. P. Blencowe, and A. J. Rimberg. Measurement of quantum noise in a single-electron transistor near the quantum limit. *Nat. Phys.*, 5(9):660–664, September 2009.

[113] Grigorij J Grabovskij, Torben Peichl, Jürgen Lisenfeld, Georg Weiss, and Alexey V Ustinov. Strain tuning of individual atomic tunneling systems detected by a superconducting qubit. *Science*, 338(6104):232–234, 2012.

[114] O Astafiev, Yu A Pashkin, Y Nakamura, T Yamamoto, and Jaw Shen Tsai. Temperature square dependence of the low frequency $1/f$ charge noise in the Josephson junction qubits. *Phys. Rev. Lett.*, 96(13):137001, 2006.

[115] Christopher Gerry and Peter Knight. *Introductory Quantum Optics.* Cambridge University Press, 2004.

[116] P. Carruthers and Michael Martin Nieto. Phase and angle variables in quantum mechanics. *Rev. Mod. Phys.*, 40(2):411–440, April 1968.

[117] Jeffrey H. Shapiro and Scott R. Shepard. Quantum phase measurement: A system-theory perspective. *Phys. Rev. A*, 43(7):3795–3818, April 1991.

[118] H. Gerhardt, H. Welling, and D. Frölich. Ideal laser amplifier as a phase measuring system of a microscopic radiation field. *Appl. Phys. A*, 2(2):91–93, August 1973.

[119] Bo-Sture K Skagerstam and Bjørn Å Bergsjordet. On the quantum phase operator for coherent states. *Phys. Scr*, 70(1):26, 2004.

[120] S. M. Barnett and D. T. Pegg. On the Hermitian optical phase operator. *J. Mod. Opt*, 36(1):7–19, January 1989.

[121] J. Lisenfeld, A. Bilmes, A. Megrant, R. Barends, J. Kelly, P. Klimov, G. Weiss, J. M Martinis, and A. V. Ustinov. Electric field spectroscopy of material defects in transmon qubits. *npj Quantum Information*, 5(1):1–6, 2019.

[122] Alexander Shnirman, Gerd Schön, Ivar Martin, and Yuriy Makhlin. Low-and high-frequency noise from coherent two-level systems. *Physical review letters*, 94(12):127002, 2005.

[123] Ofer Naaman and Joe Aumentado. Poisson transition rates from time-domain measurements with a finite bandwidth. *Physical review letters*, 96(10):100201, 2006.